

**Measurement of the proton structure function F_2
at
low Bjorken x at the H1 experiment**

Inaugural Dissertation

zur Erlangung der philosophischen Doktorwürde

vorgelegt der

Philosophischen Fakultät II

der

Universität Zürich

von

Katharina Müller

aus Zürich

begutachtet von Prof. Dr. P. Truöl

und Dr. U. Straumann

Zürich 1994

**Measurement of the proton structure function F_2
at
low Bjorken x at the H1 experiment**

Inaugural Dissertation
zur Erlangung der philosophischen Doktorwürde
vorgelegt der
Philosophischen Fakultät II
der
Universität Zürich

von
Katharina Müller
aus Zürich

begutachtet von Prof. Dr. P. Truöl
und Dr. U. Straumann

Zürich 1994

Contents

1	Introduction	3
2	Deep inelastic scattering at HERA	5
2.1	Kinematics of DIS	5
2.2	DIS cross section	6
2.3	Cross section and structure function at low Q^2	9
2.4	The quark momentum distribution in QCD models	9
2.5	Parton densities at low x	13
2.6	Radiative corrections	16
3	Determination of the kinematical variables	18
3.1	HERA kinematics	18
3.2	Electron only method	21
3.3	Hadronic measurement and mixed method	23
3.4	Double angle method	25
3.5	Influence of radiative corrections	26
3.5.1	Radiative corrections for the electron only method	27
3.5.2	Radiative corrections for the Jacquet-Blondel method	28
3.5.3	Making use of radiative events	28
4	HERA and the H1 detector	29
4.1	HERA machine	29
4.2	The H1 detector	30
4.2.1	Central Tracker	34
4.2.2	Backward electromagnetic calorimeter, BEMC	47
4.2.3	Trigger and data acquisition	49
5	The Data	51
5.1	Event selection	51
5.2	Vertex Determination	53
5.3	ϑ measurement	54

5.3.1	ϑ determination	54
5.3.2	ϑ resolution	54
6	The Background	56
6.1	Beam induced background	56
6.2	Photoproduction background	56
6.2.1	Classification of photoproduction events	57
6.2.2	Tagged events	59
6.2.3	Cut on the distance to the closest BPC hit	61
6.2.4	Cluster size distribution	69
6.2.5	Missing backward energy distribution	70
6.2.6	Using the tracker information	72
7	Results	83
7.1	Monte Carlo simulations	83
7.2	Binning	86
7.3	Acceptance	87
7.4	Measurement of F_2	89
7.5	Error considerations	90
7.6	Proton structure function F_2	92
8	Summary	101
A	ϑ resolution	103
B	List of systematical errors	107
C	Comparison with H1 results	110

Zusammenfassung

Diese Arbeit beschreibt die Messung der Strukturfunktion des Protons F_2 im kinematischen Bereich von $3 \times 10^{-4} \leq x \leq 10^{-2}$ und $8.5 \leq Q^2 \leq 60 \text{ GeV}^2$. Die Messung beruht auf den Daten, die von H1 am HERA Speicherring am DESY 1993 gemessen worden sind und entspricht einer totalen integrierten Luminosität von 253 nb^{-1} mit etwa 16000 Ereignissen. Der Schwerpunkt dieser Arbeit liegt in der Unterdrückung des Untergrundes von Photo-produktionsereignissen, die den Bereich von kleinen Energien des gestreuten Elektrons dominieren, mit Hilfe der Spurkammern. Die dazu notwendigen Detektorkomponenten werden im Detail vorgestellt.

Die x -Abhängigkeit der Proton-Strukturfunktion wird für acht verschiedene Bereiche von Q^2 und zwei verschiedene Methoden zur Bestimmung der Lorentz-invarianten Variablen x, y und Q^2 gezeigt. Beide Methoden stimmen sehr gut überein. Ein weiterer Vergleich mit den H1-Resultaten, die auf der Glasgow Konferenz gezeigt wurden, weist ebenfalls eine gute Übereinstimmung auf, und zeigt, dass die spezielle Behandlung des Untergrundes die Messung von einem zusätzlichen Punkt bei kleinem x zulässt. Die Strukturfunktion des Protons steigt mit abnehmendem x , was auf eine schnell wachsende Gluondichte hinweist.

Abstract

This thesis presents the analysis of the proton structure function F_2 in the kinematical domain of $3 \times 10^{-4} \leq x \leq 10^{-2}$ and $8.5 \leq Q^2 \leq 60 \text{ GeV}^2$. It is based on a total integrated luminosity of 253 nb^{-1} with roughly 16000 events, measured with the H1 experiment at the HERA collider in 1993.

The main emphasis lies on a reduction of the photoproduction background, which is dominant at low energies of the scattered electron, by making use of the tracking chambers. The detector components used for this analysis are presented in detail.

Two methods are used for the determination of the kinematical variables x, y and Q^2 , using either only the scattered electron or a combination of the electron and the hadronic system. The two methods agree nicely in the overlapping regions. The structure function F_2 is in agreement with the results presented by the H1 collaboration and allows to extend the measurement to lower x . It shows a rise of F_2 with decreasing x indicating a rising gluon density.

Chapter 1

Introduction

Deep inelastic lepton nucleon scattering played a dominant role in understanding the structure of the nucleon for the last 25 years. Starting in the late sixties at SLAC with the discovery, that nucleons are composed out of point-like objects called partons [1], [2], the fundament was laid for Quantum Chromodynamics (QCD) [3] to become the theory for the strong interaction. In the quark parton model the partons are identified with quarks with spin $1/2$ and a charge of multiples of one third of the charge of the electron [4]. Further experiments showed that the quarks carry only half of the momentum of the nucleon [5], the remaining momentum is carried by the gluons, which are the exchange particles of the strong interaction, and sea quarks. The predictions of QCD were tested in various experiments.

At the end of 1991 the first electron proton collider HERA came into operation, providing collisions between 26.7 GeV electrons and 820 GeV protons. Compared to previous fixed target experiments, HERA as a colliding experiment has a much higher center of mass energy which allows a momentum transfer from the electron to the struck quark of two orders of magnitude higher than previous experiments.

Therefore the proton structure function F_2 and hence the distribution of the valence quark, sea quark, and gluon densities can be measured in a wide kinematical range. The high center of mass energy allows on one side to have a very high momentum transfer, making the exchange of the weak exchange boson Z_0 visible and resolve structures down to 10^{-18}m , and on the other side to measure in a region with a very low x , which is the momentum fraction carried by the struck quark. This means entering a kinematical region of special significance for QCD effects, where it is expected that the momentum densities of the gluons and therefore the sea quarks increase. At even lower x non-perturbative effects such as saturation and shadowing should show up.

In 1992 the two detectors H1 and Zeus started data taking. One of the first analyses based on this first years data was the determination of the proton structure function in the previously unexplored region of low x . The results of the two experiments, though with large statistical and systematical errors, showed a rise of F_2 with decreasing x , already being an indication

for a fast growing of the gluon density towards low x . Owing to the almost 4π coverage of the H1 detector the deep inelastic scattering measurement allows also a precise study of the hadronic system.

The much higher statistics available in 1993 allowed to measure the structure function with reduced statistical and systematical errors and a much finer binning in x and Q^2 .

This analysis presents the measurement of the proton structure function at low x with a special emphasis on background contamination.

Chapter 2 gives an overview of the theoretical background for the measurement of the differential cross section and the proton structure function.

Chapter 3 discusses the kinematics of the deep inelastic scattering process at HERA. Different methods for determining the kinematical variables from the measured quantities are presented. In contrast to previous fixed target experiments not only the scattered electron is measured, but also the hadronic system. A combination of all the information allows to extend the kinematical region accessible at HERA and to cross-check the results and systematical errors obtained with different analyses.

Chapter 4 shortly describes the H1 detector. The components used for this analysis and their behaviour in the 1993 running period are discussed in detail.

Chapter 5 describes the selection of the event sample with an emphasis on the angular resolution.

Chapter 6 is dedicated to the discussion of background contamination of the event sample. Several methods for background suppression are compared. Finally a method is presented which uses the innermost tracking chambers. It allows to reject part of the background and to estimate the remaining background from data.

Chapter 7 discusses the measurement of the proton structure function for two different methods with regards to the determination of the kinematics. The results are compared with the standard H1 analysis and to different parametrizations.

Chapter 8 finishes with a summary of this analysis.

Chapter 2

Deep inelastic scattering at HERA

Deep inelastic scattering (DIS) of leptons has played an important role in probing the structure of the nucleons and gave fundamental informations on electromagnetic, weak, and strong interactions at the quark parton level. At HERA the very high center of mass energy allows to measure structures in the proton with a spacial resolution of 10^{-18} m and opens a completely new kinematic domain.

2.1 Kinematics of DIS

Neutral current DIS takes place via the exchange of a γ or Z_0 , the neutral exchange bosons of the electroweak interaction (charged current processes have only the charged weak bosons W^\pm). The scattering process can be described as $e + p \longrightarrow l + H$ where e, p, l and H denote the incoming electron and proton, the scattered lepton, and the final state hadron system respectively. The process is illustrated in Figure 2.1, the abbreviations for momenta and energies used in the following are summarized in Table 2.1. The total invariant mass squared (s) of the system is given by the square of the four momenta of the incoming or outgoing particles:

$$s = (k + P)^2 = (k' + p_H)^2 = 4 \cdot E_e E_p = 4 \cdot E_H E' \quad (2.1.1)$$

if the masses of the electron, proton and the scattered lepton can be neglected.

Instead of the energies and angles specific to a given detector one commonly uses Lorentz-invariant variables (x , y and Q^2) which allow a better comparison between different experiments:

$$\begin{aligned} Q^2 &=: -q^2 =: -(k - k')^2 = -(P - P_H)^2 \\ y &=: \frac{q \cdot P}{k \cdot P} \quad \text{and} \quad x =: \frac{Q^2}{2P \cdot q}, \end{aligned} \quad (2.1.2)$$

where x , y , and Q^2 are correlated via $Q^2 = xys$.

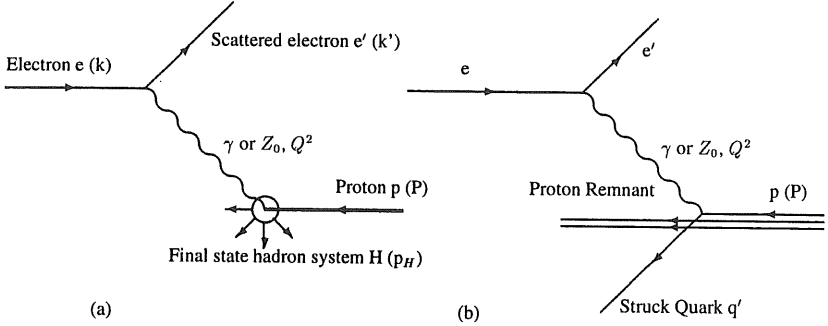


Figure 2.1: Deep inelastic electron proton scattering (a) without any further assumptions on the proton structure and (b) in the quark parton model.

Q^2 is the negative four momenta squared (q^2) transferred from the electron to the proton and y describes the relative energy loss of the electron in the rest frame of the proton. In the quark parton model (QPM) x is understood as the momentum fraction of the proton momentum carried by the struck quark in a system, where the proton momentum is very large. The reconstruction of x , y and Q^2 from the angles and energies of the scattered particles is discussed in more detail in chapter 2.

particle description	particle name	four momenta	energy
incoming electron	e	k	E_e
incoming proton	p	P	E_p
scattered lepton, e or ν	l	k'	E'
final hadron system	H	p_H	E_H

Table 2.1: Abbreviation for the DIS process.

2.2 DIS cross section

In leading order electroweak theory the differential cross section for DIS with γ or Z_0 exchange can be written as [8]:

$$\frac{d^2\sigma_{NC(ep)}}{dx dQ^2} = \frac{4\pi\alpha^2}{xQ^4} \left(y^2 x F_1 + (1-y)F_2 + \left(y - \frac{y^2}{2}\right)x F_3 \right)$$

$$= \frac{2\pi\alpha^2}{xQ^4} \left((1 + (1-y)^2) F_2 - y^2 F_L + (1 - (1-y)^2) xF_3 \right) \quad (2.2.3)$$

with the three structure functions F_2 , F_3 , and F_L or xF_1 all depending on x and Q^2 . F_2 is the proton structure function and F_3 describes the non parity conserving part of the cross section. F_L , which describes the interaction with longitudinal polarized photons, is defined by F_2 and the transversal structure function xF_1 :

$$F_L = F_2 - 2xF_1. \quad (2.2.4)$$

It is equal to zero for spin 1/2 particles (Callan-Gross relation [9]) as long as the quark masses and the intrinsic transverse momenta are neglected ([8]). However, higher order QCD effects change this relation and make the longitudinal structure function proportional to α_s , the strong coupling constant. In a good approximation this can be neglected except for very small x [10],[38].

F_2 and F_3 can be written in the quark parton model in terms of the probability of finding a quark (antiquark) of flavour f with the momentum fraction x ($q_f(x, Q^2)$, $\bar{q}_f(x, Q^2)$). They have a logarithmic Q^2 behaviour as will be shown in the next section. In the QPM the structure functions are given by [8]:

$$\begin{aligned} F_2(x, Q^2) &= \sum_{flavours} (xq_f(x, Q^2) + x\bar{q}_f(x, Q^2)) \cdot A_f(Q^2) \\ xF_3(x, Q^2) &= \sum_{flavours} (xq_f(x, Q^2) - x\bar{q}_f(x, Q^2)) \cdot B_f(Q^2), \end{aligned} \quad (2.2.5)$$

where the sum runs over all flavours in the proton.

The coefficients A_f and B_f for the quark flavours are given below, separated into contributions from pure γ or pure Z_0 exchange and γ/Z_0 interference in terms of the charge of the electron (e_f) and the neutral current vector and axial vector couplings a and v (a_e and v_e for the electron and a_f , v_f for a quark with flavour f):

$$\begin{aligned} A_f^{L,R} &= \overbrace{e_f^2}^1 - \overbrace{2e_f(v_e \pm a_e)v_f P_z}^2 + \overbrace{(v_e \pm a_e)^2(v_f^2 + a_f^2)P_z^2}^3 \\ B_f^{L,R} &= \overbrace{\mp 2e_f(v_e \pm a_e)a_f P_z}^{2'} + \overbrace{(v_e \pm a_e)^2 v_f a_f P_z^2}^{3'} \\ & \quad (1: \text{pure } \gamma \text{ exchange } \quad 2, 2': \gamma/Z_0 \text{ interference } \quad 3, 3': \text{pure } Z_0 \text{ exchange}) \end{aligned} \quad (2.2.6)$$

where \pm corresponds to left (L) and right (R) handed electrons. B_f has only terms coming from the weak interaction since it is not parity conserving.

P_z gives the strength of the Z_0 exchange term and depends on the mass of the exchange boson Z_0 . The relative contribution of pure Z_0 and γ/Z_0 interference then becomes:

$$\frac{\gamma/Z_0}{\gamma} \propto P_z = \frac{Q^2}{Q^2 + M_Z^2} \quad \text{and} \quad \frac{Z_0}{\gamma} \propto P_z^2 = \left(\frac{Q^2}{Q^2 + M_Z^2} \right)^2. \quad (2.2.7)$$

The ratio of the part of the cross section belonging to the weak interaction and the pure γ cross section is plotted in Figure 2.2, showing that the corrections to the pure γ exchange become only important for high Q^2 and dominate the cross section above $Q^2 = 10^4 \text{ GeV}^2$. In this analysis we are interested in the low and intermediate Q^2 domain and we therefore neglect the contribution of the weak interaction.

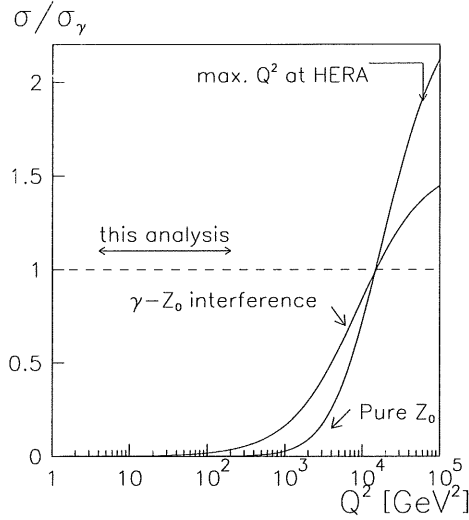


Figure 2.2: Relative contribution of Z_0 exchange and γ/Z_0 interference to pure γ exchange as a function of Q^2 .

Figure 2.2 shows that the high center of mass energies available at HERA allows for the first time a direct measurement of the Z_0 exchange. However, since the cross section in Formula 2.2.3 is proportional to $1/Q^4$ the higher Q^2 region needs high luminosity to get a reasonable number of events. Due to the limited statistics this analysis is restricted to an event sample with Q^2 less than 100 GeV^2 , where the weak interaction can safely be neglected.

The charged current-cross section taking place via the exchange of a charged boson W^\pm can be deduced directly from above formulas. The only remaining contribution is coming

from the weak interaction and is therefore suppressed in the low and intermediate Q^2 region with respect to the neutral current cross section by

$$\left(\frac{Q^2}{Q^2 + M_W^2} \right)^2,$$

making the charged current events visible at very high Q^2 only.

2.3 Cross section and structure function at low Q^2

As it has been shown above the cross section can be expressed in good accuracy by γ exchange alone for Q^2 below 500 GeV². The coefficients in 2.2.5 are then given by the photon propagator

$$A_f = e_f^2, \quad B_f = 0 \quad \text{with } e_f = \text{charge of the quark with flavour } f.$$

It is convenient to rewrite 2.2.3 by making use of a new definition which describes the contribution of the longitudinal structure function:

$$R = \frac{\sigma_L}{\sigma_t} = \frac{F_L}{2xF_1} = \frac{F_L}{F_2 - F_L}. \quad (2.3.8)$$

R gives the ratio of the longitudinal (σ_L) and transversal (σ_t) cross section. In the limit $Q^2 \rightarrow 0$ where the photon is becoming real σ_L goes to 0.

2.2.3 then becomes:

$$\begin{aligned} \frac{d^2\sigma}{dx dQ^2} &= \frac{2\pi\alpha^2}{xQ^4} \left((1 + (1-y)^2) F_2 - y^2 F_L \right) \\ &= \frac{2\pi\alpha^2}{xQ^4} \left(2(1-y) + \frac{y^2}{1+R} \right) F_2 \\ &= \frac{2\pi\alpha^2}{xQ^4} \left(2(1-y) + \frac{y^2}{1+R} \right) \sum_{\text{flavours}} e_f^2 \left(xq_f(x, Q^2) + x\bar{q}_f(x, Q^2) \right) \end{aligned} \quad (2.3.9)$$

2.4 The quark momentum distribution in QCD models

It was seen in Formula 2.3.9 that a measurement of F_2 gives us insight into the quark and antiquark distributions (q_f and \bar{q}_f) of the proton, depending on both x and Q^2 . In first order perturbative QCD we have to include gluon radiation processes and gluon quark pair conversion in addition to the valence quark scattering. The Feynman graphs for the three first order processes are shown in Figure 2.3. (a) and (b) show initial and final state gluon radiation respectively and c) scattering at sea quarks which are produced by conversion of gluons. First evidence for the gluons was found in 1970, by observing a violation of the momentum sum rule in a comparison of electron-proton and electron-neutron scattering.

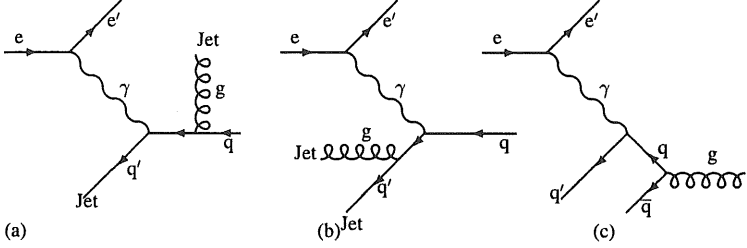


Figure 2.3: Lowest order QCD corrections: (a) initial state, (b) final state gluon radiation and (c) boson gluon fusion.

The corrections to the quark momentum distributions due to initial state gluon emission were calculated in leading log approximation $LL(Q^2)$ by Altarelli and Parisi [12] (AP equation) and by Dokshitzer, Gribov and Lipatov [13]. The correction can be expressed in terms of the probability of a quark carrying a momentum fraction ξ (with $1 > \xi > x$) and the splitting function $P(\frac{x}{\xi})$,

$$\Delta F_2 = x \frac{\alpha_s}{2\pi} \sum_{flavours} \left(e_f^2 \int_x^1 \frac{d\xi}{\xi} q_f(\xi) P_{qq}(\frac{x}{\xi}) \log Q^2 + \text{terms of order } \alpha_s^2 \right). \quad (2.4.10)$$

Similarly the scattering at sea quarks can be included. The form of the splitting functions for four different processes is given below in Table 2.2.

Taking into account both quarks with initial state gluon radiation and quark pairs produced from gluons we get for the variation of the quark and the gluon density (denoted by $g(x, Q^2)$) [14]:

$$\frac{\partial q(x, Q^2)}{\partial(\log Q^2)} = \frac{\alpha_s}{2\pi} \int_x^1 \frac{d\xi}{\xi} (P_{qq}(\frac{x}{\xi}) q(\xi, Q^2) + P_{qg}(\frac{x}{\xi}) g(\xi, Q^2)) \quad (2.4.11)$$

usually written as :

$$\frac{\partial q(x, Q^2)}{\partial(\log Q^2)} = P_{qq} \otimes q + P_{qg} \otimes g \quad (2.4.12)$$

and similarly for the gluon density

$$\frac{\partial g(x, Q^2)}{\partial(\log Q^2)} = P_{gq} \otimes q + P_{gg} \otimes g$$

known as GLAP (Gribov, Lipatov, Altarelli and Parisi [12] [13]) equation. A different notation separates the quark distribution in flavour singlets ($q^s = q + \bar{q}$) and non singlets (q^{ns} : containing the valence quarks):

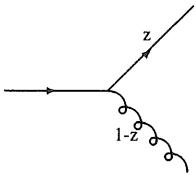
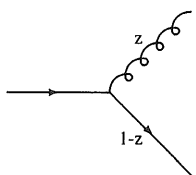
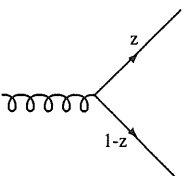
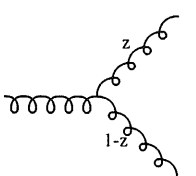
<p>1) $P_{qq} = \frac{4}{3} \frac{1+z^2}{1-z}$</p> 	<p>2) $P_{gq} = \frac{4}{3} \frac{1+(1-z)^2}{z}$</p> 
<p>3) $P_{gg} = \frac{1}{2}(z^2 + (1-z)^2)$</p> 	<p>4) $P_{gq} = 6\left(\frac{z}{1-z} + \frac{1-z}{z} + z(1-z)\right)$</p> 

Table 2.2: Splitting function for different processes with gluon radiation in LLA(Q^2). z denotes the fraction of the incident four momenta: $z=x/\xi$ carried by the parton in question.

$$\begin{aligned}
 \frac{\partial q^{ns}}{\partial(\log Q^2)} &= \frac{\alpha_s}{2\pi} P_{qq} \otimes q^{ns} \\
 \frac{\partial q^s}{\partial(\log Q^2)} &= \frac{\alpha_s}{2\pi} (P_{qq} \otimes q^s + P_{gq} \otimes g) \\
 \frac{\partial g}{\partial(\log Q^2)} &= \frac{\alpha_s}{2\pi} (P_{gg} \otimes g^{ns} + P_{gq} \otimes q)
 \end{aligned} \tag{2.4.13}$$

The evolution of the GLAP equation therefore gives us the evolution of the quark and gluon densities in Q^2 in first order perturbative theory once the quark and gluon densities at a fixed Q^2 (Q_0^2) as a function of x are known.

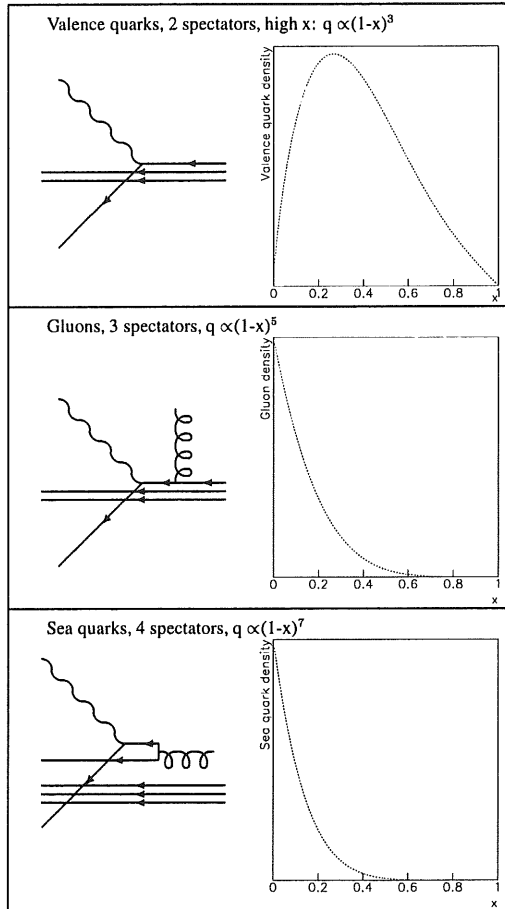


Table 2.3: Naive estimate for the quark and gluon density as a function of x in arbitrary units.

2.5 Parton densities at low x

It was shown that the Q^2 evolution from a given x distribution at Q_0^2 can be extracted using the GLAP equations. The evolution towards low x is a priori not known and subject to different models. It is clear that towards $x = 1$ the quark density is dominated by the valence quark density, whereas for low x sea quarks and gluons play a dominant role.

The high- x behaviour of $q_f(x)$ is defined by the number of spectators (n_s) [14]:

$$q_f(x) \propto (1-x)^{2n_s-1} \quad (2.5.14)$$

The valence part declines towards $x = 0$ with $xq_v \propto x^{0.5}$. This naive estimation of the x behaviour for different processes is illustrated in Table 2.3.

Although there is no firm theory yet which describes the low x behaviour, we can use the GLAP equations to derive x distributions from a given distribution at Q_0^2 . It turns out that this way the GLAP equations produce steeper and steeper x distributions when going to higher Q^2 [15]. Several models exist which differ by the starting distributions at Q_0^2 . The low x behaviour is determined for different parametrizations by fitting the models to the existing data at high x and extrapolating them towards lower x . Some of the commonly used parametrizations are summarized in Table 2.4. The MRS parametrizations have a total of 16 free parameters for the starting distributions of the quark and gluon densities at $Q_0^2 = 4 \text{ GeV}^2$. As an example for the effect of different starting distributions on the evolution towards low

name	assumptions
MRS ^{0'} [18]	$\bar{u} = \bar{d}$, $q_f(x, 4 \text{ GeV}^2) = \text{constant}$ very simple method, NMC already showed that $\bar{d} > \bar{u}$
MRS ^{D0'} [18]	$u \neq d$, $q_f(x, 4 \text{ GeV}^2) = \text{constant}$
MRS ^{D-'} [18]	$u \neq d$, $xq, x\bar{q} \propto x^{-0.5}$ at $Q_0^2 = 4 \text{ GeV}^2$
MRS ^H [19]	same as MRS ^{D-} but fitted to published HERA data
CTEQ [20]	u , d , and s are freely parametrized and not strongly coupled to the gluon density, in total 30 parameters. CTEQ2M starts with a constant ($xq(x, Q_0^2) = \text{const.}$) and CTEQ2MS with a singular ($xq(x, Q_0^2) \propto x^{-0.5}$) quark distribution.
GRV [21]	small x partons are radiatively generated according to the Altarelli Parisi equation, starting from valence quark and gluon distributions at $Q_0^2 = 0.3 \text{ GeV}^2$

Table 2.4: Different parametrizations for quark densities.

x , Figure 2.4 shows the quark and gluon densities at $Q^2 = 20 \text{ GeV}^2$

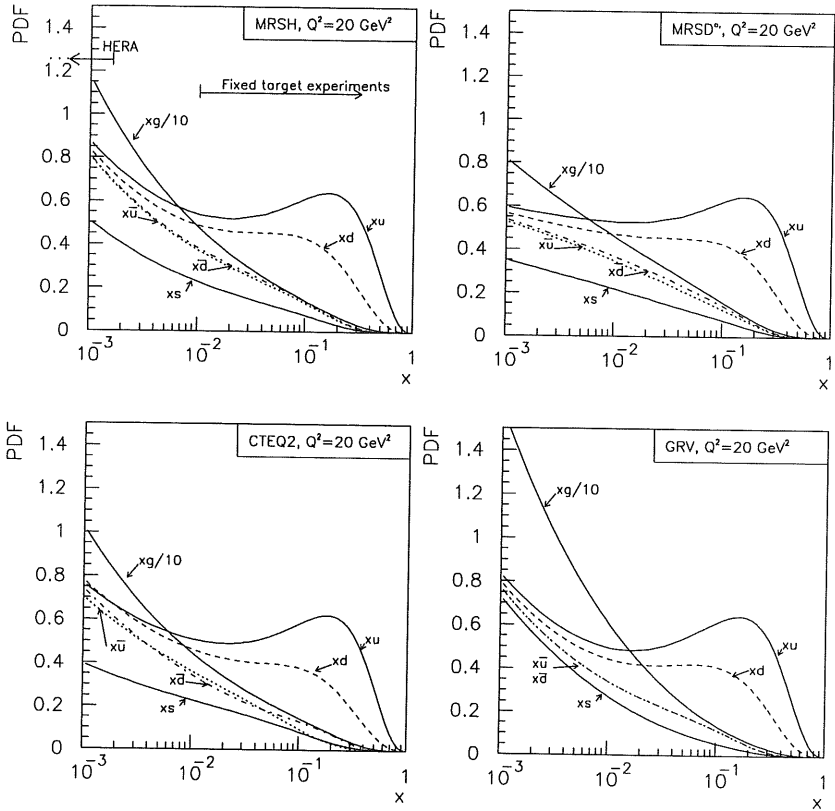


Figure 2.4: Quark and gluon densities for four different parametrizations at $Q^2 = 20 \text{ GeV}^2$. MRSD^{0'} assumes a flat starting distribution at $Q_0^2 = 4 \text{ GeV}^2$ ($xg, xq = \text{const}$), whereas CTEQ and MRSH start with a singular distribution ($xg, xq \propto x^{-0.5}$). GRV generates the sea quarks radiatively from a given valence quark and gluon distribution at $Q_0^2 = 0.3 \text{ GeV}^2$. The four parametrizations agree in the region of the fixed target data ($x > 0.01$) but differ much in the region accessible with HERA ($x < 0.001$).

for the MRSD^{0'} MRSH, CTEQ2 and GRV parametrization. Data was available for x larger than 0.01 (except for MRSH). In this region the quark and gluon distributions do not differ much. All are dominated by the valence quark distributions. Coming to low x however the four models differ significantly. Since the structure function F_2 is essentially the sum of the quark distributions, this results in a large difference in the prediction of F_2 . This is illustrated in Figure 2.5 which shows the prediction for F_2 at $Q^2=20 \text{ GeV}^2$ extrapolated from the fixed target data to the x range of HERA.

Clearly this picture cannot hold for very low x , otherwise the gluon density would rise to

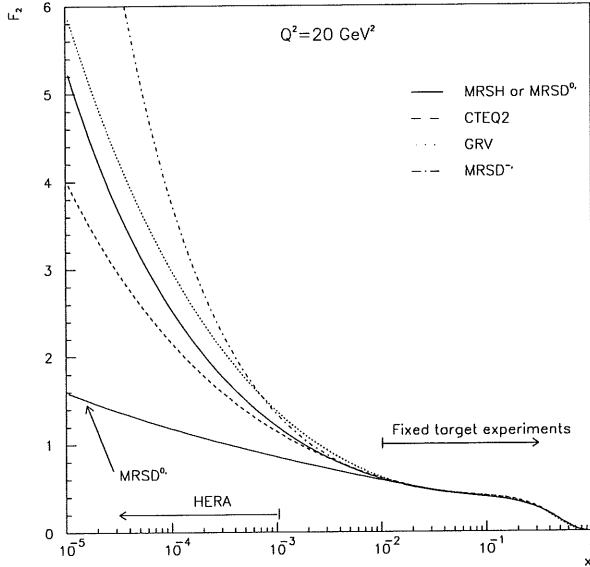


Figure 2.5: Predictions for F_2 at $Q^2 = 20 \text{ GeV}^2$ obtained from different sets for the parton density distributions (see text).

infinity. One has to take into account recombination of gluons. This is done by adding a nonlinear term proportional to R^{-2} in the evolution equation [16], [17]. The radius R determining the strength of the nonlinear term denotes the size of the region inside the proton from which the recombining gluon originates. Naturally it cannot exceed the proton radius of 5 GeV^{-1} . Two different assumptions exist:

- the gluons are homogeneously spread in the proton and hence recombination is observed at very low x , $R=5 \text{ GeV}^{-1}$.
- gluons cluster in so called 'hot spots' around the valence quarks. Therefore the critical

density is reached at higher x .

The above discussions show that the structure function measurement at HERA enters a very interesting kinematical region:

- at HERA we can measure at $x > 10^{-4}$. We therefore expect to see a rising of the structure function F_2 towards lower x due to the rise of the gluon and therefore the sea quark density.
- if saturation takes place in so called hot spots, it should happen at higher x and might be detectable at HERA .

2.6 Radiative corrections

So far only QCD effects were discussed, electroweak corrections to the cross section arising out of the emission of an additional real photon, which is independent on the QCD evolution of the partons, were neglected. These QED contributions do not contain additional information

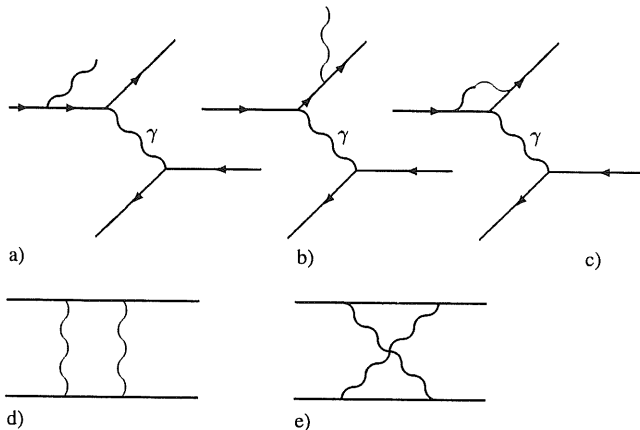


Figure 2.6: First order radiative corrections, no weak contributions are shown. The emission of the photon may happen at the quark or the electron line, therefore they are not further specified. (a) and (b) illustrate initial and final Bremsstrahlung, (c) corrections to the vertex and (d) and (e) additional γ exchange between electron and quark.

about the electron quark interaction, therefore the structure function is deduced from the Born cross section σ_{Born} describing the pure electron proton scattering. Hence the radiative

corrections have to be subtracted from the measured cross section. This means that a proper treatment of the corrections is imperative for a determination of the structure function. Two different methods were used at H1 and showed a good agreement. The first includes the radiative processes in the Monte Carlo simulation which allows the estimation of the corrections for each bin in x and Q^2 (HERACLES [22]), whereas the second one calculates the full order α corrections analytically using a program called TERAD [23], [24]. The first order corrections are obtained by attaching a single photon to each charged fermion line. The different processes are illustrated in Figure 2.6, they include real photon emission of the incoming or outgoing electron or quark (a) and (b) as well as virtual corrections to the vertex (c), and photon exchange between quark and electron (d) and (e). At high Q^2 also weak corrections have to be applied but they can be neglected due to their $\frac{1}{Q^2+M_Z^2}$ suppression [25] in the low Q^2 region. An evolution in $\alpha = \frac{1}{137}$ of the measured cross section explicitly shows the corrections to the Born cross section:

$$\begin{aligned}\sigma_{Born} &= \sigma_0 + \frac{\alpha}{2\pi} A_1 + \left(\frac{\alpha}{2\pi}\right)^2 A_2 + \dots \\ &= \sigma_{Born}(1 + \delta_1 + \delta_2 + \dots)\end{aligned}\quad (2.6.15)$$

where A_i is given by the sum of all Feynman graphs of the order i . A good approximation is already reached in first order since α is much smaller than 1:

$$\sigma_{exp} = \sigma_{Born} \frac{1}{1 + \delta_1} + \text{terms of order } \alpha^2. \quad (2.6.16)$$

The first order corrections can be calculated using the Weizsäcker-Williams approximation in leading log (LLA) [26], [27]. The first order corrections at the electron line for example are given by [28]:

$$\delta_1 = \frac{\alpha}{\pi} \left(\frac{3}{2} \ln \frac{Q^2}{m_e^2} - 2 - \left(\ln \frac{Q^2}{m_e^2} - 1 \right) \ln \frac{EE'}{\Delta E^2} + R \right) \quad (2.6.17)$$

with R small and ΔE the maximal photon energy. Due to the factor $1/m^2$ corrections at the quark line are suppressed and will not be discussed further. The remaining contribution arise out of initial and final state Bremsstrahlung of the electron. The size of the corrections crucially depends on the method used for the reconstruction of the kinematical variables and will be discussed in the next chapter.

Chapter 3

Determination of the kinematical variables

3.1 HERA kinematics

A major advantage of HERA structure function measurement is its redundancy arising from the simultaneous measurement of the scattered electron and the hadrons. With the incident beam energies known (electron beam: E_e , proton beam: E_p) one only needs two variables to describe the scattering process:

$$\text{electron} + \text{proton} \rightarrow \text{electron}' + \text{hadronic system} .$$

In the H1 coordinate system (positive axis corresponds to the proton direction) the four momenta of incoming electron (k), proton (P), scattered electron (k'), and the current jet (P_J) - which develops through fragmentation from the struck quark - become:

$$k = \begin{pmatrix} E_e \\ 0 \\ 0 \\ -E_e \end{pmatrix} \quad k' = \begin{pmatrix} E' \\ E' \sin \vartheta \\ 0 \\ E' \cos \vartheta \end{pmatrix} \quad P = \begin{pmatrix} E_p \\ 0 \\ 0 \\ E_p \end{pmatrix} \quad P_J = \begin{pmatrix} E_{Jet} \\ -E_{Jet} \sin \gamma \\ 0 \\ E_{Jet} \cos \gamma \end{pmatrix} \quad (3.1.1)$$

if the scattering process is defined to take place in the $x - z$ plane. E' , E_{Jet} , ϑ , and γ denote the energy and angle of the scattered electron and current jet respectively. Conventionally fixed target experiments used the energy and the angle of the scattered electron, whereas charged current events with the neutrino not detected had to be analysed using the hadronic information. At HERA we can choose the appropriate combination of the measured variables depending on the kinematical range of the measurement which allows a cross-check of the results in the overlapping region. The different methods are shortly discussed in the following sections, more detailed informations are found in [29], [30], and [31].

The four observables of the DIS process are energy and angle of the scattered electron and the

current jet. In Figure 3.1 (a)-(d) lines of constant energy and angle of the scattered electron and the current jet are drawn in the x - Q^2 plane. The most striking features are:

- Lines of constant energy of the scattered electron: a large kinematical region has energies between 25 and 30 GeV. This fact makes a x determination using the electron energy and angle not useful for low y ($y < 0.1$). Nevertheless this region of almost constant energy - referred to as kinematical peak- proved to be very useful for a calibration of the backward electromagnetic calorimeter (BEMC), see Section 4.2.2, since the peak position and its distribution towards high x (and high energies) is almost independent of different parametrizations [32].
- Lines of constant electron angle: due to the $1/Q^4$ dependence of the cross-section the bulk of the events is situated at large scattering angles and mainly detected in the BEMC. Its angular acceptance is shown in dashed lines. Events at very low Q^2 ($Q^2 \leq 4 \text{ GeV}^2$) are lost since the electron escapes through the beampipe. The fact that the ϑ -lines are running almost parallel to the x axis makes the x determination almost independent of the ϑ -resolution.
- Lines of constant jet energy: the region at very low x and low Q^2 cannot be used, because the jet energy is too low. It becomes clear that the double energy method which reconstructs x and Q^2 using the energies of the scattered electron and the jet is not useful, except for very high x ($x > 0.1$), because the lines of constant energy of the jet and the scattered electron often run almost parallel.
- Lines of constant jet angle: in the interesting region of very low x the current jet starts to point backwards. This implies possible misidentification of the electron and a bad hadronic measurement because part of the hadrons may be lost in the beampipe and others badly measured in the BEMC. This fact essentially reduces the kinematical region accessible with a hadronic measurement to $y < 0.5$. At very low y ($y < 0.02$) the hadrons are lost in the forward beampipe.

The four observables leave us with six possible combinations for a reconstruction of x , y and Q^2 . The double energy method and two combinations which give double solutions ((E', γ) and (E_{Jet}, ϑ) [31]) will not be discussed further.

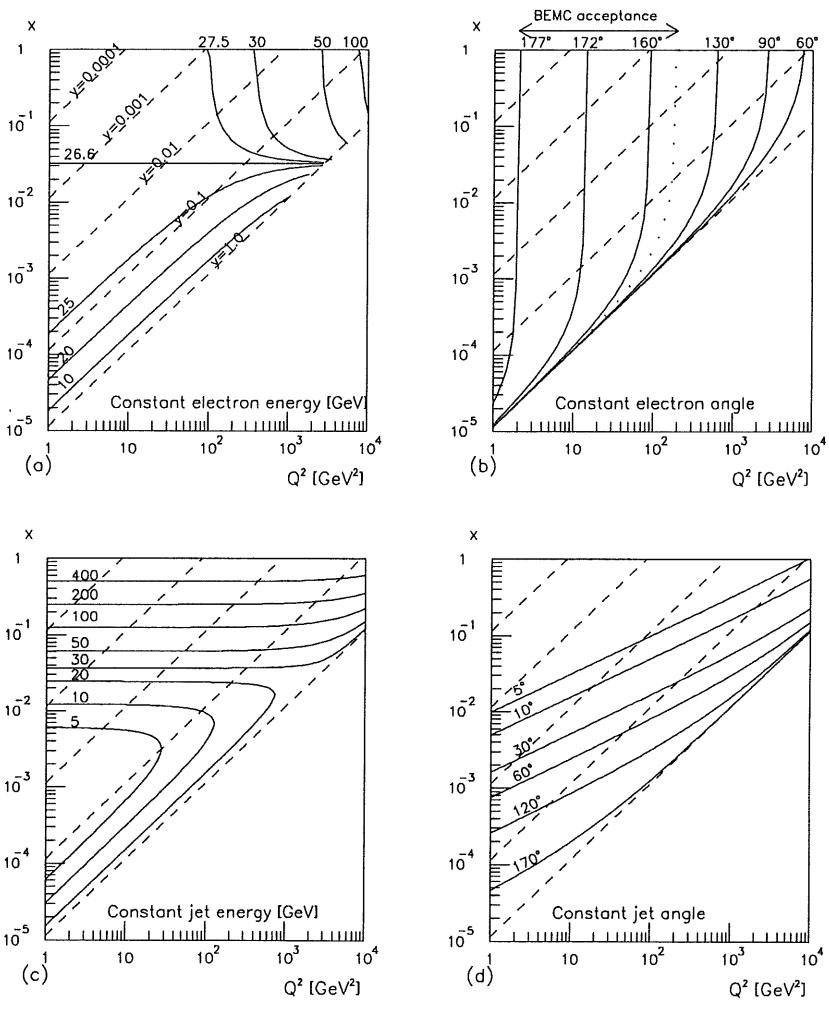


Figure 3.1: Kinematics at HERA lines of constant energy and scattering angle in the x - Q^2 plane, different values of y are plotted as dashed lines. (a) lines of constant energy of the scattered electron, showing a large range with almost constant energy. (b) constant scattering angle of the electron and (c) lines of constant jet energy and jet angle (d).

3.2 Electron only method

Deducing the kinematical variables x , y and Q^2 from a measurement of the energy and angle of the scattered electron is the conventional method for structure function measurements. By putting the four momenta defined above (3.1.1) into the definition for x , y and Q^2 (2.1.2), and neglecting the masses of the electrons and quarks we immediately get:

$$Q_e^2 = 4E_e E' \cos^2 \frac{\vartheta}{2} \quad y_e = 1 - \frac{E'}{E_e} \sin^2 \frac{\vartheta}{2} \quad x_e = \frac{Q_e^2}{s y_e}. \quad (3.2.2)$$

Taking the derivatives of the measured quantities, we easily get the resolutions:

$$\frac{\delta Q_e^2}{Q_e^2} = \frac{dE'}{E'} + \tan \frac{\vartheta}{2} d\vartheta \quad (3.2.3)$$

$$\frac{\delta x_e}{x_e} = \frac{1}{y_e} \frac{dE'}{E'} + \tan \frac{\vartheta}{2} \left(x_e \frac{E_p}{E_e} - 1 \right) d\vartheta$$

These resolutions and their kinematical dependence were studied by a comparison of the reconstructed and the generated value of x , y , or Q^2 , using a detailed simulation of the H1 detector:

$$\delta_{Q^2} = \frac{Q_{rec}^2 - Q_{gen}^2}{Q_{gen}^2} \quad \delta_x = \frac{x_{rec} - x_{gen}}{x_{gen}} \quad \text{and} \quad \delta_y = \frac{y_{rec} - y_{gen}}{y_{gen}}.$$

Figures 3.2a) and d) show that the Q^2 measurement is rather precise in the whole Q^2 range. It is reconstructed within 15% (HWHM) with a tendency to be shifted to values which are by 10% too low due to the energy reconstruction. It hardly varies with the energy (d) except for very low energies. Figure 3.2 (g) shows the probability to find the reconstructed Q^2 value within 15 % around the center of the distribution in (a) (hatched area), in the $x - Q^2$ plane indicating that a precise measurement is possible in a large kinematical range. A small drop in the quality of reconstruction is visible at low energies (high y) due to the less precise energy measurement. The resolution is mainly determined by the energy measurement (see Formula 3.2.3), only at very large scattering angles, i.e. low Q^2 , the ϑ resolution becomes important.

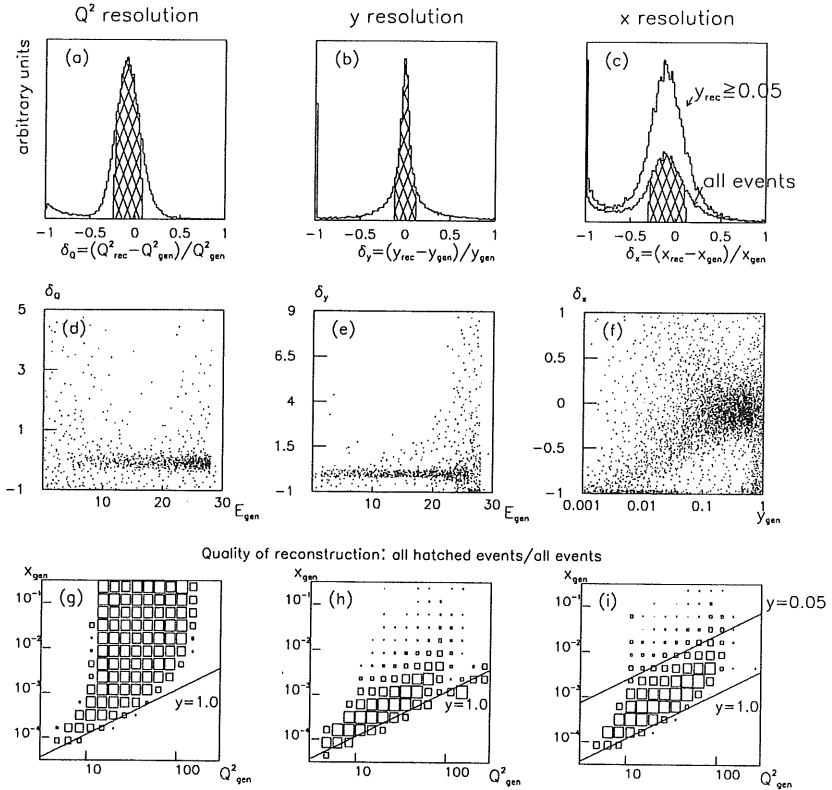


Figure 3.2: Resolution of the kinematical variables $-Q^2$ ((a),(d) and (g)), y ((b),(e) and (h)) and x ((c),(f) and (i)) for the electron only method. The plots (g)-(i) give the acceptance for events within one sigma of the measured resolution (hatched area in Figures (a)-(c) in the $x - Q^2$ -plane). The limit for a sensible x -determination ($y=0.05$) is indicated in Figure (h). The two curves in (c) are normalized to the peak value.

The y resolution is shown in Figures 3.2 (b), (e) and (h). It is determined by the energy measurement and therefore deteriorates in the region of the kinematic peak, clearly seen in Figure e) where the resolution versus energy is plotted. For energies below 25 GeV y is measured very accurately with a shift of less than 1% and a resolution of 12%.

The resolution for x (c) already indicates that there must be a large range with a very bad x -determination. This is expected from Formula 3.2.3 since the x measurement deteriorates due to the $1/y$ term (see also Figure (f)). Therefore this method is restricted to the high y region, with y typically larger than 0.05. The effect of this cut is illustrated in Figure 3.2 (c), the two curves are normalized to the peak value. With a cut at $y \geq 0.05$ the events with a meaningless reconstructed x value ($\delta x = -1$) disappear. (i) gives the acceptance for events with a good x -resolution, the cut at $y = 0.05$ is limiting the measurement to a kinematical region with good acceptance.

3.3 Hadronic measurement and mixed method

A hadronic measurement has to cope with the fact that energy and angle of the quark are not directly measurable. Access is limited to the hadronic final state after all fragmentation and hadronization processes. The jet which develops out of the struck quark still contains the information regarding its energy and angle, but their reconstruction is very sensitive to different algorithms defining a jet, lost particles and detector deficiencies.

Therefore a method was developed by F. Jacquet and A. Blondel [33] - it will further be referred to as Jacquet-Blondel - which makes use of the hadronic system without any jet identification.

Using energy and momentum conservation, the energy and momentum of the sum of all the hadrons is equal to the energy and momentum of the jet and to the quark:

$$P_{Quark} = \begin{pmatrix} E_{Quark} \\ -E_{Quark} \sin \gamma \\ 0 \\ E_{Quark} \cos \gamma \end{pmatrix} \longrightarrow P_{Jet} = \begin{pmatrix} E_{Jet} \\ -E_{Jet} \sin \gamma \\ 0 \\ E_{Jet} \cos \gamma \end{pmatrix} = P_h = \sum_{hadrons} \begin{pmatrix} E_h \\ p_{xh} \\ p_{yh} \\ p_{zh} \end{pmatrix} \quad (3.3.4)$$

By making use of two newly defined observables of the hadronic system Σ and T :

$$\Sigma = \sum_{hadrons} (E_h - p_{zh}) \quad T = \sqrt{\left(\sum_{hadrons} p_{xh} \right)^2 + \left(\sum_{hadrons} p_{yh} \right)^2} \quad (3.3.5)$$

and putting 3.3.4 and 3.1.1 into 2.1.2 we get for the kinematical variables:

$$y_{JB} = \frac{qP}{kP} = \frac{1}{2E_e} \sum_h (E_h - p_{zh}) = \frac{\Sigma}{2E_e} \quad (3.3.6)$$

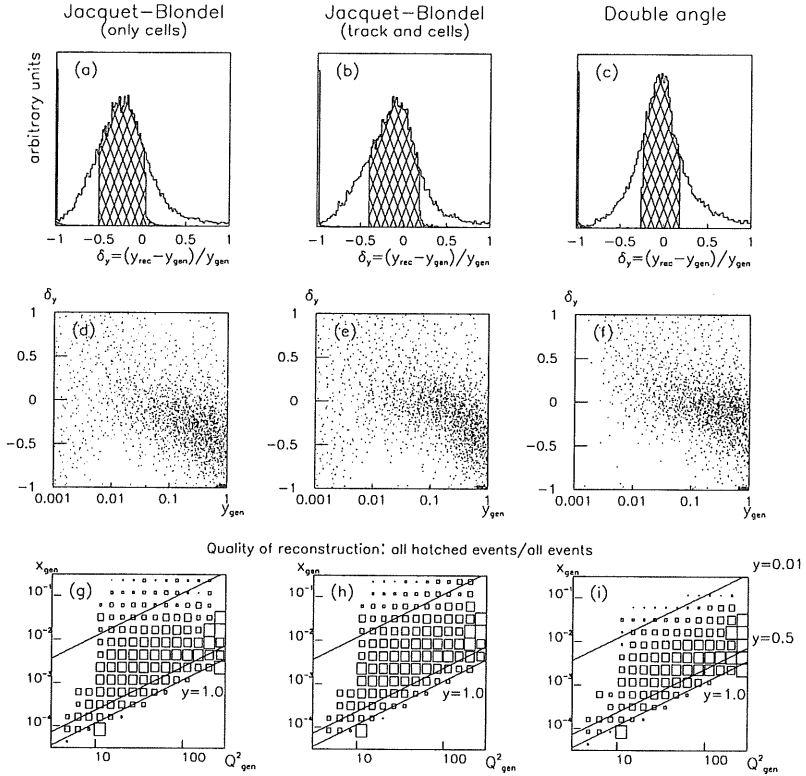


Figure 3.3: Resolution of the reconstruction of y using the Jacquet- Blondel and the double angle method.

$$Q_{JB}^2 = -(P - P_J)^2 = \frac{(\sum_h P_{xh})^2 + (\sum_h P_{yh})^2}{1 - y_{JB}} = \frac{T^2}{1 - y_{JB}}.$$

The advantage of this method is immediately clear from the above formulas. Hadrons emitted in the forward direction contribute only marginally to Σ and T and therefore particles lost in the forward beam hole hardly influence the measurement. This is not true for particles lost in the backward region, missing particles shift the reconstructed y_{JB} to lower values. To avoid the region with no accurate hadronic measurement usually a cut of $y < 0.5$ is applied.

The resolution depends on the errors of the energy and angle and the amount of particles lost and can only be checked by detailed simulations. The y resolution is shown in Figure 3.3 for two methods of calculating y . Method 1, labelled with 'only cells', corresponds to a pure calorimetric measurement with y determined by a summation over all calorimeter cells except

the cells belonging to the identified electron. Method 2 on the other hand uses a combination of tracks and cells which allows to include also very low energetic particles. Figure 3.3 (a) shows that method 1 suffers from a big shift of the order of 20% of the reconstructed y towards lower y , an effect reduced to 10% by using tracks and cells. This systematic shift is y dependent and largest at large y (see Figure 3.3 (d) and (e)) where the hadronic flow points backward and particles are lost. The resolution is worse than for the 'electron only' method (25% HWHM), but constant over a large range in x and Q^2 . This is illustrated in Figures 3.3 (g) and (h) where the fraction of events with a good resolution (hatched area) to all events is plotted. The two methods have the same acceptance region which is limited in the low y region by $y=0.01$, where the hadrons are lost in the forward beampipe and at very high y ($y>0.5$), with the hadrons pointing backward. The y measurement is fairly precise because the effect of lost energy is partly made up since the measured angle has a tendency to be shifted towards higher values [34].

The Q^2 measurement is less precise because T is severely influenced by the loss of particles, furthermore the resolution decreases with $1/(1 - y)$, making an accurate measurement impossible for small y .

Therefore the mixed method which uses the accurately measured Q^2 of the electron and y from the hadrons becomes the natural choice. Use of this method extends the measurable kinematical range down to $y=0.01$.

The mixed as well as the electron only method were already used in the first determination of the proton structure function by H1 with the 1992 data [35].

3.4 Double angle method

The lines of constant scattering angle of the electron and the quark cross each other with large angles and therefore allow a precise determination of y and Q^2 in a wide kinematical range. The main problem of the double angle method is the reconstruction of the polar angle of the jet (γ). It was shown in [31] that the angle can be calculated using the Jacquet-Blondel variables above.

$$\cos \gamma = \frac{Q_{JB}^2(1 - y_{JB}) - 4E_e^2 y_{JB}^2}{Q_{JB}^2(1 - y_{JB}) + 4E_e^2 y_{JB}^2} = \frac{\sum_h E_h \cos \gamma_h}{\sum_h E_h} \quad (3.4.7)$$

In first order this determination of the angle is independent of the energy, which proved to be the main advantage of the method, since at H1 presently the possible miscalibration of the hadronic energy of 5-7% is substantially contributing to the systematical error of the mixed method. The double angle method was used in the high Q^2 analysis by H1 [36] and as the main method in the ZEUS analysis [37].

$$Q_{da}^2 = 4E_e^2 \frac{\sin \gamma(1 + \cos \vartheta)}{\sin \gamma + \sin \vartheta - \sin(\gamma + \vartheta)} \quad y_{da} = \frac{\sin \vartheta(1 - \cos \gamma)}{\sin \gamma + \sin \vartheta - \sin(\vartheta + \gamma)} \quad (3.4.8)$$

The resolution of y_{da} is shown in Figures 3.3(c), (f) and (i) in comparison with the y deduced with the Jacquet-Blondel method discussed above. (c) and (f) show that the resolution is somewhat better (20% HWHM) and the systematic shift is considerably smaller (4% in average), a consequence of the independency of the energy scale. The kinematical region accessible with the double angle method is comparable with Jacquet-Blondel and fails for the same reasons as discussed above.

3.5 Influence of radiative corrections

It was shown in Section 2.6 that the main contribution to the radiative corrections comes from bremsstrahlung of the incoming (ISR=Initial State Radiation) and outgoing electron (FSR=Final State Radiation). The two processes are illustrated in Figure 3.4 with E_i and E_f denoting the energy of the incoming and outgoing electron and \hat{E}_i and \hat{E}_f their energy at the vertex. In the following x , y , and Q^2 describe the kinematical variables extracted under the

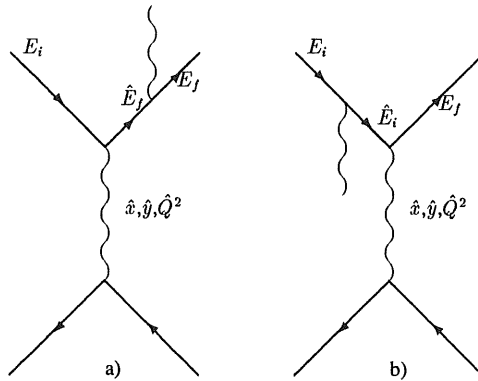


Figure 3.4: (a) Final state bremsstrahlung and (b) initial state bremsstrahlung of the electron.

assumption of a Born-event using the event topology and \hat{x} , \hat{y} , \hat{Q}^2 the true event kinematics.

$$\begin{aligned}
 E_i &\rightarrow \hat{E}_i = E_i - \gamma_i =: z_i E_i \\
 E_f &\rightarrow \hat{E}_f = E_f + \gamma_f =: \frac{1}{z_f} E_f
 \end{aligned}
 \tag{3.5.9}$$

with $0 \leq z_i, z_f \leq 1$.

The effect of ISR can be looked at as a deterioration of the beam energies and therefore affects all kinematical variables calculated under the assumption of fixed beam energies.

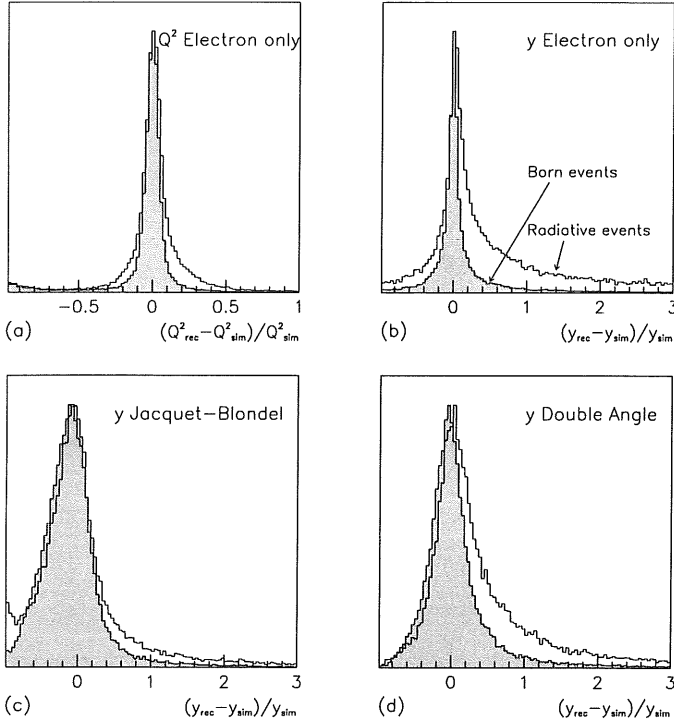


Figure 3.5: Effect of radiative corrections on the reconstruction of kinematical variables. The hatched histograms show the resolutions for non-radiative events, the empty histograms for events with initial state radiation.

3.5.1 Radiative corrections for the electron only method

The electron only method is heavily affected by initial state bremsstrahlung. Using the Formula 3.2.2 one gets

$$\begin{aligned}
 Q^2 &\rightarrow \hat{Q}^2 = z_i Q^2 \\
 y &\rightarrow \hat{y} = \frac{z_i + y - 1}{z_i} \\
 x &\rightarrow \hat{x} = \frac{z_i x y}{z_i + y - 1}
 \end{aligned}
 \tag{3.5.10}$$

shifting the events with initial state radiation to higher Q^2 and large y . To avoid events with catastrophic ISR a cut in y is necessary for the electron only method.

Final state bremsstrahlung is of minor importance since for 80% of the events the emitted

photons lie within a cone of 2 mrad of the scattered electron and are therefore not resolved in the calorimeter [38]. The remaining events transform to:

$$\begin{aligned} Q^2 &\rightarrow \hat{Q}^2 = \frac{1}{z_f} Q^2 \\ y &\rightarrow \hat{y} = \frac{z_f + y - 1}{z_f} \\ x &\rightarrow \hat{x} = \frac{xy}{z_f + y - 1}, \end{aligned} \quad (3.5.11)$$

again manifesting themselves at high y . The effect for the reconstruction of the kinematical variables is illustrated in Figure 3.5. The Q^2 determination is only slightly affected, but the reconstructed y is shifted towards high y .

3.5.2 Radiative corrections for the Jacquet-Blondel method

The Jacquet-Blondel method is differently affected by radiative corrections. In first order it is completely independent on FSR. Starting from Formula 3.3.6 the kinematical variables become with initial state bremsstrahlung:

$$\begin{aligned} Q^2 &\rightarrow \hat{Q}^2 = z_i Q^2 \frac{1-y}{z_i - y} \\ y &\rightarrow \hat{y} = \frac{y}{z_i} \\ x &\rightarrow \hat{x} = z_i x \frac{1-y}{z_i - y}. \end{aligned} \quad (3.5.12)$$

The amount of the corrections can be huge especially for the electron method at large y (see for example [39]). Regions with corrections exceeding 100% are avoided by a cut of $y_{el} \leq 0.6$. The corrections for the mixed method are much smaller and beyond 20% except for very large x .

3.5.3 Making use of radiative events

Radiative events can be identified by comparing the measurement of the electron and the hadronic system. This can be used first of all for a cross-check of the correct implementation of the radiative corrections, since after all the corrections have to be calculated in a region where the structure function is not known. Secondly these events - once they are identified - may access the kinematical region between the fixed target experiments and the presently available HERA data, since ISR events have a lower center of mass energy [40], [41]. Finally a method to avoid large corrections was developed at H1 making use of the redundant measurement at HERA [30], [42] by extracting the kinematical variables using three instead of only two observables.

Chapter 4

HERA and the H1 detector

4.1 HERA machine

HERA is the first electron proton collider and came into operation in autumn 1991, after eight years of construction and commissioning. The first collisions were recorded by the two HERA experiments H1 and ZEUS in spring 1992.

Two independent rings, situated in a 6.3 km long tunnel, are used for acceleration and storage of the electrons and protons. Figure 4.1 gives an overview of the HERA storage ring with its injection chains and the location of the experiments. The electron machine is a conventional storage ring, accelerating the electrons to 26.6 GeV, whereas the proton ring makes use of superconducting magnets to produce the high magnetic field needed to keep the 820 GeV protons on their orbit. The electrons and protons are pre-accelerated in the former e^+e^- storage ring PETRA to an injection energy of 12 GeV and 40 GeV, respectively. The proton beam proved to be very stable with an average lifetime of more than 24 hours, whereas the electron fillings had a lifetime of only some hours.

The particles are packed into a maximum of 210 bunches, with a bunch crossing distance of only 96 ns, and brought to head-on collisions in the two experimental halls. Presently two more experiment are being prepared [43], [44]. In the 1993 running period the machine operated with 94 electron and 90 proton bunches, 84 of them were colliding. The bunches with no colliding partner were used for an estimate of beam induced background. Some parameters of the HERA machine are listed in Table 4.1 comparing the design values with what was achieved in the 1992 and 1993 running periods. In 1993 HERA delivered an integrated luminosity of almost 1 pb^{-1} of which about 60% was recorded by H1 and could be used in the physics analysis. The main losses occurred by the selection of good quality runs and dead time introduced by the readout. Some run periods were lost because of malfunctioning of important detector parts or periods of very bad beam quality (typically at the start of a new luminosity run) which didn't allow to switch on sensitive detector parts. The limited statistics available with the data collected in 1992 already allowed a first look

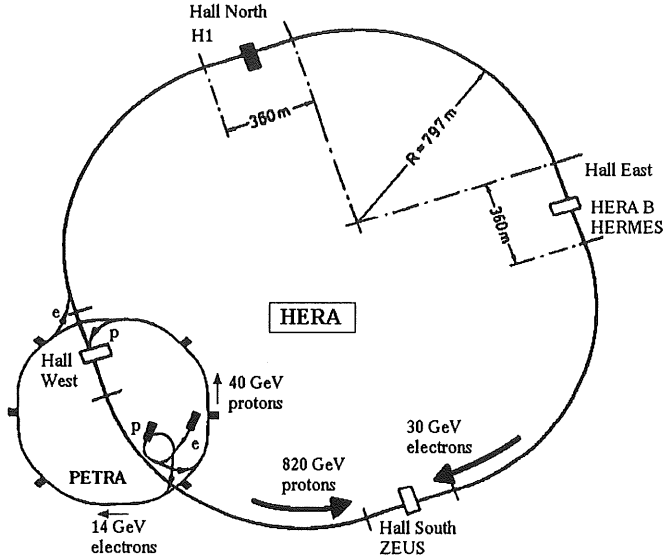


Figure 4.1: The HERA storage ring.

at the physics expected to be seen at HERA. Besides the first measurement of the proton structure function [35], which lead to the determination of the scaling violation of the proton structure function [47] with an estimation of the gluon density, much effort was taken to investigate the final state of the hadrons. The measurement of the energy and the transverse momentum flow [48] as well as the jet rates [49] in deep inelastic scattering events yields information on the QCD sub-processes. Furthermore this first years data allowed to measure the total cross section of photoproduction events [50], which take place via the exchange of a quasi real photon and therefore have a high rate. Also for this class of events the analysis of inclusive jet spectra allows to draw conclusions on the underlying QCD picture.

4.2 The H1 detector

This chapter shortly describes the H1 detector, more details can be found in [51]. The detector components used in this analysis and their properties especially in the 1993 running period are then discussed in the next sections. The main features are best illustrated by a typical deep inelastic scattering event recorded in the 1993 data taking period (Figure 4.2).

	unit	design [45]	1992 [46]	1993
Energy p/e	GeV	820/30	820/26.6	820/26.6
number of bunches p/e		210/210	10/10	90/94
current p/e	mA	163/58	2.5/2	16/14
bunch separation	ns	96	96	96
bunch length in z	cm	11	20	10
luminosity	$\text{cm}^{-2}\text{s}^{-1}$	$1.5 \cdot 10^{31}$	$3.0 \cdot 10^{29}$	$1 \cdot 10^{30}$
integrated luminosity	nb^{-1}	10^5	62	880
used for analysis	nb^{-1}		32	520

Table 4.1: HERA parameters.

The proton with an energy of 820 GeV is coming from the right and the electron (26.6 GeV) from the left side with the interaction region in the center of the detector. The scattered electron is detected at a large angle with respect to the proton direction, further referred to as backward region, whereas in this event the hadrons are detected in the central region. In the very forward region some activity is recorded due to the proton remnant. The two pictures on the right hand side give a radial view, in the direction of the proton, of the detector. The electron is measured in the backward calorimeter (lower picture) and balances the transverse momentum of the hadrons, as detected in the central region (upper picture). Since the large difference in the beam energies boosts the center of mass system along the z axis into the direction of the proton the detector is constructed asymmetrically and is instrumented in the direction of the outgoing proton with a higher granularity. Following the H1 convention this direction is referred to as positive z axis.

Figure 4.3 gives a schematical side view of the H1 detector with following detector parts starting from the interaction region:

- **Central Tracker:** a sandwich of cylindrical drift and multiwire proportional chambers, surrounding the interaction region. It is used simultaneously for track reconstruction of charged particles in the range $15 \leq \vartheta \leq 170^\circ$, particle identification, and triggering.
- **Forward Tracker:** completes the tracking system in the forward direction and measures particles with a polar angle $7 \leq \vartheta \leq 15^\circ$. It has three identical supermodules consisting of planar drift and proportional chambers.
- **Liquid Argon Calorimeter (LAR):** surrounding the tracking region in the forward and barrel region. It is divided into an electromagnetic part with lead absorbers, measuring the electron energy with a resolution of the order of $12\%/\sqrt{E}$ and a hadronic part with steel absorbers (resolution $50\%/\sqrt{E}$). The absolute energy scale for the electromag-

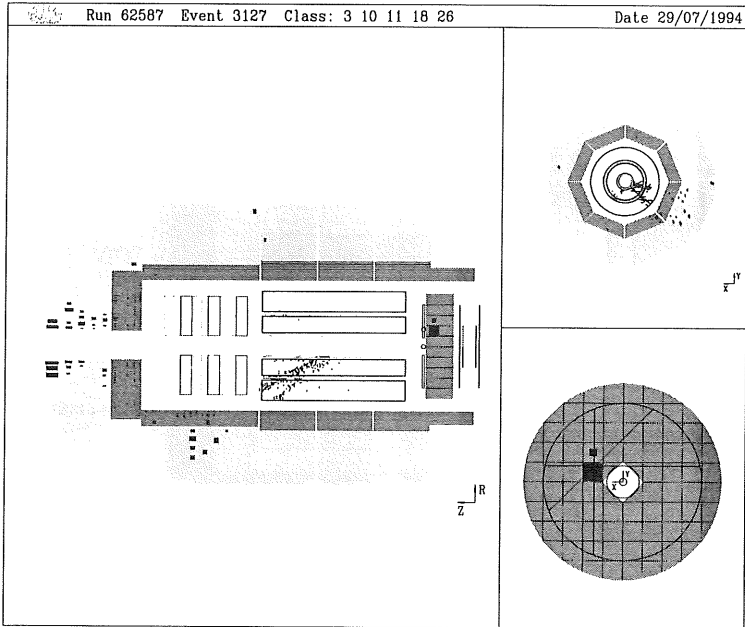


Figure 4.2: A typical deep inelastic scattering event with a scattering angle of 167° and an energy of the scattered electron of 26.6 GeV. The event kinematics as determined with the mixed method, yields $Q^2 = 35 \text{ GeV}^2$ and $x=0.01$. The two pictures on the right side give a radial view of the central (upper) and backward (lower figure) part of the detector in the direction of the outgoing proton.

netic part is known within 3% and 5% in the most backward part. The hadronic energy scale as determined from studies of the balance of transverse momentum of DIS events, is presently known to 7%. In the very forward region the calorimetric measurement is completed by a Si-Cu plug. It measures energy depositions between the beam pipe and the LAR ($0.6 \leq \vartheta \leq 3^\circ$).

- Backward electromagnetic calorimeter (BEMC): supplements the energy measurement in the backward direction ($151 \leq \vartheta \leq 177$). It provides a good electron detection but only a poor hadron measurement. It is completed by a multiwire proportional chamber (BPC) just in front of it, giving an accurate space point.
- Time of Flight System (TOF): two scintillator walls are installed behind the BEMC at 2 m upstream of the interaction region. Their accurate time resolution of the order of 2 ns

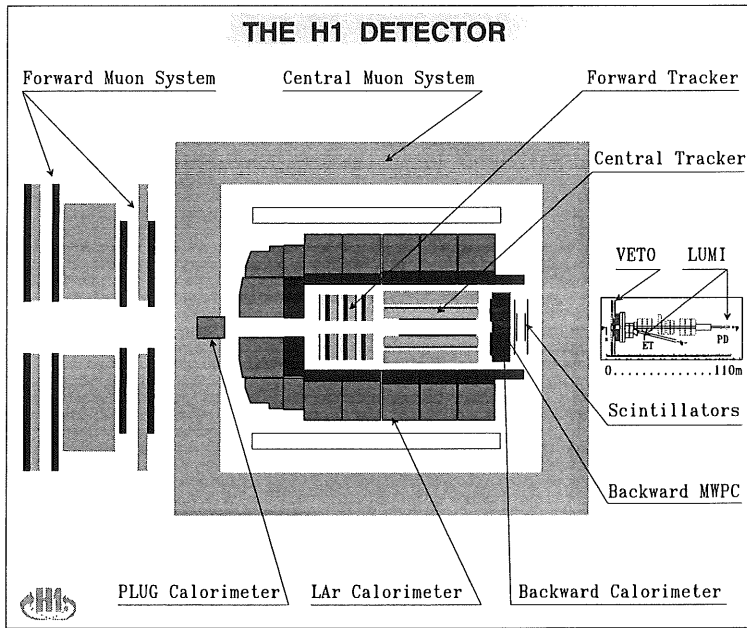


Figure 4.3: Schematical side view of the H1 detector.

allows to reject p-beam induced background originating from outside (upstream) the H1 detector. Furthermore they allow an estimate of the energy leakage of the BEMC.

- **Magnet:** the superconducting solenoid of 6 m diameter surrounds the H1 calorimeter, providing a homogeneous field of 1.2 T parallel to the beam axis in the tracking region of the H1 detector. It allows to determine the momenta of charged particles from the track curvature measured in the central tracker.
- **Muon detection:** muons escaping the H1 detector are recorded in the instrumented iron, an octagonal iron yoke surrounding the coil. Some 140000 channels are read out, allowing also a measurement of the hadronic energy leakage, which is generally small except in the BEMC region. It is completed by a forward muon system.
- **Luminosity system:** this system consists out of two crystal calorimeters for the measurement of collinear photons and small angle electrons. The γ detector is installed at $z=-103$ m and the electron detector (e -tagger) at -33 m. The luminosity system provides

at the same time a measurement of electrons scattered at very small angles (≤ 5 mrad), detection of photons from initial state Bremsstrahlung, and an accurate measurement of the luminosity. The latter records the Bethe Heitler process $ep \rightarrow ep\gamma$, which is proportional to the luminosity and has a well known cross section.

4.2.1 Central Tracker

A schematical view of the tracking area including the backward proportional chamber (BPC) is shown in Figure 4.4. The most central chamber system is a double layer of multiwire proportional chambers (CIP), giving a fast but coarse φ and z position of a track. It is followed by a z -drift chamber (CIZ) with a spacial resolution of $250 \mu\text{m}$ (design value) and two large volume jet chambers (CJC), measuring the $R - \varphi$ projection of a track within $210 \mu\text{m}$. The inner chamber is divided into 30 φ segments with 24 sense wire planes, the outer into 60 segments with 32 layers. The cells are tilted by 30° in order to allow optimal track reconstruction in the presence of the magnetic field. The two jet chambers are separated by another z -drift chamber (COZ) and again two layers of proportional chambers (COP). It

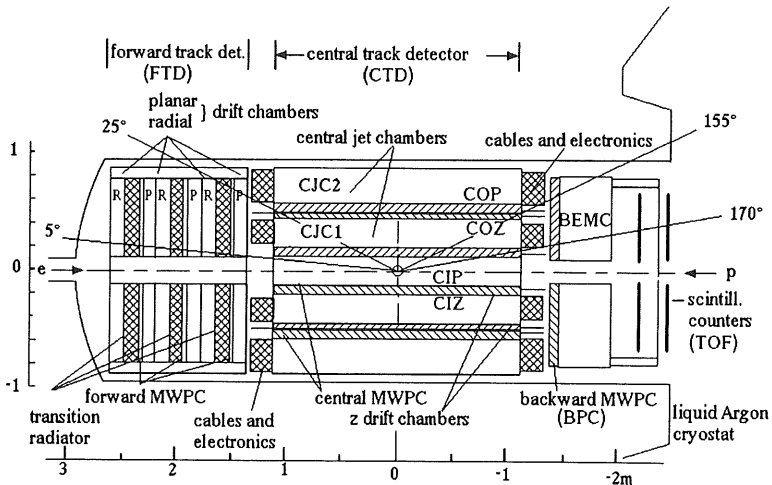


Figure 4.4: Schematical side view of the tracking area of H1.

becomes clear from Figure 4.4 that the well determined track quantities cannot be used for the identification of an electron scattered at large angles and measured in the BEMC, since it leaves the acceptance region of the inner jet chamber. However the tracks reconstructed in the central tracker were used for the reconstruction of the kinematical variables using the hadronic information (see Chapter 3.3).

Central Inner Proportional Chambers, CIP

The innermost chamber system of the H1 experiment consists of two thin multiwire proportional chambers (MWPCs). Their main purpose was delivering space points for three different triggers. This information together with the space points of similar chambers at larger radii [53], [52], four planes of MWPC's in the forward direction [54], or space points in the z drift chambers [55], is used to give a fast estimation of the z position of the event vertex. Therefore the design criterion was good time resolution to separate individual HERA bunch crossings. The space resolution was subject to the requirements of the z -vertex trigger [53].

	unit	chamber	
		inner	outer
active length	mm	2190	2190
chamber starts	mm	-1125	-1125
chamber ends	mm	1100	1100
radius of anode planes	mm	157	166
number of wires		480	480
wire distance	mm	2.06	2.17
gap width	mm	3.0	3.0
number of cathode pads		480	480
width of pad (along z)	mm	36.5	36.5
length of pad (along φ)	mm	123	130
middle of first pad in z	mm	-1107	-1107
middle of first pad in φ	°	22.5	0

Table 4.2: CIP geometry, absolute positions are given in H1 coordinates.

Chamber geometry and construction The chamber is described in detail in [56], we therefore only discuss the important points. The Central Inner Proportional Chambers (CIP) consist of two thin cylindrical chambers and have an active length L of 2190 mm with the $e-p$ interaction region in the middle, thus covering a large ϑ region from 8 to 172°. To minimize

the radiation thickness the chambers were constructed with a sandwich of Rohacell-foam and thin foils. The cathode is made of a graphite coated Kapton foil. Induced signals on the cathode couple through the Kapton to its other side, where an aluminium layer is segmented into pads of the size $\Delta z = 36 \text{ mm}$ and $\Delta\varphi = 45^\circ$, giving a length of 123 mm for the inner and 130 mm for the outer chamber, resulting in 480 pads per chamber with a 60-fold segmentation in z and 8-fold in φ . The inner chamber is rotated in φ by 22.5° with respect to the outer one which results in an effective 16-fold φ -segmentation of the two chambers. The signals from the pads are amplified directly on the chambers and finally shaped in the readout electronics which discriminates the signals with an adjustable threshold. The 480 anode wires are connected to positive high voltage. 30 wires are connected to the same high voltage supply, thus allowing a 16-fold high voltage segmentation. Some of the important properties of the chambers are summarized in Table 4.2 the geometry is illustrated in Figure 4.5.

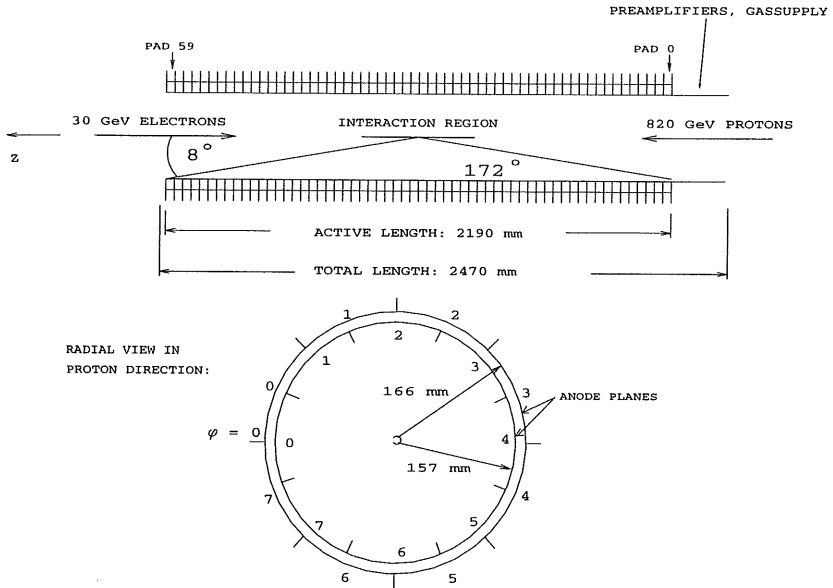


Figure 4.5: CIP geometry. The upper figure gives a schematical side view of the two chambers, whereas the lower picture gives a radial view in the direction of the outgoing proton.

Operation and performance The chamber is operated with an argon-ethan (50:50) mixture with an additive of 0.2 % of freon12 and 0.2 % of water. Test beam measurements and

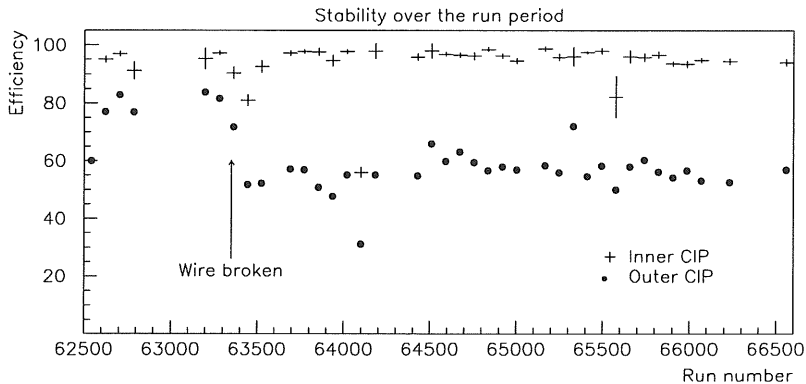


Figure 4.6: Run dependent efficiency for both chambers of CIP.

measurements with cosmic rays showed a plateau starting at 2400 V (2450) for the outer (inner) chamber. The worse noise situation in the H1 detector required slightly higher thresholds. Therefore both chambers had to be operated at an increased high voltage.

Problems and stability: already before the start of the data taking period, we had a high voltage problem in sector 0 of the outer CIP. Therefore the whole sector was at lower voltage and not efficient. Later at the beginning of the luminosity period a wire broke in a different region of the outer CIP which resulted in more dead sectors: sector 2 was completely dead, 1 and 3 only 50 % efficient. As a consequence of the 16 fold high voltage segmentation, sectors 1 and 3 were completely dead in that half of the pad neighbouring sector 2 and fully efficient on the remaining part of the pad.

However the other sectors behaved very stable over the whole 1993 running period, as shown in Figure 4.6 with a measurement of the run dependent efficiency. The method of the measurement is discussed below.

The time resolution was measured both with a source for a single pad and with cosmic rays for all pads in the detector, thus including effects of the whole readout chain as well. We measured a base width of 75 ns and FWHM of 21 ns [56]. Thus the timing is good enough to separate different HERA bunch crossings. Since the discriminated signal is available for 10 consecutive bunch crossings offline, it is possible to study the effect of mis-timing also in real $e - p$ data.

The efficiency for the two chambers was studied with CJC tracks pointing to the chambers,

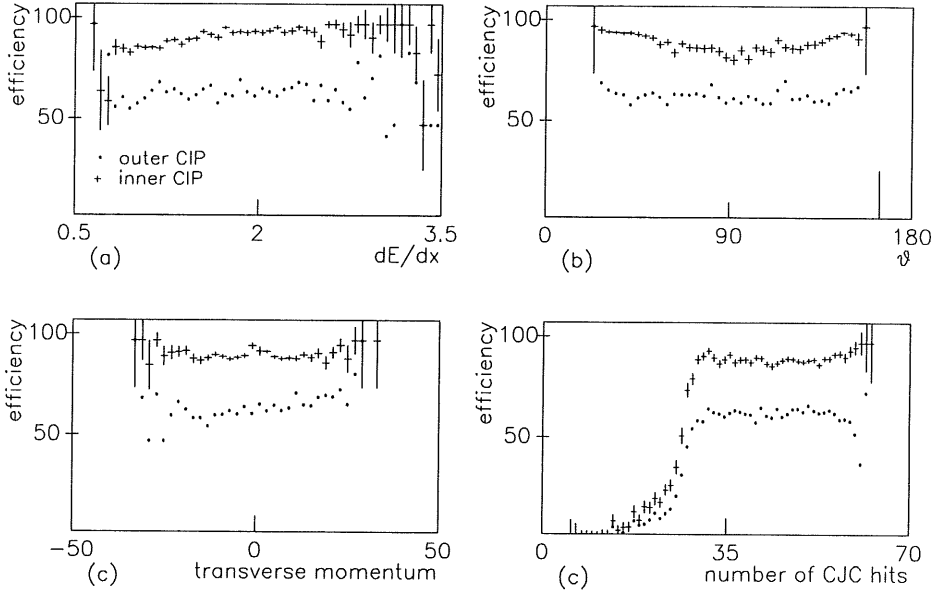


Figure 4.7: CIP efficiency as a function of track parameters: (a) energy loss of the particle, (b) ϑ of the track, (c) transverse momentum p_t and (d) number of CJC hits used for the track.

using an event sample which was not only triggered by a trigger using the CIP information. Only events with less than 20 tracks were accepted in order not to suffer from random coincidences. Some further track criteria were applied:

- tracks had to come from the interaction region ($-30 \leq z_{vertex} \leq 20$ cm) with the distance of closest approach of the track to the beam axis (DCA) less than 1 cm. This cut rejects beam induced background and badly measured tracks.
- track length: at least 35 hits were required for a good track, guaranteeing a good track quality with the particle measured in both jet chambers.

The CIP was found to be efficient if a hit was found within a distance of $\Delta\varphi \leq 22.5^\circ$, corresponding to half the padsize, and $\Delta z \leq 7$ cm to the track. The large window in z (twice the padsize) was necessary, since no z chamber information was required. The z resolution of the tracks is therefore determined by the CJC, which uses charge division methods to determine z .

Figure 4.7 shows the efficiency as a function of different track parameters; it is not corrected for the known dead sectors (32%) of the outer chamber:

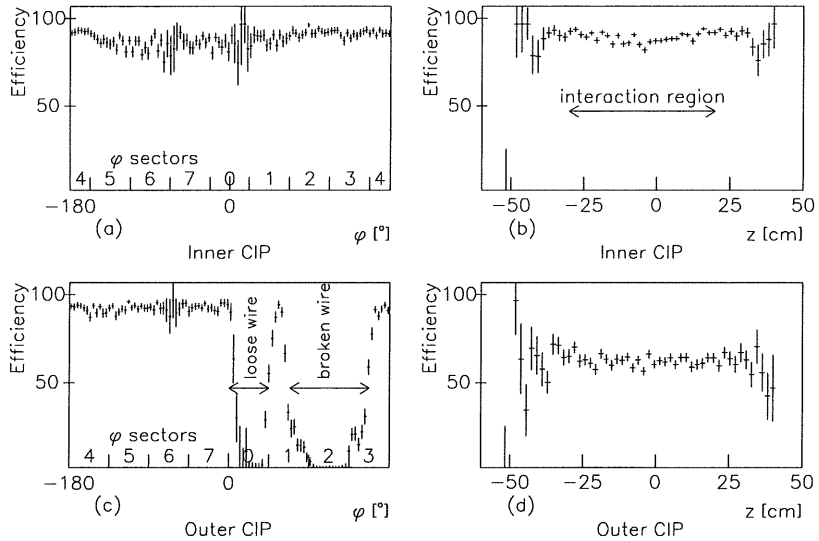


Figure 4.8: CIP efficiency: (a) and (b) inner chamber, efficiency as a function of φ and z , (c) and (d) for the outer CIP.

- 4.7(a) Specific ionization (dE/dx) of the particle measured with the CJC. The inner chamber clearly suffers from a loss in efficiency towards low dE/dx , i.e. minimum ionizing particles, indicating that the chamber is not operated on the plateau. This effect is reduced and hardly visible anymore for the outer chamber, which requires 50 V less voltage for the same gas gain due to the larger wire spacing [57].
- 4.7(b) ϑ of the track: another consequence of the fact that the inner chamber is not on full high voltage is visible. The efficiency for the inner CIP is ϑ dependent and is smallest for tracks crossing the chamber perpendicular, where the ionization length is shortest. Again the efficiency for the outer chamber does not vary over ϑ .
- 4.7(c) transverse momenta p_t of the track: no dependence is seen which essentially shows that the quality of the track reconstruction is good.
- 4.7(d) number of CJC hits: the drop in efficiency for tracks with less than 30 hits is attributed to bad track quality. The short track length does not allow to determine the track

parameters accurately enough. Therefore a cut on the number of CJC hits larger than 35 was applied for the analysis of the CIP efficiency.

	inner CIP %	outer CIP %
average chamber efficiency (no dead sectors)	91.4 ± 0.3	95.6 ± 0.3
dead sectors	0	37.5
sector 0	88.4 ± 1.4	4.6 ± 4.4
sector 1	91.3 ± 1.0	$49.2 \pm 2.0 (94.4 \pm 1)^*$
sector 2	95.1 ± 0.6	0
sector 3	94.0 ± 0.6	$49.6 \pm 1.5 (95.6 \pm 0.7)^*$
sector 4	95.9 ± 0.5	95.2 ± 0.5
sector 5	89.4 ± 0.8	95.4 ± 0.5
sector 6	86.8 ± 1.0	95.6 ± 0.9
sector 7	89.6 ± 1.0	96.1 ± 0.6

*: part of the sector which is not degraded

Table 4.3: Efficiency for CIP in percentage.

The final efficiencies as a function of φ and the z position on the chamber are illustrated in Figure 4.8, clearly showing the dead zones of the outer CIP (4.8(c)) No fluctuations along z are seen in the region accessible with this method, corresponding essentially to the interaction region. This was confirmed by a measurement with cosmic rays, which accesses the whole z range of the chamber. The inner chamber shows some φ dependency being due to its sensitivity to geometrical variations (gapsize). The average efficiency for both chambers, excluding the dead sectors, as well as the efficiency per sector is summarized in Table 4.3.

Backward Proportional Chambers, BPC

The Backward Proportional Chambers (BPC) give a space point in the angular region of ϑ from 174.5° to 155.5° . This is used for an accurate ϑ determination, since in this angular region the central detector is not very useful (CIZ measures only angles of maximum 172°). Furthermore it is used to calculate the correct impact point of a particle on the BEMC. This is important since the corrections to the measured energy such as correction for the dead material in front of the BPC and corrections for particles depositing part of their energy between the stacks (crack corrections) are position dependent. To get a good space resolution the anode wires are read out.

Geometry The BPC is a system of four MWPC's and consists of four anode planes with 624 wires each and five graphite coated cathode planes with no segmentation. The middle of

	unit	plane			
		0	1	2	3
active length	mm	515			
starts at r	mm	135			
ends at r	mm	650			
number of wires	mm	624			
wire distance	mm	2.5			
gap width	mm	4			
z position of anode planes	mm	-142.3	-141.5	-140.7	-139.9
φ orientation of plane		0	90	45	-45
efficiency of plane	%	84.1	86.0	85.0	80.1

Table 4.4: BPC parameters.

the chamber is situated at $z=-141.4$, just in front of the BEMC. Each chamber has an active gap of 4 mm and a wire spacing of 2.5 mm, only every second wire is read out. The wire orientation is different in each plane: with increasing z we have a plane with wires strain horizontally (x -plane), vertically (y -plane), in $+45^\circ$ (u -plane) and -45° (v -plane) direction. Thus a combination of the four planes gives an accurate space point. The active zone of the BPC starts at an inner radius of 135 mm and ends at a radius of 640 mm and does not cover the full BEMC surface. The geometrical layout of this chamber system is illustrated in Figure 4.9.

Some of the geometrical properties of the chamber are summarised in Table 4.4.

Reconstruction of a BPC space point A space point is reconstructed from the information in the four wire planes. First, bands of consecutive active wires are found for each plane. Up to ten wires may contribute to one wire band with one wire allowed to be missing. Then the crossings of orthogonal planes are found - (x, y) or (u, v) - and tried to match. If no matching between four planes is found a combination with three out of four planes is tried. This gives some additional spurious hits but was found to be necessary to cope with the deficiencies of the single planes. The error in the reconstructed point depends on the width of the wire bands and thus on the amount of preshowering in the dead material in front of the chamber.

BPC operation and performance The BPC suffered from high voltage stability problems in the 1993 running period. One reason is that some of the wires are very close (135 mm) to

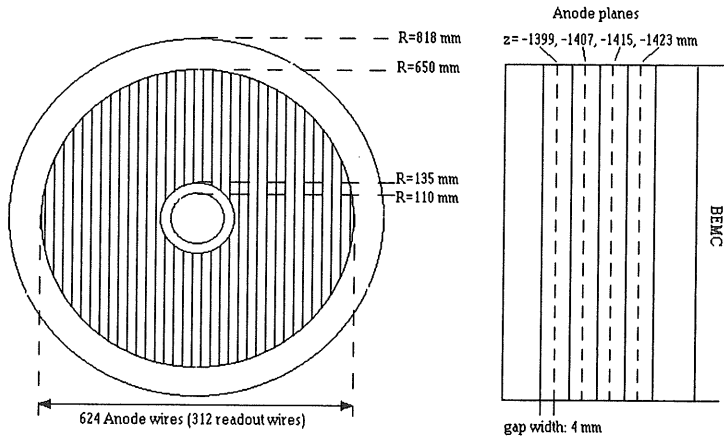


Figure 4.9: BPC geometry.

the beam pipe and therefore have to stand a high particle flux. Another reason was found after the running period: the inner ring which fixes the position of some wires was misplaced. Due to these problems the high voltage had to be lowered in some regions which lead to position dependent inefficiencies. Fortunately these inefficiencies smear out in the reconstruction of a BPC hit so that we get a rather homogeneous hit efficiency.

We measured the single plane efficiency by requiring a crossing of three planes and asking for the fourth plane. In this analysis we restricted ourselves to events with only few hits in order not to suffer from random coincidences between two planes and the runs which were used for this analysis.

Figure 4.10 shows the resulting inefficiency for each plane, with large boxes corresponding to large inefficiencies. Obviously the efficiency loss is more pronounced for large radii, an effect enhanced for the two planes with generally lower efficiency (plane 0 and 3). Figure 4.11 illustrates the position in terms of the radius and φ for all four individual planes and the efficiency for a three-fold coincidence. The latter was extracted from the single plane efficiencies with the assumption of the inefficiencies between two planes being independent. With ϵ_i denoting the individual chamber efficiencies and ϵ_i the efficiency for a three-fold coincidence with the i^{th} plane missing, for example

$$\epsilon_2 = \epsilon_0 * \epsilon_1 * \epsilon_3 * (1 - \epsilon_2),$$

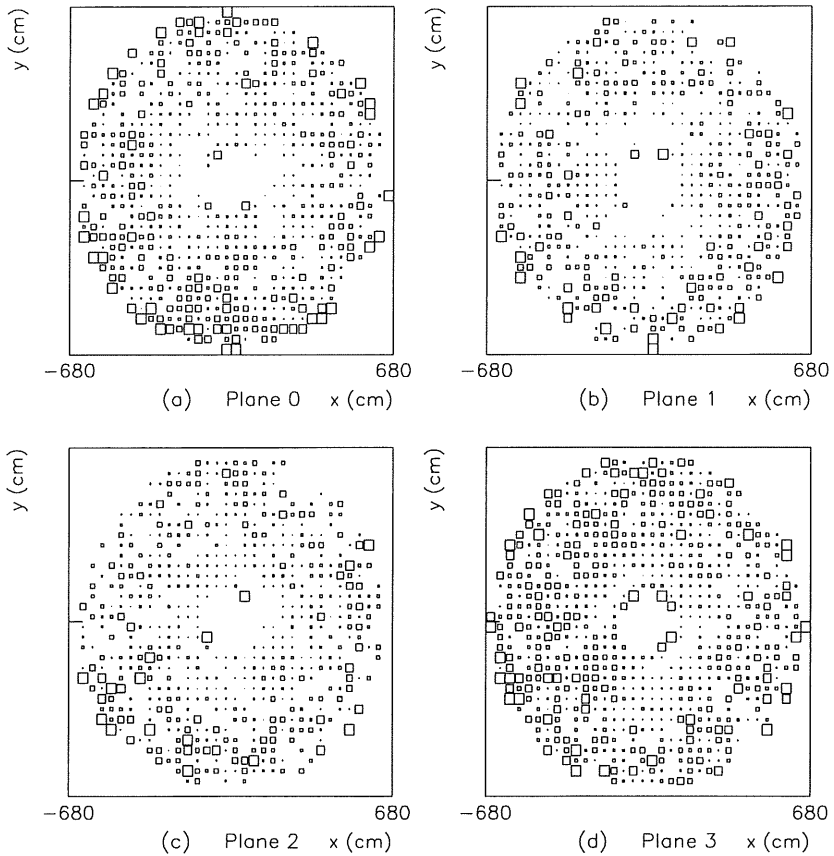


Figure 4.10: Inefficiency of the four BPC planes, only inefficiencies bigger than 15 % are shown. A clear difference in efficiency between planes and different radii is seen (see text).

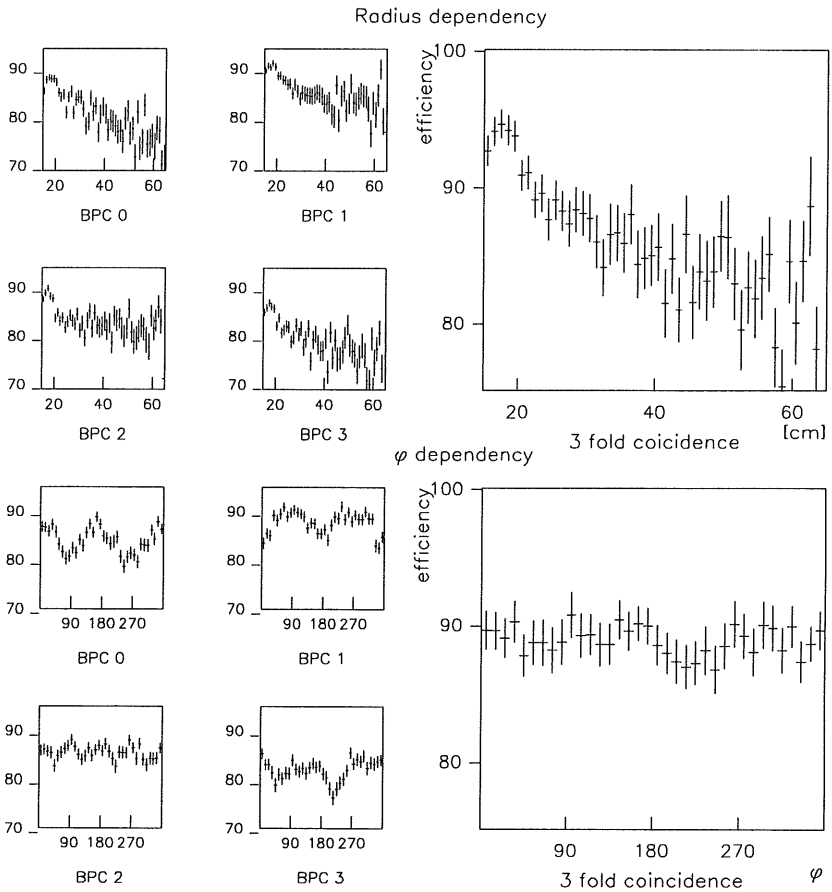


Figure 4.11: Radius and φ dependence of the individual plane efficiency and the efficiency for a 3-fold coincidence.

the efficiency for a coincidence of any three of the four BPC planes gets:

$$\epsilon_{3of4} = \epsilon_0 + \epsilon_1 + \epsilon_2 + \epsilon_3 + \epsilon_0 * \epsilon_1 * \epsilon_2 * \epsilon_3$$

The efficiency as a function of the angle φ varies with the wire orientation; losses in efficiency show up for the short wires which run from the inner ring to the outer ring. This effect

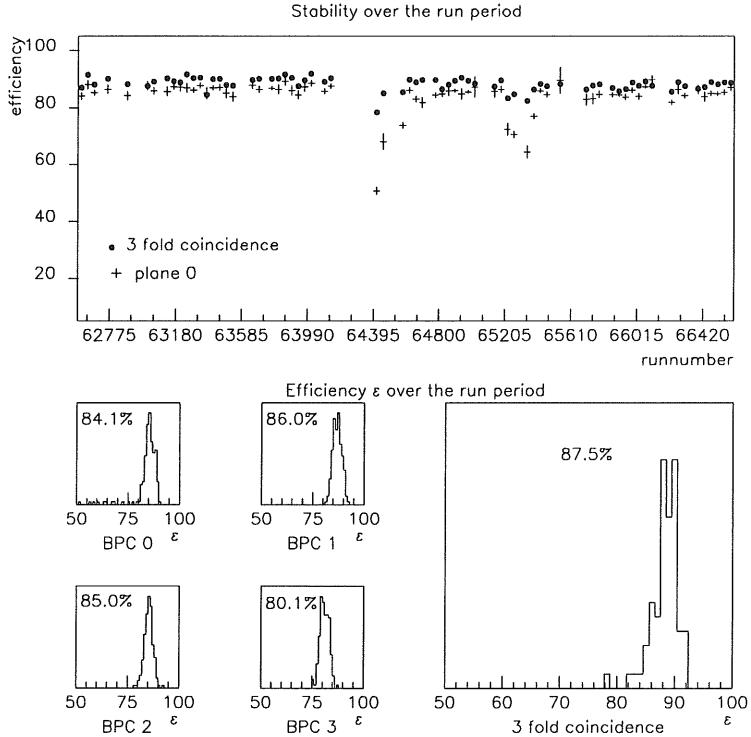


Figure 4.12: Run dependency of the BPC efficiency for the runs which were used in this analysis.

is correlated with the slight misplacement of the inner ring. The efficiency for the 3-fold coincidence shows no variations in φ . On contrary the radius dependency does not completely smear out in the coincidence, but it is reduced to 3-4%, this has to be compared to an efficiency loss towards large radii of 7-15% for the individual planes. The run dependent efficiency is shown in Figure 4.12 for plane 0, one clearly sees the fluctuation during the whole run period. However, the efficiency for a three fold coincidence is rather stable. The analysis

of the proton structure function described in the next chapters extensively uses the BPC information for electron identification. Obviously the intrinsic plane efficiency discussed above cannot be used without further studies, since effects as preshowering in the dead material are not included. A further discussion of the BPC hit efficiency will follow in section 6.2.3.

Central inner z -chamber, CIZ

CIZ surrounds the CIP and is primarily intended to measure the z position of a track with good accuracy (design value $250 \mu\text{m}$), its construction and performance is described at full detail in reference [58].

A z determination requires a drift direction parallel to the beam axis implying wires to be strung perpendicular to the beam. Technically this was solved by choosing the geometry of a 16 fold polygon, giving a 16-fold division of the drift cells in φ . The chamber is divided along z in 15 drift cells, each having a volume of $\Delta z=12 \text{ cm} \times \Delta r=2 \text{ cm}$ with four sense wires per cell. The wire plane is not nominal to the beam axis but tilted by 45° (-45° in backward direction) to improve the track resolution in forward and backward direction and resolving the left right ambiguity. Some geometrical properties are summarized in Table 4.5.

	unit	
active length	mm	1800
chamber starts at z	mm	-1080
chamber ends at z	mm	720
number of drift cells in z / φ		15 / 16
number of sense wires per ring		4
number of potential wires per ring		3
total dead zone in z / φ	%	1.6 / 6.1

Table 4.5: CIZ parameters.

Performance and operation in 1993 Since the CIZ is very close to the beam region with the disadvantage of having only few wires, and therefore a big drift volume per wire, it is very sensitive to the high particle flux induced from ep collisions and background events. Already in 1992 the high voltage became unstable in the very backward ring, requiring a reduced high voltage which resulted in an inefficient ring. With the higher beam currents in 1993 four more rings developed a similar behaviour. After the running period the chamber was opened and the stability problems were found to be due to ageing of the wires [58]. The efficiency for finding a CIZ segment, built out of two or three hits, linked to a CJC track

is plotted as a function of the z position and φ on the chamber in Figure 4.13. (a) shows the dead region in φ around $\varphi=0$ due to the cable channel whereas (b) shows the effect of the dead rings, they are marked with arrows. The efficiency in the good regions reaches as much as 80%, with a drop at z very backwards. This drop might be attributed to bad CJC track quality, since generally the tracks are very short at the end of the chamber. The resolutions

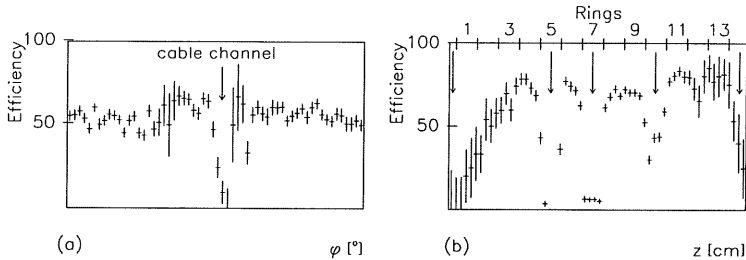


Figure 4.13: Efficiency for finding a CIZ segment linked to a CJC track as a function of φ (a) and z (b). Clearly visible are the dead rings along z and the readout channel in φ , marked with arrows.

obtained in the 1993 running period were measured using tracks reconstructed in the central detector. An average deviation from a straight line fit of $\sigma_z=300\mu\text{m}$ for CIZ internal tracks and $600\mu\text{m}$ for linked tracks was found. The φ -resolution was determined to be of the order of 8° but strongly depends on the charge deposited on the wires.

4.2.2 Backward electromagnetic calorimeter, BEMC

The main task of the backward electromagnetic calorimeter (BEMC) is to give an accurate energy measurement for the scattered electron. It is however not optimized for a good hadronic measurement as will be shown later. For a measurement of the hadronic energy in the backward region a combination with other detector components has to be used.

Geometry The BEMC covers an angular region of $151^\circ \leq \vartheta \leq 177^\circ$ with full acceptance in φ . It is segmented into 88 calorimeter stacks of the size of $16 \times 16 \text{ cm}^2$, each consisting of a lead-scintillator sandwich with 50 active layers. The complete structure has a thickness of 22.5 radiation length or 0.97 nuclear absorption length. This means a shower coming from an electron should be well contained inside the BEMC whereas a hadronic shower has a considerable leakage.

Each stack is read out by four wavelength shifters (WLS), covering the full length of a stack. They are connected to photodiodes, allowing a determination of the x and y position of the shower center of gravity (c.o.g.) to 1.5 cm. In addition two WLS are installed covering only the last 15 layers of the stack, giving a possibility to identify hadrons, since electrons deposit

the main fraction of their energy in the front part. A cluster algorithm is used to combine a maximum of nine cells to a cluster with the most energetic stack in the middle. Only in case of adjacent clusters with overlapping stacks less than nine stacks are used.

Calibration A possible miscalibration of the BEMC directly affects the resolution in Q^2 and x . The calibration involves two independent chains: calibration of the electronic gain and of the light response.

- **electronic stability:** The response of the total electronic chain was measured and recalibrated with pulser runs once a week during the data taking period. This resulted in a stability at a few per thousand, far better than the uncertainties of the light calibration.
- **Light response:** The response of the WLS has to be monitored and calibrated permanently, since the BEMC suffers from scintillator aging and radiation damage. The WLS for each stack were initially calibrated with a 5 GeV electron test beam at DESY with rather large uncertainty. A much better calibration can be reached with $e - p$ data using the energy spectrum of the scattered electron [59] or by making use of the hadronic measurement in the LAR calorimeter, since the energy of the electron is given by a measurement of the electron angle and the angle of the struck quark (see Chapter 3.4).

The resolution can be written as

$$\frac{\sigma}{E} = \frac{\sigma_{noise}}{E} \oplus \frac{\sigma_{sampling}}{\sqrt{E}} \oplus \sigma_{const} \oplus \sigma_{calibration}$$

The noise term was determined to 97 MeV and the constant term is less than 1%. The sampling term which determines the energy dependence of the energy resolution is 10%, and the uncertainty in the absolute energy scale of the BEMC was determined to 1.7% for the 1993 running period [60].

Energy corrections Several corrections have to be applied to the reconstructed energy. First one has to correct for the dead material between the interaction region and the BEMC, which is done using detailed Monte Carlo simulations of the tracker. The material can locally reach up to one radiation length. Only an average correction is made; at 10 GeV dead material of a thickness of one radiation length leads to an error of the energy of 1% [32].

Another significant energy loss occurs if a shower develops in two stacks, i.e. deposits part of the energy between two stacks (crack corrections). This effect was studied in a detailed MC simulation [61]. It was found that the corrections crucially depend on the knowledge of the correct impact point on the BEMC which is given by the hit in the backward multiwire proportional chamber (BPC). The corrections can rise to up to 8%.

BEMC hadronic measurement The BEMC is suitable for a good measurement of the energy of the electrons. Their shower should be well contained within a stack, both in radius and in z . In contrast it is a thin medium for hadrons ($0.9 \lambda_h$). In this analysis we are not that much interested in a correct energy measurement for hadrons but in possibilities to distinguish them from electrons.

One handle is the measurement of the backward part of the energy with the short WLS. Unfortunately it turned out to be difficult to understand their response and this measurement could not be used so far.

The lateral size of the cluster turned out to be a better estimator. It should be larger for pions than for electrons as confirmed by test beam measurement. For more details on this estimator see chapter 6.2.4 and [59].

The hadronic response of the BEMC was measured with a π^- test beam of 30 GeV at CERN. Its analysis showed that about 40% of the pions pass the BEMC as minimum ionizing particles with an energy deposit of the order of the noise level. The remaining ones deposit only 30 to 40% of their energy in the BEMC.

4.2.3 Trigger and data acquisition

The detection of interesting physics events from genuine ep collisions is a challenge for the two experiments at HERA since the background is orders of magnitude higher than the expected rate of ep collisions. Background is mainly beam induced and includes:

- Proton-gas interaction: the protons may interact with remaining particles in the beam pipe. The vacuum around the interaction region is much worse than in the pure proton ring due to the synchrotron radiation of the electrons. Therefore beam gas interactions mainly take place close to the experiment.
- Electron-gas interactions: the cross section is much smaller than for proton gas interactions, but since the event kinematics points backwards, they may be a source for contamination of deep inelastic events.
- Proton beam pipe interactions: off momentum protons may hit the beam pipe preferably at the location of collimators. Electron beam pipe interactions are of minor importance due to the lower beam currents and the better focussed beam.
- Synchrotron radiation: the electron ring is bent just a few meters away from the interaction region in order to achieve collisions. This makes synchrotron radiation visible in the detector.

The H1 trigger components used in the first trigger decision level work dead time free. They mainly make use of the different topology of the background events to suppress them at an early stage:

- Estimate of the position of the z -vertex using the fast signals of multiwire proportional chambers. The z position has to be within ± 20 cm around the nominal interaction point [53].
- Extraction of the $R - \varphi$ vertex using CJC tracks [62].
- Reconstruction of the vertex in the time coordinate by a measurement of the time of flight with the TOF system. It allows to reject events from upstream (in proton direction) of the interaction point.
- Veto against beam halo events provided by two scintillator hodoscopes.

Identification of interesting physics events by a measurement of the energy flow in the calorimeter completes the trigger decision:

- Measurement of the total, transversal and missing energy in the LAR.
- Identification of electron candidates by isolated electromagnetic clusters in the LAR or the BEMC.
- Electrons recorded in the electron tagger.
- Detection of one or more muons in the muon chambers.

Given the short bunch crossing distance of only 96 ns it is obvious that an event selection has to be done in several steps in order to reduce dead time. In the 1993 running period only three out of the planned four trigger levels were operational. Each subsequent trigger level is only started if the event has been accepted by the previous trigger level. The first level triggers as well as all the data acquisition systems use a pipelined design, which allows to extend the decision time to 2.3 μ s without any dead time. Only after a positive first level decision the data taking is stopped and the readout is started. At the same time a software based level three trigger starts operation. The information available to it contains information on individual subsystems and the level 1 trigger decisions. Finally the event passes a filter system on a RISC processor farm, working asynchronously to the data taking. On this level already part of the reconstruction takes place allowing to use the full event information for the selection of the events to be written to a storage device. The final reconstruction and classification of the events is done offline in a later step.

Chapter 5

The Data

5.1 Event selection

The events finally used in this analysis run through different steps of event classification, allowing to check the efficiency and the effect of different cuts. A description of the 1993 event selection can be found in ref. [63].

We used the standard event selection of the H1 deep inelastic analysis group. All DIS

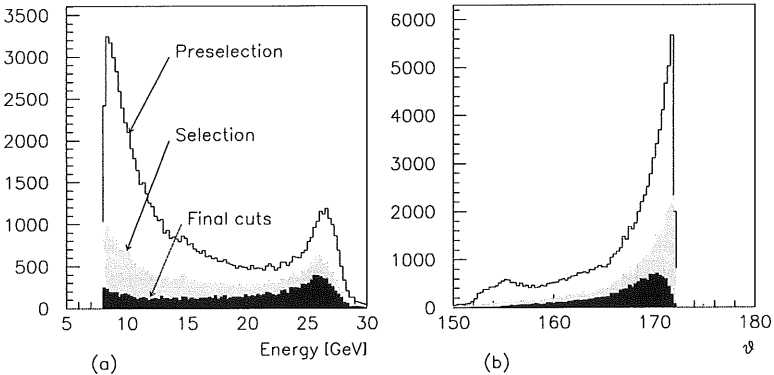


Figure 5.1: Effect of different selection steps on the energy (a) and angle (b) distribution. The preselection requires only the existence of a reconstructed vertex or a BPC point within 10 cm of the cluster c.o.g. whereas the selection requires both conditions to be fulfilled with the BPC cut at 5 cm. The final cuts require the vertex to be within 25 cm around the nominal z -vertex position and a cut against background (CIPCIZ) which will be discussed in the next chapter.

candidates had to fulfill following conditions:

- Trigger selection

- Energy cluster in the BEMC with an energy above a certain threshold [64]. Three different thresholds were set in 1993, allowing a cross check of the trigger efficiency. For this analysis a trigger threshold of 7.7 GeV (value of 50% efficiency) was used. Accessing the energy region below 7 GeV would require a combination with other triggers, because of the high background rate. The trigger efficiency was determined to rise from 75% between 8 and 9 GeV to 100% for energies above 10 GeV [65].
 - TOF veto: Requiring TOF response in the interaction window rejects beam induced background from outside the detector [51].
- Event selection
 - Energy of the largest cluster in the BEMC has to be larger than 7 GeV.
 - There exists a BPC point within 5 cm of the center of gravity of the cluster, after parallax correction in the xy -plane.
 - Existence of a vertex based on either CJC or forward tracks. This requirement guarantees a good ϑ measurement and rejects beam induced background.
 - A stronger TOF cut on the pad level ensuring that the event is not a background event from upstream with a secondary vertex inside the detector.
 - The cluster is not in the innermost BEMC part, where the stacks are not quadratic. To avoid this region which is difficult to calibrate it was required that the cell with most of the energy of the cluster was not one of the innermost stacks ($\text{abs}(x)$ or $\text{abs}(y) \geq 13$ cm).
 - Good run selection: only runs with the detector parts relevant for this analysis (LAR, BEMC, CJC and BPC) switched on are considered.

The effect of the cuts on the selected event sample is illustrated in Figure 5.1. The empty histogram is a preselected sample with very loose cuts, only requiring the existence of a vertex or a BPC hit within 10 cm of the cluster c.o.g.. There is considerable background in the sample as can be estimated from the huge amount of low energy events. The requirement of a vertex and a BPC hit within 5 cm of c.o.g. already significantly reduces the low energy part. The loss of events at high energies mainly comes from the vertex requirement. The final cuts restrict the vertex position to ± 25 cm around the nominal vertex position and a further background cut (CIPCIZ), which will be discussed in the next chapter, is applied. Again we observe a large reduction in the low energy part and at large scattering angles. The loose cuts of the event selection define the event sample which will be used in the following. It is still dominated by background especially in the low energy part, since only electron identification cuts have been applied so far. The efficiency of some cuts and further cuts against background will be discussed in the Chapter 6.

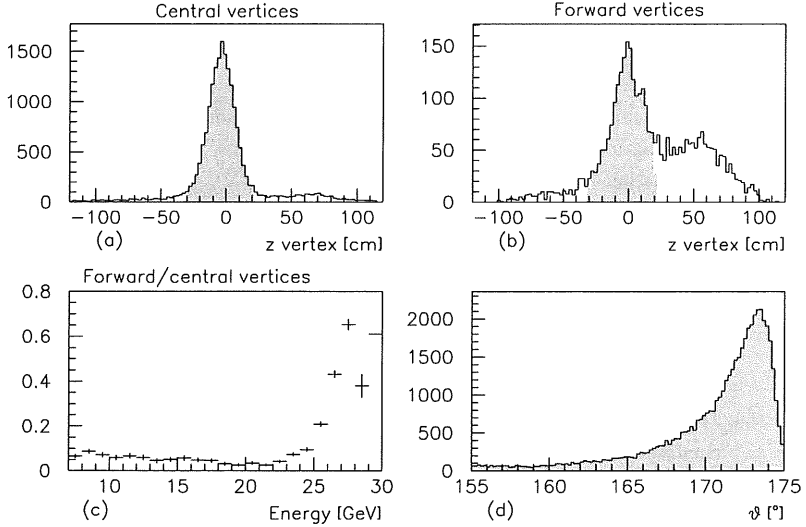


Figure 5.2: z -vertex distribution for the selected DIS events, for vertices determined by central tracks (a) and forward tracks (b), the hatched area indicates the events used for this analysis. The ratio of central to forward vertices is plotted in (c) as a function of the energy of the electron candidate. (d) gives the ϑ spectrum for the selected events.

5.2 Vertex Determination

The $e - p$ interaction vertex in the $x - y$ plane has a size of up to 2 mm. Since the mean position of the x, y vertex is very stable for one electron fill its value is determined by a fit of good tracks over all runs of one electron fill. A strong track criterion was used for the definition of good tracks: long, high momentum tracks with a small value at DCA. The z -vertex is then determined eventwise with all tracks fitting to the x, y vertex. At the moment the z -vertex is determined by either forward or central tracks, no combination is used yet. The reconstructed z position of the vertex (z_{vertex}) is shown for vertices reconstructed by central (Figure 5.2 (a)) and forward tracks (b). The distribution peaks at the nominal z -vertex position $z = -5$ cm with a width of ± 20 cm. But there is a second peak, more pronounced in the distribution for forward vertices, at 70 cm. This is due to satellite bunches developing around the proton bunches with a time difference of 4.8 ns. Figure 5.2 (c) gives the ratio of forward to central vertices as a function of the energy. The vertex is generally determined by tracks measured in the central trackers, except in the kinematical peak region, where the jet angle is lower than 30° .

5.3 ϑ measurement

5.3.1 ϑ determination

A good ϑ determination of the electron is imperative for a good resolution of the kinematical variable Q^2 in both the pure electron and in the mixed method. In H1 ϑ is defined as the polar angle with respect to the proton direction.

For ϑ angles lower than 155° the angle is measured with good accuracy by the central detector but this method fails in the very backward region we are interested in. The best resolution is reached by the point measured in the BPC and the vertex. A point in $r-z$ could be measured with much better accuracy by CIZ but the longer lever-arm in the BPC-vertex measurement diminishes its relative error. The measured ϑ distribution is shown in Figure 5.2 (d).

As expected from the shape of the lines of constant electron angle in the $Q^2 - x$ plane (see Figure 3.1 (b)) the distribution falls rapidly towards lower scattering angles due to the $1/Q^4$ term in the cross section. This means that the bulk of these low x events is located at very large angles around the beampipe.

5.3.2 ϑ resolution

The ϑ resolution in the backward region as measured with the BPC hit and the vertex position is dependent on the radial accuracy of the BPC hit, the vertex resolution and the amount of preshowering in front of the BPC. Since especially the last two points are not reproduced

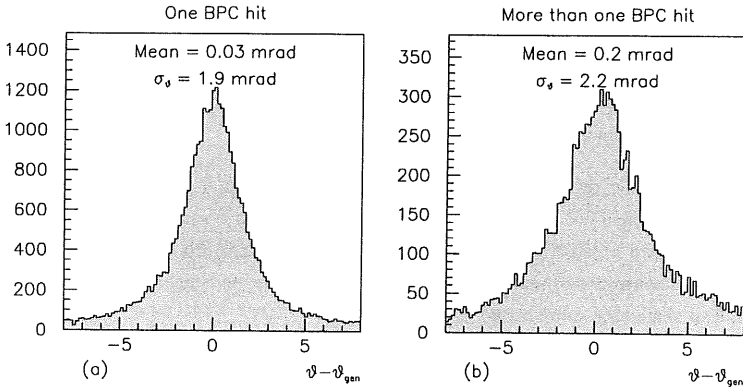


Figure 5.3: Theta resolution as determined from Monte Carlo simulations, by comparing the reconstructed and the generated angle ($\vartheta - \vartheta_{gen}$) for events with exactly one (a) BPC hit within 5 cm of the cluster c.o.g. and for events with preshowering (b).

	average BPC [mrad]	only one BPC hit[mrad]	CIP [mrad]	Cluster [mrad]
Data	2.5 ± 0.3	1.7 ± 0.7	4.8 ± 0.6	5.8 ± 0.3

Table 5.1: ϑ resolution in backward region.

exactly by simulation it is not possible to determine the angular resolution by simulations alone.

The simulated resolutions for events with one single BPC hit (within 5 cm of the cluster c.o.g.) and for events with more than one BPC hit (events with preshowering) are shown in Figure 5.3 (a) and (b), respectively. The mean value for the events with preshowering is shifted from 0.03 to 0.2 mrad since the angle is always determined by the closest BPC hit.

A cross check of this simulated resolution with the real one turned out to be somewhat difficult, because, except for very large angles close to the beampipe, the BPC-vertex measurement is the most accurate one. We tried to unfold the ϑ resolution from the distribution of different ϑ measurements. The method is explained in more detail in Appendix A. For a measurement of the angle in backward region we have four possibilities:

1. BPC-vertex: the resolution is rather constant over the range of ϑ , the variation is dependent on the ratio of the radial BPC to the z -vertex resolution.
2. Cluster-vertex: determined by the cluster resolution in the radius and the z position.
3. CIP-vertex: the resolution is strongly ϑ dependent, it is smaller than the BPC-vertex resolution for very large angles.
4. Vertex fitted tracks: these tracks are strongly dependent on the BPC resolution since most of them are linked to the BPC point. Therefore this angle gives no new information and was not used in the analysis.

The deviations of these three measurements of the angle give us a measurement of the individual ϑ resolutions plus a correction term proportional to the z -vertex resolution. The latter has to be applied because all three measurements use the same vertex. The z resolution of the vertex was determined by making use of the strong radius dependency of the $\vartheta_{CIP-vertex}$ resolution. The results are summarised in Table 5.1.

Chapter 6

The Background

6.1 Beam induced background

Beam induced background was the main background before the selection cuts. Interactions of electrons or protons with remaining gas atoms or elements of the beam pipe have generally a different topology from genuine ep interactions. Hence a large fraction can already be suppressed at the trigger level. In this analysis they are rejected by the requirement of the TOF, which essentially means that the event vertex has to lie inside the H1 detector. The further selection cuts, especially the tight vertex requirement reduces the remaining background to less than 1%. This number was deduced from studies with so called pilot bunch events. The latter are electron or proton bunches with no colliding partner (1993: 10 electron and 6 proton pilot bunches). They allow to study the effect of the cuts and to estimate an upper limit for beam induced background by multiplying the number of events surviving the cuts (N_{beam}) with the ratio of the beam currents and the current of the pilot bunches:

$$N_{beam}^{tot} = N_{beam} \cdot \frac{I_{e/p}^{tot}}{I_{pilot}^{e/p}} \quad (6.1.1)$$

This number was found to give only an upper limit because some of the empty bunches were partly filled.

In 1993 the fraction of the beam current was 0.138 ± 0.025 (0.074 ± 0.007) for the electron (proton) beam. We found that the contamination was generally below 1% and below 10% in the highest y bins. The background was subtracted statistically with a systematical error corresponding to half of the number of subtracted events.

6.2 Photoproduction background

Photoproduction events take place via the exchange of a quasi real photon with $Q^2 \leq 10^{-2} \text{GeV}^2$. This implies that the electron is not detected in the main detector but

escapes through the beampipe. Only a small fraction of the events has the electron identified in the electron tagger at -33.4 m upstream the detector in the proton direction.

Though this class of events contains interesting physics processes its high cross section of $\sigma_{\gamma p}^{tot} = 156 \pm 2(\text{stat}) \pm 18(\text{syst}) \mu\text{b}$ [66] compared to the DIS cross section of only $\sigma_{DIS} = 92 \pm 11(\text{stat}) \pm 12(\text{syst}) \text{nb}$ [67] makes it the dominant background source for DIS events. The hadrons produced in the event can mimic an electron since the means to identify electrons in the backward region are quite poor. Therefore a crucial point in the analysis of the proton sturcture function is the purification of the event sample from photoproduction events. They dominate our sample at low energies. Some handles to suppress the background are discussed in the following sections. We finally present a method to exclude part of the γp events and get an estimate of the remaining contribution.

6.2.1 Classification of photoproduction events

The photoproduction events which mimic a DIS event can be classified as follows:

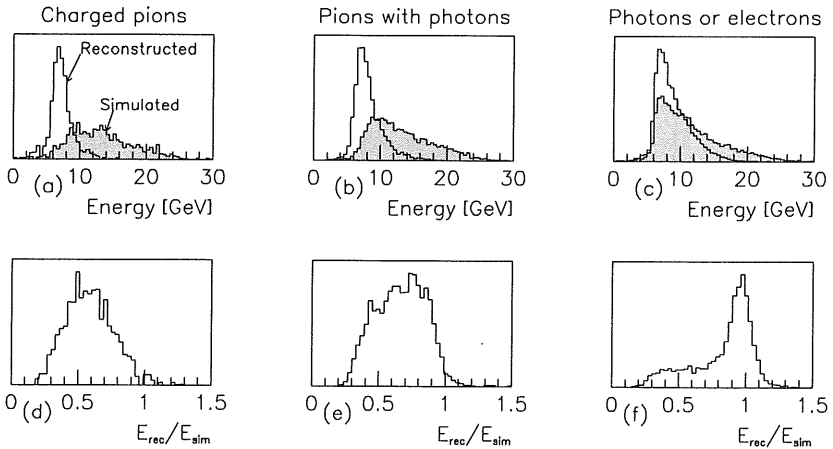


Figure 6.1: Monte Carlo simulations: Reconstructed energy deposited in the BEMC (open histograms) compared to the simulated energy (hatched histograms) for different particles in photoproduction events. Figures (d)-(f) give the ratio of reconstructed to simulated energy.

1. Charged pions: The insensitivity of the BEMC to hadronic energies shifts the reconstructed energy of the pion to lower values. This is illustrated in Figure 6.1 (a) and (d)

by a comparison of the simulated to the reconstructed energy in a sample of simulated photoproduction events. No background rejection cuts are applied yet. The only requirement for the simulated sample was a simulated hadronic energy flow in backward region of more than 4 GeV and a minimal reconstructed cluster energy of 1 GeV. The cut on the minimum energy deposited in the BEMC implies that the particles which pass the calorimeter as minimum ionizing particles are not visible. The pions which have a reconstructed cluster in the BEMC have in average only 50% of their energy deposited, therefore this class of photoproduction events contributes only to the very low energies.

2. Pure photons: their energy is correctly measured in the BEMC but they are not detected in the central tracker or the BPC unless they convert into electron positron pairs (see point 4).
3. $\gamma\pi^\pm$ overlap: these events may heavily affect the DIS sample, because a high energy cluster is induced by the photon whereas a BPC point and eventually a track is measured from the charged pion. This leads to a misidentification if the γ and the π are close. The comparison of the reconstructed to the simulated energy in Figure 6.1 (b) and (e) illustrates, that the events with a pion accompanied by a photon have their reconstructed energy closer to the generated one, with an average energy deposit of 75% of the simulated energy.
4. π^0 and converting photons: π^0 s already decay within the interaction region into two photons (lifetime $0.87 \cdot 10^{-16}$ s [68]). The photon may convert in the dead material into an electron and a positron, mostly in the endflanges, electronics and cables situated between the central tracker and the BPC or in the beam pipe. The energy of the electron or the photon is generally well reconstructed (see Figure 6.1 (c) and (f)). This class of events proved to be the main background source since there is no possibility to distinguish the cluster of (converted) photons from genuine electrons and even the requirement of a hit in the BPC does not help to suppress background induced from converted photons.

The relative contribution of electron like and pion like clusters as a function of the reconstructed energy is illustrated in Figure 6.2 for events fulfilling the DIS event selection criteria, which essentially means a BPC hit close to the energy cluster. Clusters are identified as 'pion like' if more than 30% of the cluster energy is carried by charged pions, 'electron like clusters' on the contrary have only a marginal part of the simulated energy belonging to charged pions (less than 10%). About 15% of the event sample could not be identified according to this simple scheme due to overlap of pions and electrons. It should be noted, that the requirement of a BPC hit implies that single photons do not contribute to the distributions in Figure 6.2.

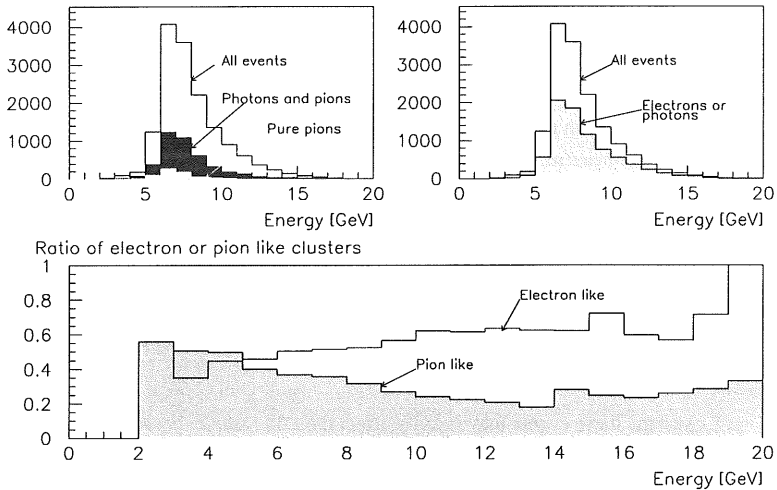


Figure 6.2: Energy deposited in the BEMC for 'pion like' and 'electron like' clusters after the DIS event selection cuts, using Monte Carlo simulated events. 'Pion like' clusters have 30% of the simulated energy carried by the pion whereas 'electron like' clusters have less than 10% energy contribution from pions. At high energies the photoproduction background is dominated by 'electron like' clusters'

Obviously the contribution of pion induced clusters diminishes towards high energies such that the main contamination at high energies is induced by 'electron like' clusters. They are usually due to high energy photons accompanied by a charged particle or converted photons.

6.2.2 Tagged events

Part of our event sample at low energies (below 15 GeV) can be identified as photoproduction events because the scattered electron is measured in the electron tagger located at $z=-92.3$ m where the electron ring is bended. This subsample is a good handle to check the efficiency of different background cuts, but the low acceptance of the e -tagger, which depends on the event kinematics and therefore on the event sample in question, makes it difficult to deduce accurate numbers for a statistical subtraction of the background. The e -tagger is sensitive to scattered electrons with an energy above 4 GeV and a scattering angle of 0-5 mrad. Before drawing conclusions from the number of tagged events one has to take into account a possible overlay of deep inelastic events with Bethe Heitler events which have a visible cross section of 29 mb [69]. The high acceptance of the photon tagger of 98% [51] makes it easy to identify

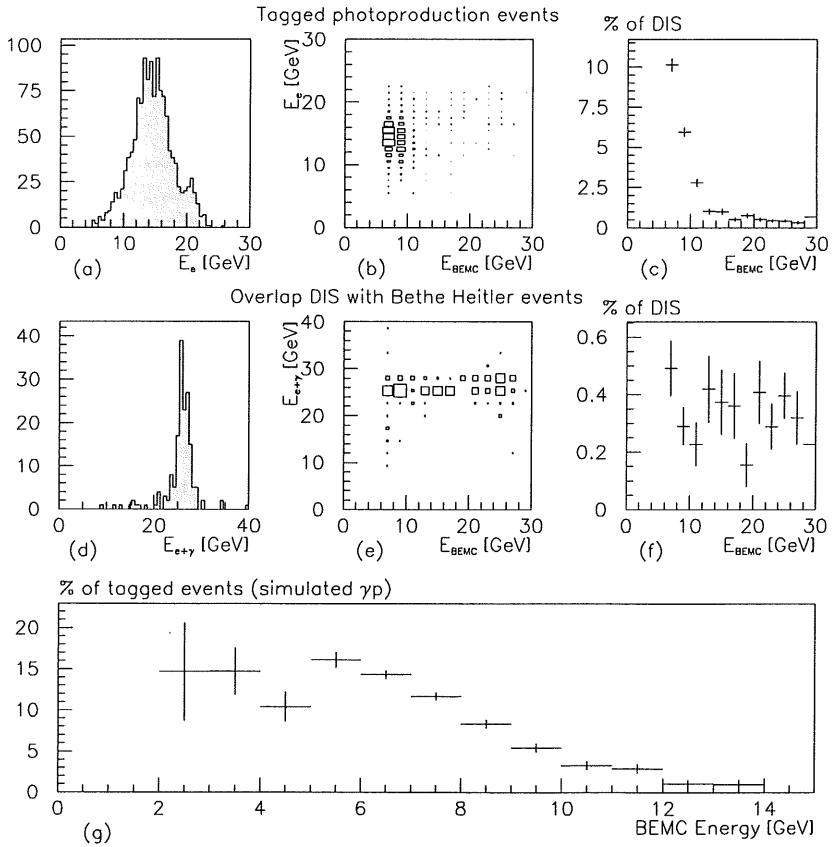


Figure 6.3: Contribution of tagged photoproduction events to the DIS event sample, no background cuts are applied yet. (a) shows the energy spectrum in the electron tagger, and (b) the correlation with the energy of the highest cluster in the BEMC with the luminosity overlap events excluded. The relative contribution of the tagged events to the whole sample is shown in (c). The overlap of DIS events with Bethe Heitler events is illustrated in Figures (d)-(f). The total energy in the photon and electron tagger peaks at the beam energy (d), with the relative contribution of the order of 0.3% independent of the energy. Figure (g) gives the percentage of tagged events as a function of the energy of the highest cluster in the BEMC for simulated γp events.

these events by a cut on an energy deposit in the γ tagger larger than 2 GeV. The energy spectrum in the e -tagger for the DIS event sample, with the overlap events subtracted is shown in Figure 6.3 (a). The photoproduction events are mainly located at low energies measured in the BEMC (6.3 (b) and(c)), with a contribution of up to 6% at 8 GeV. Given the acceptance of the electron tagger, which is of the order of 8% (6.3(g)) this corresponds to a huge contamination of the selected event sample at low energies. Since the acceptance of the e -tagger depends on the event kinematics it varies with the energy of the highest energy cluster in the BEMC, this is illustrated in Figure 6.3 (g) for simulated γp events. The acceptance varies between 15% at very low energies, becomes less than 5% for energies larger than 10 GeV and vanishes for BEMC energies above 15 GeV. The tagged events above 15 GeV which give a constant contribution of the order of 0.5% have therefore to be attributed to random coincidences.

The overlap of DIS events with Bethe Heitler events is illustrated in Figure 6.3 (d)-(f). The total energy in the photon and electron detector peaks at the nominal beam energy (d) as expected for these luminosity events. The ratio of these overlap events is constant over the whole energy range and of the order of 0.3% (f). Given the acceptance of the luminosity detectors (38% for the e -tagger and 98% for the γ tagger) for Bethe Heitler events with a visible cross section of 29 mb [69], and the specific luminosity of $10^{30} \text{ cm}^{-2}\text{s}^{-1}$ the luminosity events are expected to have a rate of 11 kHz. The typical rate including background was measured to be 15 kHz. This leads to an estimated probability for an overlap of genuine DIS and Bethe Heitler events of 0.3% per bunch which agrees perfectly with the measured value.

6.2.3 Cut on the distance to the closest BPC hit

A cut on the distance between the cluster c.o.g. and the closest BPC hit is a very powerful tool to suppress photoproduction background, furthermore the existence of a BPC hit is required for an accurate measurement of the angle of the electron. Since this cut is already applied in the selection the control of losses of good DIS candidates due to this cut is a critical part of this analysis. The rejection power of the BPC cut is illustrated in Figure 6.4 using simulated photoproduction events. A distance of the closest BPC hit of less than 5 cm rejects about 40% of the γp events, almost independent of the energy of the cluster (6.4 (a)). Figures 6.4 (b) and (c) show that the BPC cut essentially reduces the number of clusters with $\gamma\pi$ overlap and the 'electron like' clusters, by rejecting clusters initiated by a single photon.

Below we will carefully discuss the efficiency for DIS events. The intrinsic BPC efficiency was already discussed in chapter 4.2.1, here we are interested in the efficiency to find a reconstructed BPC hit close to a given cluster in the BEMC. We studied several methods using the events in the kinematical peak or events with a tracking information belonging to the electron candidate to access the total energy range.

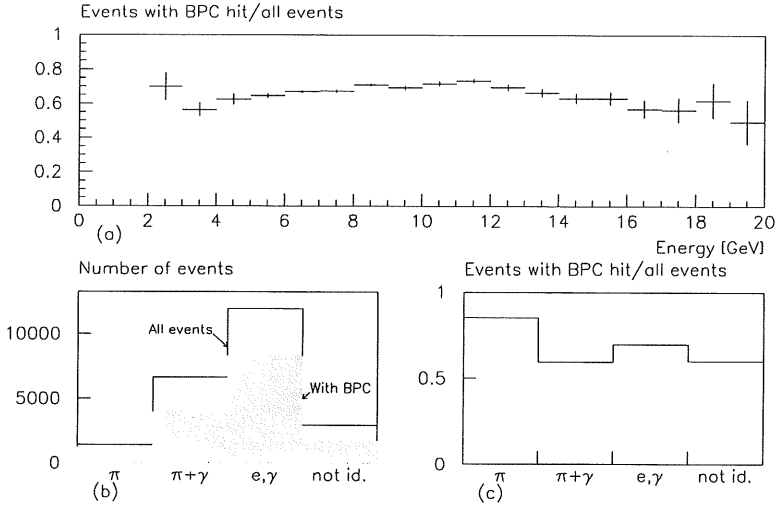


Figure 6.4: Rejection of photoproduction background by a cut on the distance of the closest BPC hit (DBPCL) less than 5 cm, using simulated photoproduction events. Figures (b) and (c) show the rejection power for different particle types (see text for definition).

Kinematic peak events A sample of events was selected with the energy of the electron candidate between 22 and 28 GeV, a radius of the cluster between 14.7 and 71 cm, to be inside the BPC acceptance, a cut on the lateral size of the cluster and a vertex reconstructed in the interaction region ($-30 \leq z_{vertex} \leq 20$ cm). The high energy required ensures that there is only a marginal background contribution. Figure 6.5 (c) shows the distance of the closest parallax corrected BPC point to the cluster center of gravity (DBPCL), the cutsize of 5 cm is well justified by the distribution. The radius dependency (Figure 6.5 (a)) shows the expected edge effects at large and small radii, due to the finite resolution of the BEMC cluster position and the smearing of the z -vertex by 20 cm. The efficiency is shown enlarged in Figure 6.5 (b) in comparison with the efficiency expected from the intrinsic single plane efficiency. Generally, the efficiency deduced from the single plane efficiencies is lower, since preshowering in the dead material increases the probability to find a hit close to a cluster. The statistics is very limited at large radii for the kinematic peak sample, however it seems not to confirm the radius dependency observed for the single planes. This can again be explained by preshowering which smears out the radius dependency. Neglecting the edge effects we get an efficiency of $95.9 \pm 0.1\%$ in this high energy region.

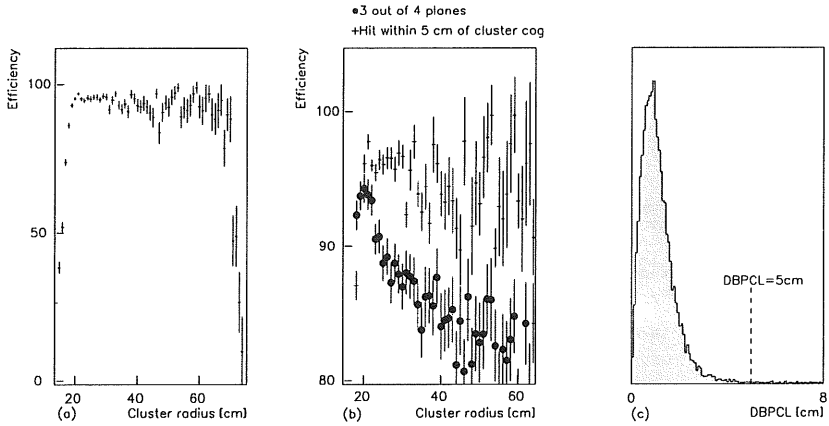


Figure 6.5: Radius dependency of the efficiency for finding a BPC hit within 5 cm for kinematic peak events (a), the dots show the expected value from the intrinsic plane efficiency (b). The DBPCL distribution is shown in Figure (c).

Total energy range The simple method discussed above cannot be used in the whole energy range we are interested in, since at low energies we suffer from background contamination which is dominated by photoproduction events. Background induced by photons leaves a considerable energy deposit in the BEMC but no hit in the BPC, unless the photon converted in the dead material in front of it. These events can be rejected by asking for a tracking information correlated to the BEMC cluster. More difficult to recognize are events with $\gamma\pi^\pm$ overlap. The pion leaves a track in the central tracker but not necessarily the high energy cluster which may result from the photon. Therefore we used two samples to access the full energy range. The first one requires a CJC track pointing to the cluster c.o.g. within 5 cm (sample 1). This is a good identification for DIS events, but its statistics is limited. A second sample was defined by requiring a CIP hit lying on the line BEMC-vertex as an identification of the electron (sample 2). Figure 6.6 (a) shows the energy dependence of the DBPCL cut for the sample with a CIP hit and a sample with no further background rejection, clearly showing the usefulness of the DBPCL cut for γ induced background rejection. However, even the use of the CIP track criterion does not fully erase the energy dependence. This illustrated in Figure 6.6 (b) in an enlarged scale. Since the use of the strong tracking criterion (sample 1) gives no further information due to its large statistical error (6.6 (c)), more tests have to be performed to understand the energy dependence. For all the following discussions the

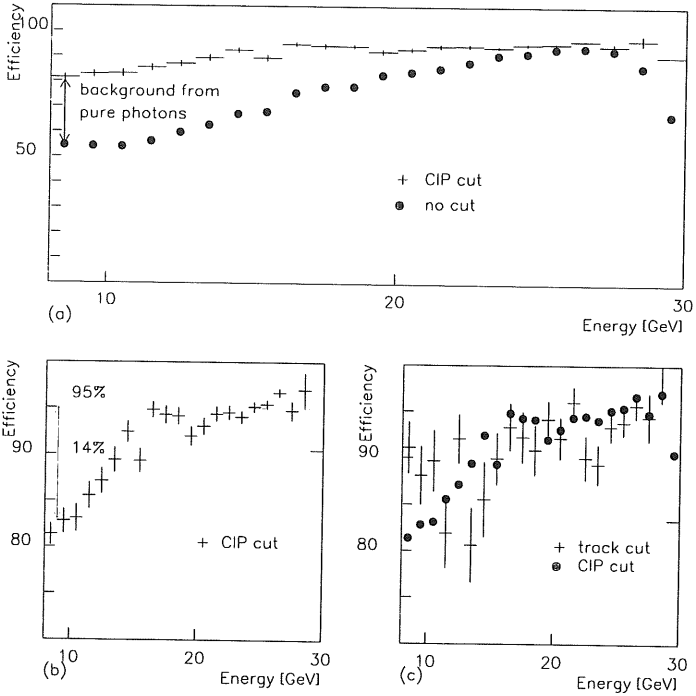


Figure 6.6: Efficiency of the DBPCL cut as a function of the energy for the DIS sample. (a) shows the rejection of photon initiated clusters by the cut on DBPCL. (b) and (c) give the energy dependence of the cut for two different cuts against photoproduction background.

sample with a CIP hit was used. Besides a remaining contamination with photoproduction events, possible reasons could be found in detector related effects:

- Different amount of preshowering. The number of BPC hits within 5 cm of the cluster c.o.g. as a function of the energy is shown in Figure 6.7(a). Obviously the distribution of the number of hits is slightly energy dependent. Despite the average number of hits being constant and equal to 2.4 the number of events with more than one hit increases towards lower energies (Figure 6.7(b)). This might be attributed to photoproduction events, which have a higher multiplicity of particles. But no evidence is seen that the amount of preshowering decreases for lower energies, therefore it cannot explain the observed loss in efficiency.

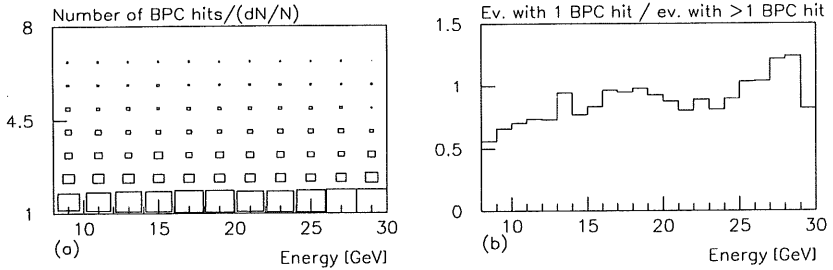


Figure 6.7: Number of hits - normalized to the number of events per energy bin - within 5 cm of the cluster c.o.g. as a function of the energy (a). The ratio of events with only one BPC hit to events with more than one hit is given in (b).

- Cluster center of gravity reconstruction: The reconstruction of the cluster position is more influenced by stacks affected by noise towards lower energies. This might induce the BPC point to be outside of the 5 cm cut. Indeed Figures 6.8 (a) and (c) show a broadening of the normalized DBPCL distribution towards lower energies with the mean value shifted by about 1 cm, but gives no evidence of a loss of the order of about 14% for events at 8 GeV. It is obvious that a cut at 5 cm cuts in the tail of the distribution, but this would only result in a small efficiency loss. The percentage of events lost in the tail of the distribution is illustrated in Figure 6.8(b) for three different cuts. For a reasonable cut at 6 cm, only an increase of the order of 0.5% in the high energy part which amounts to up to 2-4% at very low energies is observed. Again this does not explain the large loss in efficiency. The number of clusters in the BEMC is also rising with the energy decreasing, due to the hadrons pointing backwards (d). This leads to more hits in the BPC and therefore the rise in the number of events outside 5 cm -illustrated for a cut of 8 or even 10 cm in Figure 6.8 (b)- can be attributed to random coincidences.

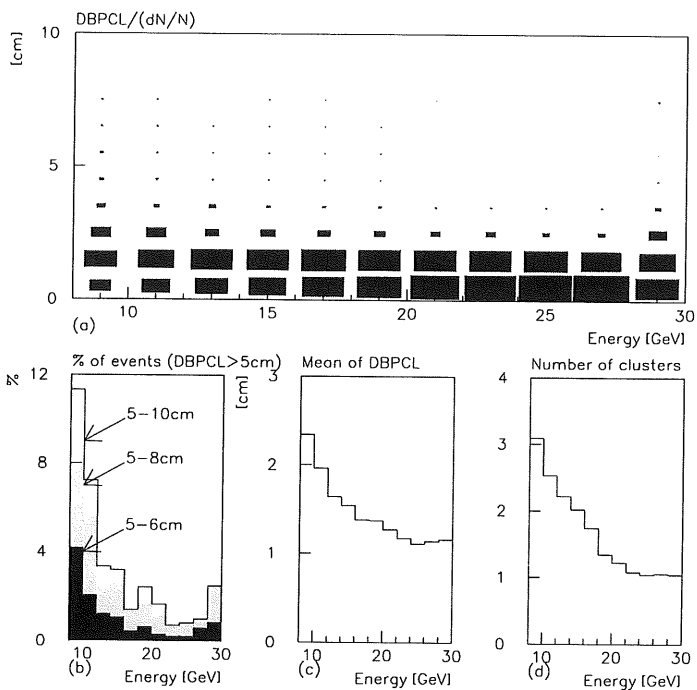


Figure 6.8: Distribution of DCLBP vs energy (a), normalized to the number of events per energy bin for data with a CIP hit. A broadening is observed better visible in the distributions below, as average value of DBPCL (c). The percentage of events missed by the cut at 5 cm is shown in (b) for three different cut values. Finally the energy dependence of the number of clusters in the BEMC is shown in (d).

Evidence for a background induced energy dependence of the DBPCL cut will be discussed in the following. The low energy sample ($E \leq 15 \text{ GeV}$) with a CIP hit was divided into a part fulfilling the DBPCL cut and a part rejected by the cut on the BPC hit. Different background estimators, which are discussed in more details in the next sections, were tested using the different samples. If it was background we expect to see a clear difference in the distributions for the two samples.

- Lateral cluster size (Figure 6.9(a)): Although the sample without a BPC hit has a tendency to have a broader distribution, no obvious difference between the two samples is visible. This implies that the major part of the particles in question are either electrons or photons.

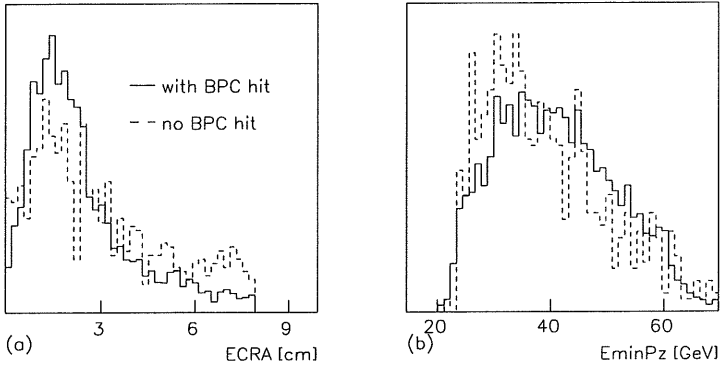


Figure 6.9: Background estimators: (a) lateral cluster size and (b) missing backward energy E_{minPz} for events below 15 GeV with (full line) and without (dashed line) a BPC hit within 5 cm of the cluster c.o.g.

- Missing backward energy (E_{minPz}) (Figure 6.9(b)): For genuine deep inelastic events we expect to see the events at $E_{\text{minPz}} = 2E_e = 53.2 \text{ GeV}$. However, the sample with a BPC hit does not show the expected distribution. It is clearly shifted to lower energies, due to the fact that hadrons escaping in the backward area or which are badly measured in the BEMC, do less contribute to the sum and because events with initial state radiation have a lower energy. But the sample with no BPC hit is shifted to even lower energies, which indicates that part of the sample are photoproduction events. The obvious suffering from lost particles pointing backwards, makes it impossible to quantitatively distinguish between DIS and photoproduction events in this energy region using E_{minPz} .

- Electrons detected in the electron tagger: these events can be identified as photoproduction events, but due to the limited acceptance of this detector device, this measurement just gives a hint on the remaining contribution to the whole sample. The ratio of the tagged to the untagged sample is given in Table 6.1, before (column 4 and 5) and after the correction of the overlap of DIS with Bethe Heitler events (column 6 and 7). A comparison of columns 4 and 6 of Table 6.1 shows that the requirement of no energy in the photon tagger drastically reduces the number of identified photoproduction events for the high energy part. The percentage of identified photoproduction events is given in the last column of Table 6.1. Apparently the events with no BPC hit and energies below 22 GeV are contaminated by photoproduction events by 4% divided by the acceptance of the electron tagger. Given the acceptance deduced from Monte Carlo simulations of 6% (for energies above 8 GeV) with a large uncertainty of about 100% the contribution of photoproduction events to the sample with no BPC hit is expected to be of the order of 70%.

	Energy	Events	energy in electron tagger		energy in e -tagger but not in γ -tagger	
			Events	%	Events	%
with BPC hit	$E \leq 15$ GeV	4777	79	1.6 ± 0.2	40	0.9 ± 0.1
	$15 \leq E \leq 22$ GeV	5150	48	0.9 ± 0.1	14	0.2 ± 0.06
	$E \geq 22$ GeV	8981	59	0.3 ± 0.05	5	0.06 ± 0.08
no BPC hit	$E \leq 15$ GeV	891	63	7.0 ± 0.9	39	4.3 ± 0.7
	$15 \leq E \leq 22$ GeV	394	60	6.3 ± 1.3	14	3.6 ± 1.0
	$E \geq 22$ GeV	471	35	7.4 ± 1.3	4	0.8 ± 0.4

Table 6.1: Identified photoproduction events in the DIS sample.

The contribution of photoproduction events rejected by the BPC cut to the whole sample with a CIP hit is listed in Table 6.2. Despite the large uncertainty in the acceptance of the electron tagger, it shows that the main part of the lost events can be attributed to photoproduction events.

To summarize we conclude that the cut on the distance of closest BPC hit seems to be independent of the energy with a possible loss of events at low energies of the order of 1-2% due to a slightly worse reconstruction of the cluster position. A possible loss in efficiency towards large radii is smaller than expected from the intrinsic BPC efficiency and amounts to at most 2-4%.

Energy	Events	no BPC hit		photoproduction contribution*	
		Events	%	Events	%
$E \leq 15$ GeV	5668	891	15.7	39/0.06=650	11
$15 \leq E \leq 22$ GeV	5544	394	7.1	14/0.06=233	4.2
$E \geq 22$ GeV	9452	471	5.0	4/0.06=66	0.7
* corrected for the e -tagger acceptance					

Table 6.2: Photoproduction events rejected by the BPC cut.

6.2.4 Cluster size distribution

As it was already shown in the Chapter 4.2.2 the BEMC has a very different response for electrons and hadrons. Genuine electrons generally produce well localized showers concentrated in one or two stacks, whereas for hadrons the energy is spread much broader. Therefore one defines the energy weighted cluster radius, ECRA, a measure of the lateral size of the cluster, as the energy weighted sum of the distance between the stack and the cluster c.o.g. of all stacks.

$$ECRA = \frac{1}{E_{Cluster}} \sum_{stack\ j} E_j * |r_j - r_{c.o.g.}| \quad (6.2.2)$$

Figure 6.10 shows the lateral cluster size for simulated photoproduction events with the expected difference of the distributions for electromagnetic (b) and hadronic clusters ((c) and (d)). The hatched histograms show the effect of the BPC cut.

For simulated DIS events the distribution is much narrower and most of the clusters have a lateral cluster size of less than 5 cm (Figure 6.11 (a)). However, the simulation shows that the estimator is slightly energy dependent though the definition is energy independent. This is illustrated in Figure 6.11 (b) where the cluster radius, normalised to the number of events per energy bin, as a function of the cluster energy shows a broadening of the distribution towards low energies. This effect was already observed in test beam data [59] and attributed to the influence of noise. Therefore a cut at 5 cm, which would reject a large fraction of the photoproduction events cuts into the DIS signal at energies below 15 GeV (c), leading to a loss of events of 5-25% for energies below 10 GeV. This means that at low energies the control of the loss of DIS events relies on a correct simulation and a good understanding of the BEMC calibration and reconstruction. In the following ECRA is not used as a cut against photoproduction events but only as an estimator for a cross check of other cuts.

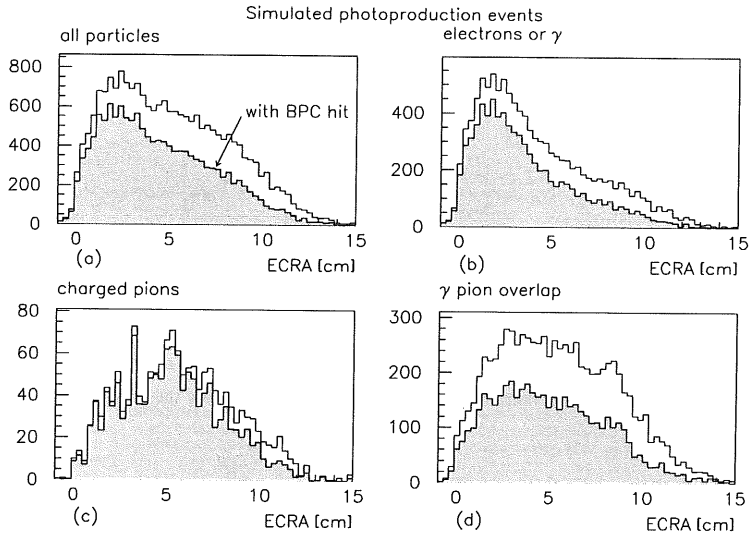


Figure 6.10: Lateral cluster size ECRA for simulated photoproduction events with a reconstructed energy larger than 5 GeV, the empty histograms have no background cuts applied, the hatched histograms fulfill the BPC requirement. A clear difference in the distribution for different particles is observed.

6.2.5 Missing backward energy distribution

The kinematical variable y was defined in chapter 3 by making use either of the hadronic measurement:

$$y_h = \frac{1}{2E} \sum_h (E_h - p_{zh}),$$

where the sum runs over all detected hadrons, or by the measurement of the electron (E_e, ϑ)

$$y_e = 1 - \frac{E_e}{E} \sin^2\left(\frac{\vartheta}{2}\right) = 1 - \frac{E_e}{E} \frac{1 - \cos \vartheta}{2} = 1 - \frac{1}{2E} (E_e - p_{ze}).$$

By a combination of the two measurements we get:

$$E_{min} P_z := \sum_{all\ particles} (E - p_z) = 2E(y_h + 1 - y_e) = 2E \quad (6.2.3)$$

with E the incident electron beam energy. The above equation is true for events with no initial state radiation unless the photon is detected in the γ -tagger. However, only a fraction of initial state photons are measured in the photon tagger which shifts the measured $E_{min} P_z$

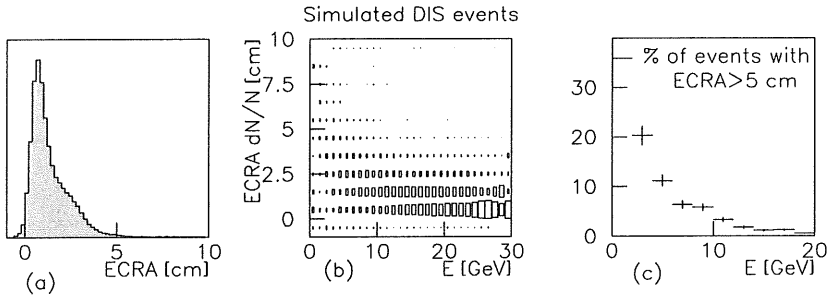


Figure 6.11: Energy weighted cluster radius (ECRA) for simulated DIS events (a). (b) shows the energy dependence of this background estimator. A cut at 5 cm cuts into the DIS signal at energies below 15 GeV (c).

value for radiative events to lower values. Therefore an E_{minPz} cut always implies a cut on radiative events. Photoproduction events have their scattered electron generally not detected and hence an E_{minPz} value much lower than expected for DIS events. Figure 6.12 (a) shows the E_{minPz} distribution for simulated DIS events. The distribution peaks at $2 \cdot E_e$, but has long tails towards low energies due to undetected particles. Particles missed in the forward region hardly influence the reconstructed value of E_{minPz} , whereas particles escaping undetected in the backward region shift the sum to lower values. Since at low energies the hadrons are pointing backwards and are not detected or are badly measured in the BEMC, E_{minPz} becomes a worse estimator. The E_{minPz} distribution for events with an energy of the scattered electron less than 15 GeV (without radiative events) is plotted in Figure 6.12 (b). Clearly a cut on E_{minPz} would cut into the signal of genuine DIS events. The energy dependence of the E_{minPz} distribution is shown in Figure 6.12 (c). A sensible reduction of photoproduction background needs a minimal cut at $E_{\text{minPz}}=30$ GeV. Therefore a control of losses of DIS events requires a good Monte Carlo description of the BEMC hadronic measurement and the particle flow at low energies. For these reasons we used this cut only as a cross check. As an illustration Figure 6.12 (d) shows the distribution for DIS events with initial state radiation and the photon measured in the γ -tagger, which is well above 30 GeV, by not taking into account the response of the γ -tagger (empty histogram) the measurement gets useless, since there is a large fraction of missing energy.

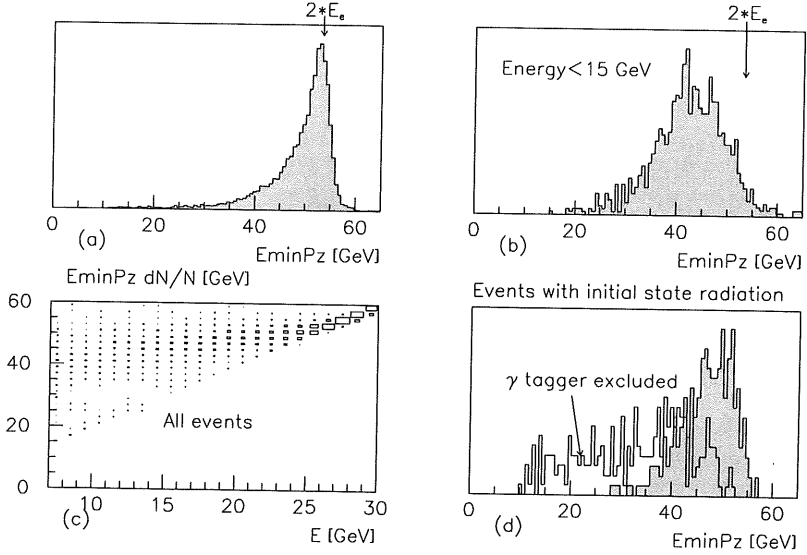


Figure 6.12: Missing backward energy (E_{minPz}) for simulated DIS events. (a) All scattered electron energies, (b) electron energy below 15 GeV, (c) energy dependence induced by particles escaping in the backward area. Figure (d) shows the large error induced to the measurement by not taking into account the γ -tagger response for events with initial state radiation.

6.2.6 Using the tracker information

The information of the central tracker can be used to identify events with a photon converting in the dead material between the central tracker and the BPC into an electron and a positron, and $\gamma\pi$ overlap events with secondary vertices. This turned out to be the major contribution. The aim of this study was to identify these events by using the information provided by CIP and CIZ and to get an estimation of the remaining γp contribution from data. Monte Carlo events were mainly used for confirmation.

Event sample and method Clearly the CIP-CIZ information cannot be used in the whole angular acceptance region of the BPC, therefore we restricted our sample to events where the inner CIP is intersected at z larger than $z_{min}=-110$ cm. The CIP pads and CIZ segments were found as follows: First the intersection of the line BPC-Vertex with each chamber plane was defined as reference point, then the hit with minimal distance in z to this point was searched, if the hit was within $\Delta\varphi=25^\circ$. The cut-off value in φ is determined by the

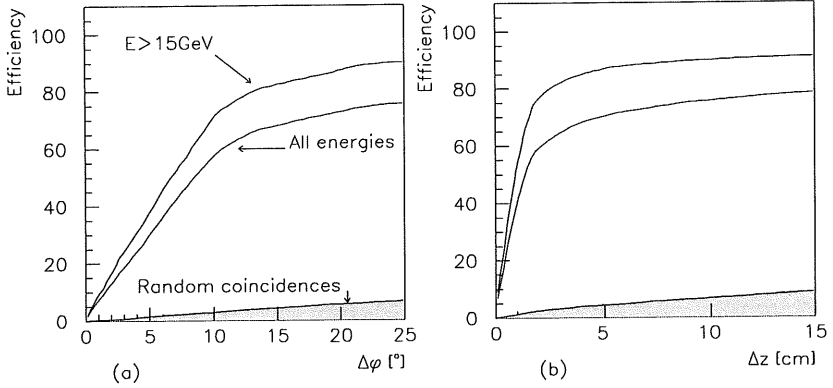


Figure 6.13: Efficiency for finding a CIP or CIZ hit in function of the minimal distance in φ and z to the intersection of the line BPC-Vortex with the inner CIP plane. The efficiency is shown for energies above 15 GeV as well as for all energies which already shows the reduction due to photoproduction events. The hatched region gives the amount of random coincidences.

chamber resolutions, given by the pad size of 45° for CIP and the φ resolution of CIZ which depends on the signal size. (see Figure 6.13 (a)). Finally a combined hit - further referred to as CIPCIZ hit - is reconstructed, by combining all CIP and CIZ hits within a distance of 2σ to the one with the minimal distance to the intersection, where σ denotes the z resolution of the single hits. Usually the combined hit was obtained from by one or two planes of the CIP. CIZ could not be used in the very backward part with the highest statistics, since the last ring, covering the region $-108 \leq z \leq -96$ cm was at reduced voltage and not efficient.

Efficiency and random coincidences The efficiency of this method was determined in a region where we expect a negligible rate of $\gamma\gamma$ background, the energy of the electron was chosen to lie between 15 and 25 GeV. The efficiency as a function of the minimal distance of the closest hit in any of the chambers, Δz_{min} is shown in Figure 6.13 (b). In the same plot the amount of random coincidences is shown. The random coincidences were studied by changing the φ value of the reference point by $\Delta\varphi = 40$ up to 180° . No dependence on $\Delta\varphi$ was found. The random coincidence rate is energy dependent since the current jet points backwards for low energies and therefore gives additional hits spread in φ .

Full efficiency is reached with a cut on $\Delta z_{min} = 5$ cm, this value is given by both the chamber and the z -vertex resolution. However the final cut size was chosen to be 10 cm in order to avoid any energy dependence of the cut which would be hard to control. The random

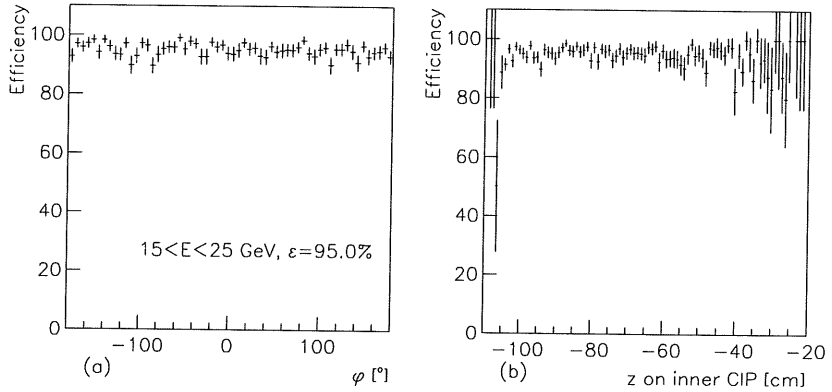


Figure 6.14: Efficiency for finding a CIP or CIZ segment for electron energies between 15 and 25 GeV as a function of the azimuthal angle φ (a) and the z position of the line BPC-vertex on the inner CIP (b).

coincidence rate is almost independent on whether one or more than one chamber is required to be active. This means that the contamination comes from true hits rather than noise hits. Therefore we require at least one active chamber in order to compensate for the known chamber deficiencies. No dependence of the efficiency on φ is seen (Figure 6.14 (a)), whereas the dependence on the z position of the intersection (6.14 (b)) shows the expected edge effects at the chamber end. The efficiency in this special energy region is determined to be 95.5% which compares well with the chamber efficiencies discussed above. It was also investigated to use single CIZ hits instead of CIZ segments, but it was found that the random coincidence rate was too high.

The events with no CIPCIZ hit were scanned and found to be due to

- Edge effects at the chamber end, visible as a drop in the efficiency in Figure 6.14 (b) for $z \leq -100$ cm.
- True inefficiencies: mostly they occur in periods, where the high voltage was not switched on (this was not required in the selection). If one requires the high voltage to be switched on the efficiency rises to 98%.
- Wrongly determined vertices: Usually events with only few or badly measured tracks. If the vertex position is wrong by more than 10 cm, the CIPCIZ hit cannot be found,

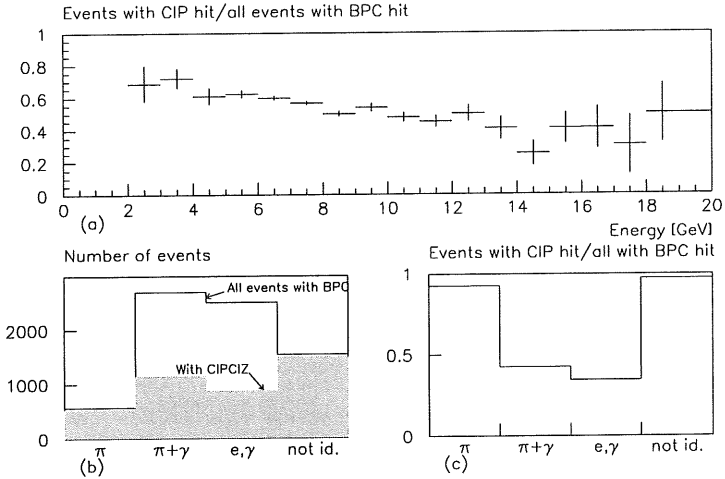


Figure 6.15: Reduction of photoproduction events by the CIPCIZ cut using simulated events. The effect of the cut for clusters initiated by different particle types is illustrated in (b) and (c). The difference in the relative contribution of different cluster types compared with Figure arises out of the different acceptance of the CIPCIZ cut.

$\gamma\pi$ background reduction Figure 6.15 shows the expected reduction of photoproduction events by applying the CIPCIZ cut to simulated events which fulfilled the DIS selection criteria. The percentage of rejected events varies between 60% at high energies and 40% at 4 GeV (6.15 (a)). As expected the cut acts differently on different cluster types. Clusters with pure pions are not affected but the cut is very effective for clusters initiated by converted photons, with a reduction of over 60%, and also reduces $\gamma\pi$ overlap events by 45% (6.15 (b) and (c)). The rejected $\gamma\pi$ overlap events were investigated and found to be events with a converting high energy photon and a low energy pion. The BPC hit required in the selection was then initiated by the converted photon and not by the pion.

Figure 6.16 shows the number of events of the DIS data sample with a CIPCIZ hit divided through the number of all selected events in function of the electron energy. We distinguish three regions:

- $15 < E < 25$ GeV: constant ratio which gives us the energy independent efficiency of the cut. The 4% difference to the simulated efficiency can be explained by periods with the high voltage of the chambers switched off (2-3%) and a slightly worse vertex reconstruction.

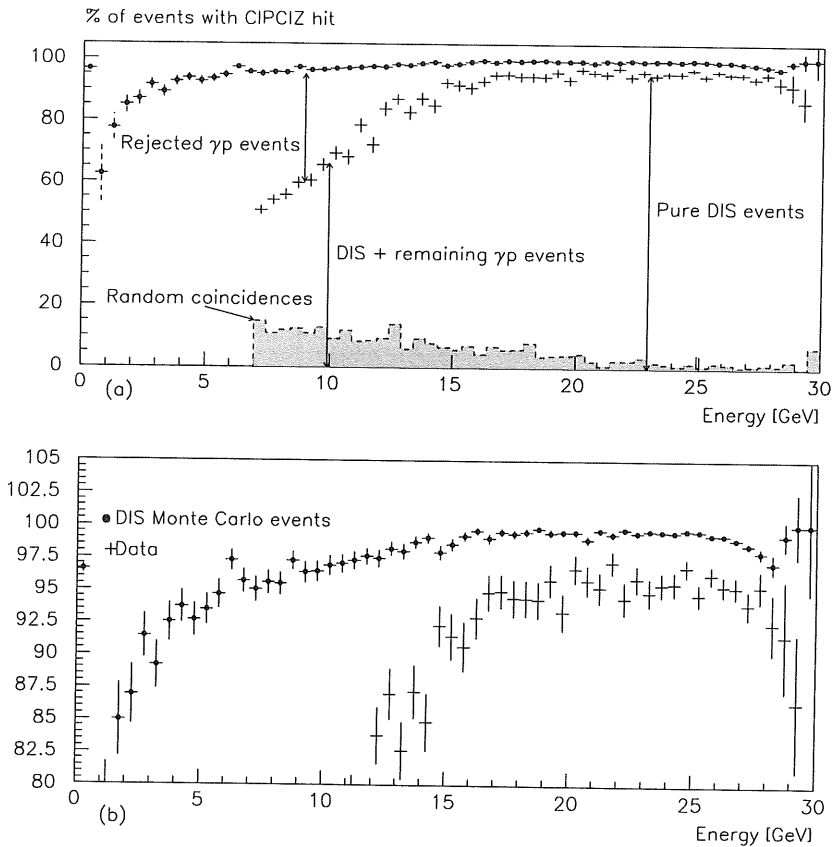


Figure 6.16: Percentage of events with a CIPICIZ hit as a function of the electron energy. The high energy behaviour is nicely described by DIS Monte Carlo events (points). The drop at low energies for the simulated events stems from misidentified electrons, whereas the difference between simulated and measured efficiency corresponds to the rejection of photoproduction events at low energies. The dashed curves correspond to the amount of random coincidences. The energy dependence is shown on an enlarged scale in Figure (b).

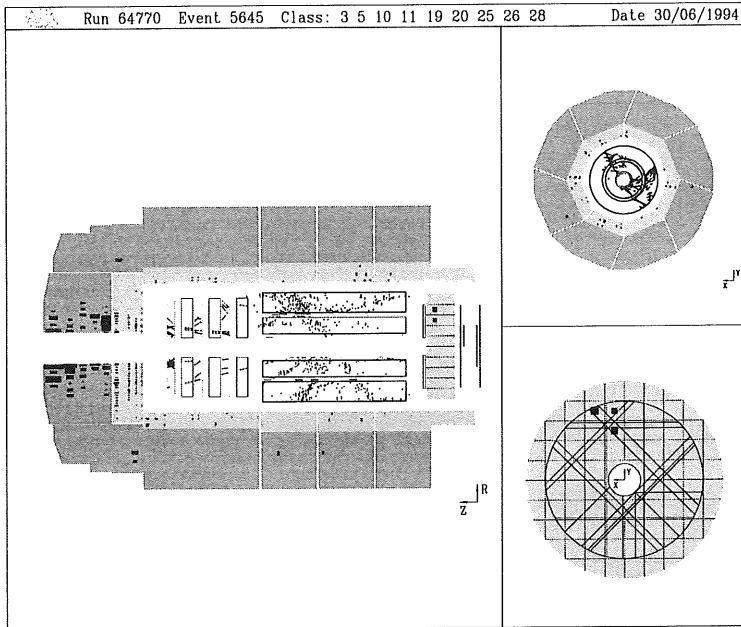


Figure 6.17: A typical γp event which can be rejected using the CIPCIZ information. The photon is converting in the endplate of the central tracker.

- $25 < E < 30$ GeV: the ratio drops, an effect which is also reproduced by the simulation. Scanning these events showed that for most of them the true CIPCIZ hit was there but could not be found because the vertex was wrongly determined. The vertex reconstruction is more difficult in this energy region, because the hadrons are going into the very forward direction. As a consequence, these events have only few tracks for the vertex determination.
- $E < 15$: In this region we see the effect of photoproduction contamination. Events with particles coming from secondary vertices or converting photons, with the conversion taking place at radii larger than the CIZ radius, can be rejected. The remaining events with a CIPCIZ hit are both true DIS events and γp events with charged pions, $\gamma\pi$ overlap or γ converting in the beampipe faking an electron.

The events with energies between 10 and 15 GeV which were rejected by the CIPCIZ cut were scanned and part of it could clearly be identified as γp events. A typical rejected event is shown in Figure 6.17. At very low energies a distinction by eye is not possible. Therefore we checked the cut by using the estimators ECRA and EminPz (see Figure 6.18). The ECRA distribution shows an obvious difference between the samples with and without CIPCIZ hit. By comparing with the Monte Carlo distributions (see Figure 6.10) we conclude that the sample rejected by the cut is a mixture of 'pion like' and 'electron like' clusters. The sample after the cut looks very clean. Figure 6.18(b) shows the ratio of the events after the CIPCIZ cut to all events as a function of ECRA. The rejection power for 'pion like' clusters is 50% which is slightly better than the Monte Carlo expectation. The EminPz distribution ((d)-(f)) illustrates that the cut rejects events with missing backward energy. Even for energies below 15 GeV where it is known that EminPz gets shifted to lower values for DIS events a clear difference in shape for the distributions with and without a CIPCIZ hit is visible, which proves that the rejected sample is dominated by γp events.

The energy dependence of the cut over the whole range can only be studied by using simulated DIS events. The efficiency for finding a CIPCIZ hit for simulated DIS events is plotted in Figure 6.16 as full circles. Besides the 4% difference due to periods with no high voltage or additional inefficiencies the simulation nicely describes the data points. The drop at very high energies due to a difficult vertex reconstruction is described by the simulation except for the low statistics region above 29 GeV. Since we chose the cuts for finding a hit large enough to avoid an energy dependence and since the vertex reconstruction is sufficiently well described by Monte Carlo, we can use the simulated energy dependence to access the low energy part. The simulated efficiency slightly drops towards very low energies, since we start to see the effect of misidentified electrons. The simple definition of the electron candidate being the highest cluster in the BEMC keeps a possible misidentification at low energies of the order of 4% at 8 GeV.

To summarize we can conclude that the CIPCIZ cut is independent of the energy of the electron for DIS events, except for events in the kinematic peak region. It was measured to be $95.5 \pm 0.3\%$ for the selected DIS sample. The background rejection power is of the order of 50%, its energy dependence will be discussed in the next section. Finally the CIPCIZ cut also rejects DIS events with wrongly identified electron candidates.

Estimation of the remaining γp background The ratio of events with a CIPCIZ hit (called N_{CIPCIZ}) to the ones without a CIPCIZ hit (denoted with $N_{\gamma p \text{ rej}}$) gives us a handle to measure the remaining contribution of γp events. In the following we assume that the sample contains only a negligible amount of γp events for energies above 15 GeV. N_{CIPCIZ} below 15 GeV contains true DIS ($N_{DIS \text{ kept}} = \epsilon_{DIS} N_{DIS}$) and γp ($N_{\gamma p \text{ remain}} = \epsilon_{\gamma p} N_{\gamma p}$)

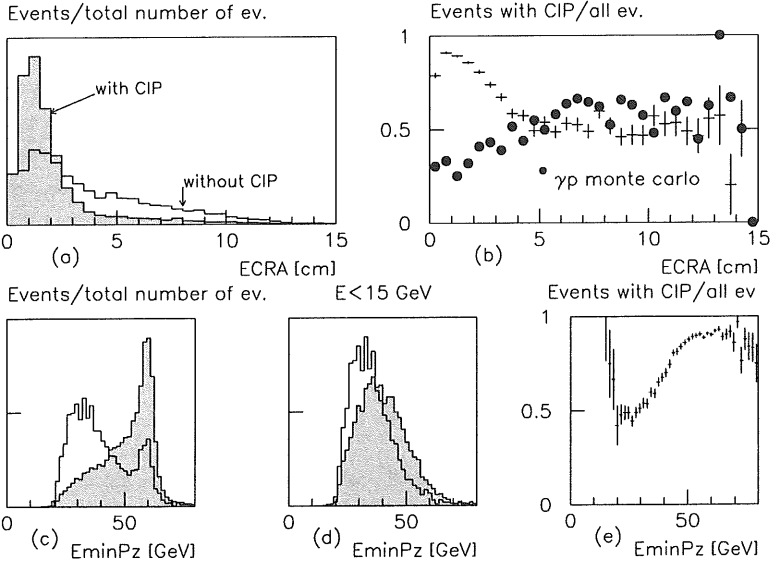


Figure 6.18: ECRA distribution for events rejected (empty histogram) and kept (hatched) by the CIPCIZ cut (a). The rejection of events with a large cluster radius is 50% (b), slightly better than the Monte Carlo expectation (points). (c) - e) show the effect of the cut in terms of the missing backward energy E_{minPz} , with a small peak at twice the nominal beam energy (c) for the rejected sample. This corresponds to the 4% loss of genuine DIS events.

events, with all these numbers being energy dependent. $\epsilon_{\gamma p}$ is the efficiency of the cut for γp events. Therefore we can write

$$N_{CIPCIZ} = \epsilon_{DIS} \cdot N_{DIS} + \epsilon_{\gamma p} \cdot N_{\gamma p} \quad (6.2.4)$$

where ϵ_{DIS} gives the efficiency for true DIS events including the drop due to misidentified electrons. It was deduced from simulation with a global correction of -4% as discussed above and parametrized by the simple function

$$\epsilon_{DIS} = \min(A, B + C \cdot E).$$

where the second part describes the loss due to wrong electron candidates. The constants were determined by a fit to the simulated efficiency for energies between 5 and 26 GeV. After the 4% correction it was determined to be

$$\epsilon_{DIS} = \min(95.5, 87.0 + 0.5 \frac{1}{GeV} * E)\%. \quad (6.2.5)$$

Similarly the measured efficiency ϵ_{meas} is described by the function

$$\epsilon_{meas} = \min(95.5, 11.0 + 6 \frac{1}{GeV} * E)\%. \quad (6.2.6)$$

The efficiency for γp events was determined both from data and from Monte Carlo simulation, containing hard and soft scattering processes in a ratio deduced from the experiment [70]. The data sample was defined by an electron measured in the electron tagger, a reconstructed vertex in the interaction region and a BPC point close to the cluster with an energy deposit in the BEMC of less than 15 GeV, to avoid random coincidences with the electron tagger (the acceptance of the e -tagger is negligible in this kinematical region, see Figure 6.3 (g)). Since the requirement of the electron measured in the e -tagger restricts the kinematics of the γp event, simulations have to be used to get the correspondance between the tagged and non tagged part of the γp sample. Figure 6.19 gives the efficiency of the CIPCIZ cut for simulated photoproduction events (full circles) and simulated tagged events. The rejection power of the cut is 12.5% higher for the tagged sample with a similar energy dependence. The energy dependence was parametrized by the function

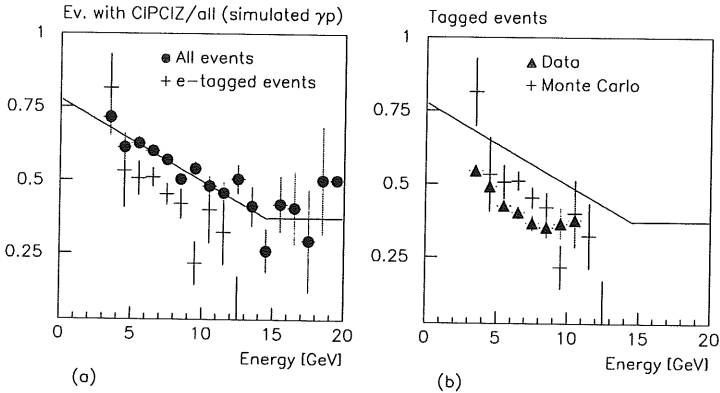


Figure 6.19: Rejection of γp events by the use of the CIPCIZ cut. Figure (a) gives the ratio of events fulfilling the cut for simulated γp events (full circles), the crosses give the same ratio for simulated tagged events. Figure (b) shows the ratio extracted from data with energy in the e -tagger (triangles) in comparison with tagged Monte Carlo events. The curve corresponds to the function given in eq. 6.2.7.

$$\epsilon_{\gamma p}^{sim}(E) = \max(A - B * E, C) \quad \text{with} \quad A = 77.6\%, \quad B = 2.8\text{GeV}^{-1} \quad \text{and} \quad C = 37\% \quad (6.2.7)$$

The last term C describes the constant high energy part which is partly determined by the fraction of photons converting already in the beam pipe. The first part is given by the percentage of clusters with a converting photon.

Figure 6.19 (b) shows the efficiency of the CIPCIZ cut for real data in comparison with the estimation of the simulated tagged events and the parametrization. As it was already observed in the ECRA distribution, the rejection power as measured with real data seems to be about 8% higher than expected by the simulation. However the energy dependence is well reproduced.

It was already observed for DIS events that the efficiency of the CIPCIZ cut is by 4% lower than in simulation, due to detector and reconstruction effects. If e.g. the energy deposit for hadrons in the BEMC is overestimated or the dead material between the tracker and the BPC is underestimated the difference between data and Monte Carlo could be explained. Therefore

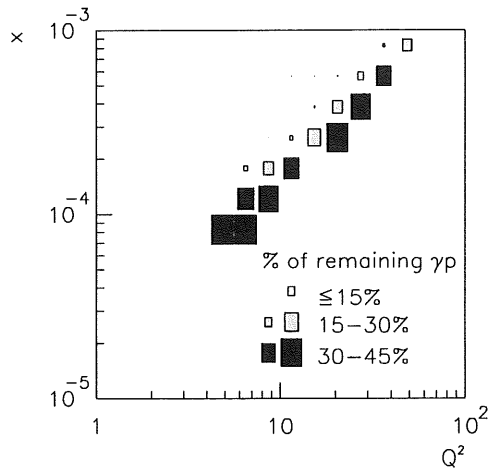


Figure 6.20: Percentage of remaining γp background after all cuts.

we take Formula 6.2.7 with a correction of -8% as an estimator for the remaining background with an absolute systematical error of 9%. The latter was given by the statistical error of the method and the difference between Monte Carlo and data.

Equation 6.2.7 then reads:

$$\epsilon_{\gamma p}^{sim}(E) = \max(69.6 - 2.8 \text{ GeV}^{-1} \times E, 29)\% \pm 9\% \quad (6.2.8)$$

The remaining fraction of photoproduction events

$$\frac{N_{\gamma p \text{ remain}}}{N_{CIPCI Z}} = \frac{\epsilon_{\gamma p} N_{\gamma p}}{N_{CIPCI Z}} \quad (6.2.9)$$

can then be estimated by making use of

$$N_{CIPCI Z} = \epsilon_{meas}(N_{DIS} + N_{\gamma p}) = \epsilon_{meas} N_{tot} \quad (6.2.10)$$

and 6.2.4. $N_{\gamma p}$ can be written as:

$$N_{\gamma p} \stackrel{6.2.4}{=} \frac{1}{\epsilon_{\gamma p}} (N_{CIPCI Z} - \epsilon_{DIS} N_{DIS}) = \frac{1}{\epsilon_{\gamma p}} (N_{CIPCI Z} - \epsilon_{DIS} (N_{tot} - N_{\gamma p})), \quad (6.2.11)$$

and therefore:

$$N_{\gamma p} = (1 - \frac{\epsilon_{DIS}}{\epsilon_{\gamma p}})^{-1} \frac{1}{\epsilon_{\gamma p}} (N_{CIPCI Z} - \epsilon_{DIS} N_{tot}). \quad (6.2.12)$$

Hence the fraction of remaining photoproduction events within the sample is obtained to:

$$\frac{\epsilon_{\gamma p} N_{\gamma p}}{N_{CIPCI Z}} = \frac{1}{1 - \frac{\epsilon_{DIS}}{\epsilon_{\gamma p}}} (1 - \epsilon_{DIS} \frac{N_{tot}}{N_{CIPCI Z}}) = \frac{1}{1 - \frac{\epsilon_{DIS}}{\epsilon_{\gamma p}}} (1 - \frac{\epsilon_{DIS}}{\epsilon_{meas}}) \quad (6.2.13)$$

Some typical values for this fraction and its error for the selected bins in x and Q^2 are given in Tables 7.2, 7.3, B.1 and B.2. As illustrated in Figure 6.20 the highest y bins contain the largest background contaminations. The background calculated in the manner described above was subtracted bin by bin.

Chapter 7

Results

7.1 Monte Carlo simulations

All Monte Carlo simulations for DIS require the proton structure function as an input, i.e. precisely what we want to measure in our MRSB [19] parametrization which described

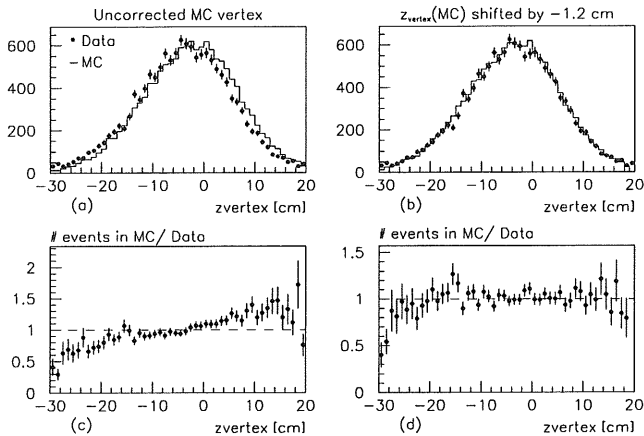


Figure 7.1: z -vertex distribution for data and Monte Carlo (MC) events (MRSB) after the final cuts. On the left side the distributions before the correction, with too many MC events on the positive z side due to a difference in the nominal vertex position between data and MC of 1.2 cm. After the correction the two distributions agree nicely (b) with the ratio of the number of events in MC and data close to one (d).

experiment. In order to deduce a systematical error induced to the analysis by a particular choice of the structure function two different theoretical model functions were used. Firstly the

cut	Efficiency %	Error %
Trigger [65]	100	2
TOF [71]	98	2
BPC	98	2
z vertex [72]	98	3
vertex tail* [73]	95	2
CIPCIZ	96	2
Total	86	5
*: correction due to events outside of the z vertex range or in the satellite bunches.		

Table 7.1: Global efficiencies with respect to Monte Carlo simulations.

well the 1992 HERA data, and secondly the MRSD⁰ [18] parametrization which doesn't describe the steep rise in F_2 towards low x . The full detector response was simulated for both choices, including some of the measured hardware inefficiencies and of course the geometrical acceptance and the response functions of the different detectors. Hence only small remaining differences between the data and the simulation are of importance for the analysis. Among these small and global, i. e. kinematically independent corrections are those from the fraction of events lost by the analysis cuts. Their efficiencies with respect to the simulation are listed in Table 7.1. Within the errors we found no dependence of the efficiencies of the cuts on the assumption of the structure function.

Only the trigger efficiency needed an additional local correction at low energies (see Section 5.1), which was applied binwise.

The quality of the simulation was checked by a comparison of the measured vertex, energy and angle distribution with the Monte Carlo (MRSH) distributions. The Monte Carlo distributions are absolutely normalized, i.e. corrected for the different luminosities (253 nb^{-1} for data and 892 nb^{-1} for Monte Carlo) and the additional inefficiencies as listed in Table 7.1. Figure 7.1(a) shows the z -vertex distribution for the MRSH Monte Carlo in comparison with the measured distribution. Obviously there is an excess of simulated events at positive z . The ratio of the number of events in Monte Carlo and in data as a function of the z position (c) of the vertex has a positive slope, again indicating that the nominal vertex position of the Monte Carlo events is shifted in positive direction with respect to the nominal vertex position in data. The Monte Carlo was simulated with a distribution of interaction vertices centering at $z=-3.6 \text{ cm}$ while in the data the center was measured at $z=-4.8 \text{ cm}$. However the shape of the distribution was simulated correctly. Such a shift of course influences the

simulated distributions, since more low angle events, which have a higher probability enter the acceptance of the detector. The restriction of the event sample to events within the acceptance of the CIP makes this analysis especially sensitive to this shift. In this sample the electrons are not fixed to an angular region, but have to pass the CIP planes within fixed limits in z , the shifted center of the vertex distributions now allow more low angle tracks to fulfill the acceptance criterion. The different z -vertex distribution for data and Monte Carlo was accounted for by requiring for the simulated events that the electron track given by the line vertex-BPC crosses the inner CIP plane at z values larger than $-110+1.2$ cm. The vertex distribution for accepted events with this correction applied and the Monte Carlo vertex shifted by -1.2 cm are shown in Figures 7.1(b). The ratio between the two distributions (Figure 7.1(d)) is close to one with no visible slope, indicating that the data is well described.

For the following analysis we always applied the above correction procedure for the

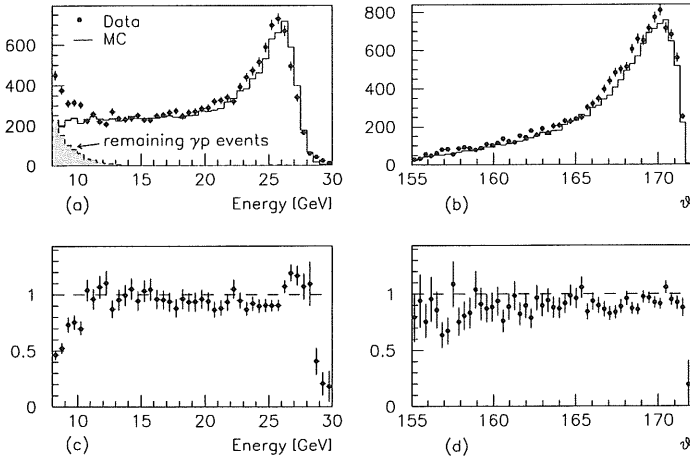


Figure 7.2: Energy (a) and angle (b) distribution for data (before the statistical background subtraction) and Monte Carlo (MC) simulated events. The ratio of the two distributions (c) and (d) show generally nice agreement except for very low energies, where there is still remaining background in the data sample and at very high energies where the sensitivity to the normalization of the energy scale is largest. The amount of remaining background, as estimated with the CIPCIZ cut is shown in the hatched histogram.

simulated events first. Figures 7.2 (a) and (b) show the energy and angle distribution again comparing data (before the statistical background subtraction) and Monte Carlo events with absolute normalization. The ratio of the number of simulated events and data ((c) and (d)) shows that the two distributions generally nicely agree except at low energies because of background contamination and the very high energy part which is very sensitive to the

energy calibration. The angular distribution is well described by the simulation. Towards high angles the background contamination becomes visible again.

7.2 Binning

The distribution of the events after all cuts is shown in Figure 7.3 in the $\log(x)$ - $\log(Q^2)$ plane. Most of the events are located at low x and low Q^2 as expected from the $1/Q^4$ dependence of the cross section. The grid indicates the binning chosen for the analysis of the proton

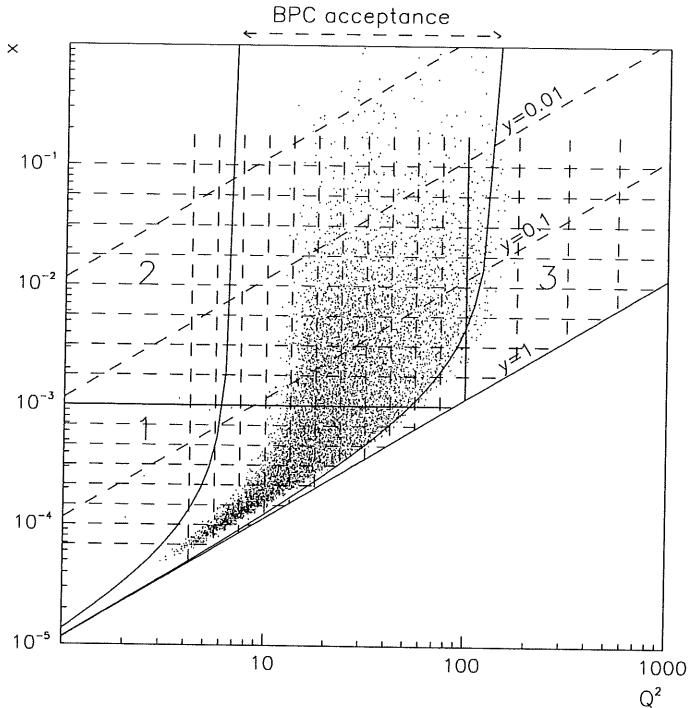


Figure 7.3: Event distribution in the $x - Q^2$ plane. The binning which was used for the analysis is overlaid. The plane is divided into three areas (1, 2 and 3) with different binnings.

structure function. The bin size was determined by the requirement of a suitable number of events in most of the bins. The $x - Q^2$ plane is divided in 8 bins per decade and 6 bins per decade in x , both divisions equidistant in $\log(Q^2)$ and $\log(x)$ respectively. For x values larger than 0.01 and Q^2 larger than 100 GeV^2 the number of events is smaller, therefore we enlarge the bin size to 4 bins per decade. The choice of bins is still dominated by statistical

considerations and exceeds the kinematical resolutions.

7.3 Acceptance

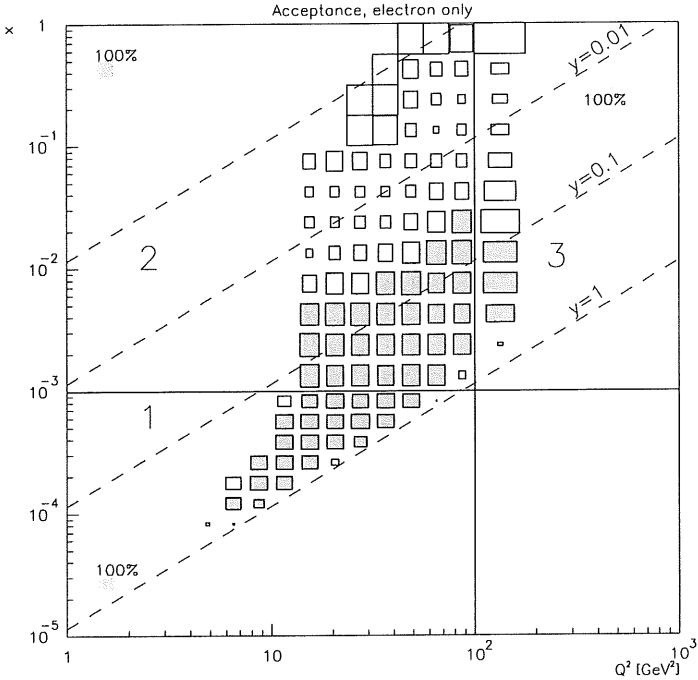


Figure 7.4: Acceptance in the binning chosen for this analysis for the electron only method. The size of the boxes gives a measure for the acceptance. Three test boxes with 100% acceptance for the three different binnings (1, 2 and 3) are drawn in the corners. The hatched bins fulfill the selection criteria of less than 50% migration and more than 45% of the events staying in the bin they were produced in.

The bins in x and Q^2 which can be used in the analysis have to be determined by acceptance studies. It was shown in Chapter 3 that the two methods for determining the kinematical variables access different kinematical regions. For a more quantitative definition of the bins which can be used for the analysis we define three new quantities:

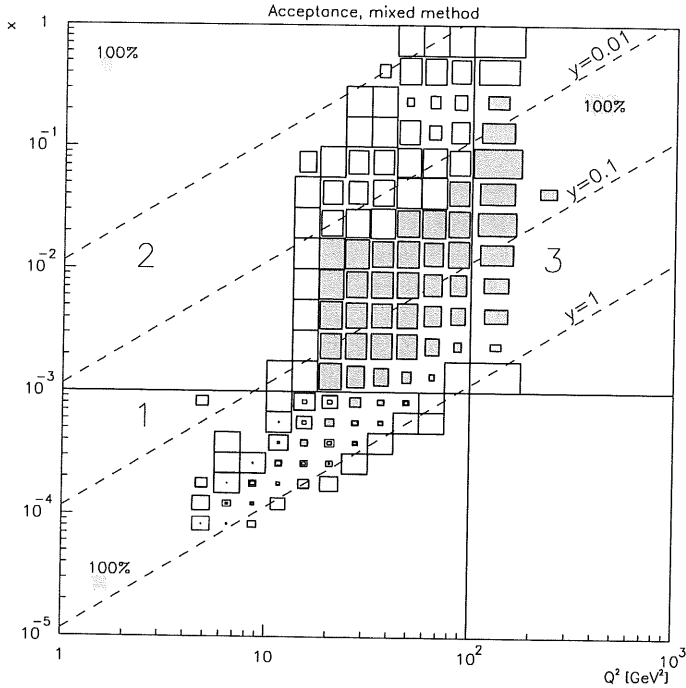


Figure 7.5: Acceptance in the x - Q^2 plane for the mixed method which cannot be used at high y . The hatched boxes in the corners give a measure of 100% acceptance for the three binnings (1, 2 and 3). Bins with a migration of less than 50% and more than 30% of the generated events staying in the bin are drawn in hatched style.

- Acceptance A : Number of events reconstructed in a certain bin (N_{rec}) divided by the number of generated events (N_{gen}):

$$A = \frac{N_{rec}(\Delta x, \Delta Q^2)}{N_{gen}(\Delta x, \Delta Q^2)}$$

- Smeared acceptance A_{smeas} : the pure acceptance A is not a good property to decide whether the bin can be used since the acceptance can be very high even if no or very few events generated in the bin are reconstructed in that bin. A better quantity is therefore the smeared acceptance, being defined as the difference of the events migrating into the bin (N_{in}) and those migrating out of the bin N_{out} divided by the number of reconstructed events:

$$A_{smeas} = \frac{|N_{in}(\Delta x, \Delta Q^2) - N_{out}(\Delta x, \Delta Q^2)|}{N_{rec}(\Delta x, \Delta Q^2)}$$

- Stable events A_{stable} : A_{stable} gives the ratio of events which remained in their original bin (N_{stay}) over all events reconstructed in the bin.

$$A_{stable} = \frac{N_{stay}(\Delta x, \Delta Q^2)}{N_{rec}(\Delta x, \Delta Q^2)}.$$

We finally accepted bins with a migration A_{smear} of less than 50% and with A_{stable} larger than 45% for the electron method and larger than 30% for the mixed method. The acceptance, as calculated with a simulation using the MRSH parametrization for the structure function, for each bin is illustrated in Figures 7.4 and 7.5 for the two methods with the size of the boxes being a measure for the acceptance A . The three hatched bins in the corners give a reference for a 100% acceptance for the three different bin definitions. Only bins with an acceptance A of less than 150% are shown. The hatched area indicates the bins which fulfilled the two quality criterion defined above. The electron method accesses the high y region with an acceptance of about 100% whereas the mixed method is useable in the intermediate y region. The acceptance for the mixed method is very bad at very high y as a consequence of the hadrons being lost in the backward region. The average acceptance in the hatched area is about 120%, because the events at high y are shifted to lower values.

7.4 Measurement of F_2

In the experiment we measure the differential cross section in bins $\Delta x \cdot \Delta Q^2$:

$$\frac{\Delta^2 \sigma}{\Delta x \Delta Q^2} = \frac{N}{A \epsilon L} \quad (7.4.1)$$

with

- N Number of DIS events after subtraction of the remaining background.
- A Acceptance of the detector, $A = N_{rec}/N_{gen}$
- ϵ Efficiency of the cuts and the selection (since in the end a comparison between Monte Carlo events and real data is made, only efficiencies which differ from the simulation enter here).
- L Total integrated luminosity used for the analysis, $L=253 \text{ nb}^{-1}$

It was shown in Chapter 2 that the differential cross section can be written in terms of the structure function F_2 :

$$\frac{d^2 \sigma}{dx dQ^2} = \kappa(R) \cdot F_2(x, Q^2) \cdot (1 + \delta) \quad \text{with} \quad \kappa(R) = \frac{2\pi \alpha^2}{Q^4 x} (2(1-y) + \frac{y^2}{1+R}) \quad (7.4.2)$$

where

$1+\delta$ gives the corrections to the pure photon exchange such as radiative corrections or contributions of the weak interaction.

The latter can safely be neglected for this analysis.

R gives the ratio between the longitudinal and the total cross section $R=F_L/F_2$. R is not measured yet in the kinematical range of HERA, therefore the value predicted by QCD calculations was taken.

By combining 7.4.1 and 7.4.2 we get:

$$F_2 \simeq \frac{1}{\kappa(R)} \frac{\Delta^2 \sigma}{\Delta x \Delta Q^2} \cdot C_{RC} \cdot C_{BC} \quad (7.4.3)$$

where $C_{RC}=1/(1+\delta)$ gives the radiative corrections and C_{BC} the corrections which have to be applied due to the finite bin size. With σ_0 denoting the Born cross section and σ the cross section with radiative corrections, the two corrections terms can be written as:

$$C_{BC} = \frac{\sigma_0(x_c, Q_c^2)}{\int_{bin} \sigma_0(x, Q^2) dx dQ^2} \quad \text{and} \quad C_{RC} = \frac{\int_{bin} \sigma_0(x, Q^2) dx dQ^2}{\int_{bin} \sigma(x, Q^2) dx dQ^2} \quad (7.4.4)$$

and the structure function becomes:

$$\begin{aligned} F_2 &\simeq \frac{1}{\kappa(R)} \frac{N}{A \epsilon L} \cdot \frac{\sigma_0(x - c, Q_c^2)}{\int_{bin} \sigma_0 dx dQ^2(x, Q^2)} \cdot \frac{\int_{bin} \sigma_0(x, Q^2) dx dQ^2}{\int_{bin} \sigma(x, Q^2) dx dQ^2} \\ &= \frac{1}{\kappa(R)} \frac{N}{A \epsilon L} \cdot \frac{\sigma_0(x_c, Q_c^2)}{\int_{bin} \sigma(x, Q^2) dx dQ^2} \\ &= \frac{N}{A \epsilon L} \cdot \frac{F_2^{th}(x_c, Q_c^2)}{\int_{bin} \sigma(x, Q^2) dx dQ^2} \end{aligned} \quad (7.4.5)$$

Herein $F_2^{th}(x_c, Q_c^2)$ is the parametrisation of the structure function which was used in the simulation at the center of the bin. The remaining integral in the above formula can be determined in Monte Carlo if all higher order radiative corrections are correctly included into the simulation.

$$\int_{bin} \sigma dx dQ^2 = \frac{N_{gen}}{L_{MC}} \quad (7.4.6)$$

with N_{gen} the numbers of generated events per bin with the luminosity L_{MC} .

Hence the proton structure function is then simply obtained by counting the events in data and in Monte Carlo:

$$F_2(x_c, Q_c^2) \simeq \frac{N}{N_{rec}/N_{gen} \epsilon L} \frac{L_{MC}}{N_{gen}} F_2^{th} = \frac{1}{\epsilon} \frac{N}{N_{rec}} \frac{L_{MC}}{L} F_2^{th} \quad (7.4.7)$$

7.5 Error considerations

In most of the bins the error is dominated by systematic effects which have to be determined carefully. All the efficiencies with respect to the simulation were determined from data. The

global bin independent efficiencies were listed in Table 7.1. The corresponding uncertainties enter into the overall systematical error. In evaluating the bin dependent systematical errors we adopt the procedure, that we shift a measured input quantity by its maximum, one-standard deviation uncertainty and take the corresponding change in F_2 as the bin dependent systematical error. A table with the systematical errors for each bin can be found in Appendix B. The systematical bin dependent errors include:

- Uncertainty in the energy scale of the BEMC. Using data with the electron energy shifted by the full uncertainty of 1.7% we found changes of F_2 varying between 1 and 10% for the electron method. For the mixed method the changes were generally smaller than 10%.
- For the angular uncertainty of 1 mrad, corrections between 1 and 8% were obtained.
- Structure function dependence: The final F_2 was determined using the MRSB parametrization. In order to get the structure function dependence, we calculated F_2 for each bin with the MRSD0 parametrization which is much flatter, and included half of the difference into the error. The effect of the unknown structure function is largest at low x and of the order of 1 to 7%.
- Radiative corrections (expression for C_{RC} in equation 7.4.4): Within 2-3% statistical accuracy the Monte Carlo (DJANGO [74]) results agree with analytical calculations including higher order corrections. Hence the systematical error is limited to less than 3% [75].
- Bin size corrections (expression for C_{BC} in equation 7.4.4): Though the bin center correction does not explicitly show up in Formula 7.4.7 it enters in the systematical error, because the bin size corrections were calculated without radiative corrections. The error is negligible at high x and 4% at very low x .
- Background subtraction: Both beam induced and photoproduction background were subtracted statistically in bins in x and Q^2 . The error for the photoproduction background was determined by the 9% uncertainty in the function which describes the energy dependence of the CIPCIZ cut on photoproduction events (6.2.8). The error is everywhere below 10% and is below 1% for y less than 0.6. The error of the beam induced background was taken as half the number of the subtracted events divided by the total number of events and is below 5%.
- 7% uncertainty in the hadronic energy scale: Affects the mixed method with an error of at most 6%. It was studied using Monte Carlo simulations.

- Fragmentation models: Again only for the mixed method with an additional systematical error of 3 to 10%. It was tested [75] using two different fragmentation models, by comparing the results obtained with the HERWIG generator [76] with MEPS (LEPTO 6.1 [77] and JETSET 7.3 [78]).
- Uncertainty at low energies: An additional error of 4% (5%) for energies below 15 GeV (10 GeV) was included to allow for a possible energy dependence of the BPC cut (see Section 6.2.3) and to consider the larger errors on the trigger efficiency.
- Global scale: The total integrated luminosity is only known within 5% [79] This global normalization error is not included in the error bars.
- Global efficiencies: The 5% error of the global efficiencies is included in the systematics. To allow for a comparison between different analyses the error of the global efficiencies is not included in the global normalization error.

7.6 Proton structure function F_2

The proton structure function F_2 as a function of x is shown for eight different bins in Q^2 in Figure 7.6. The error bars correspond to statistical and systematical errors added in quadrature, the inner error bars are statistical errors only. Only electron variables were used for the determination of the points with full circles, whereas the results obtained with the mixed method, which uses the hadronic measurement for the determination of y_h , are plotted with open circles. The two methods agree very well in the overlapping region. The electron method is restricted to the low x region and the mixed method complements the measurement towards higher x . F_2 rises with decreasing x . Since the structure function in this region is essentially determined by the sea quark density this rise corresponds to a rise of the gluon density towards low x .

The results are compared with the H1 structure function results presented on the Glasgow conference [80]. The two methods are compared individually (Figure 7.7 for the electron and Figure 7.8 for the mixed method). A detailed comparison can be found in Appendix C in Tables C.1 and C.2. The H1 analysis used the electron only method with an energy cut at 10.6 GeV as well as the so called Σ method [42], [30] (energy larger than 8 GeV) which is similar to the mixed method at low y but is less sensitive to initial state radiation. The kinematical variables x , y and Q^2 are determined by the three quantities energy and angle of the electron and the sum of $(E_h - p_{zh})$ of all hadrons. The background was rejected by a cut on the lateral cluster size in the BEMC and additionally a cut on the total E_{minPz} for the Σ analysis. The remaining background was subtracted statistically. The points shown in the

figures correspond to the analysis with the lowest error. The agreement with the H1 results is good in the whole kinematical region, which essentially shows that the different methods for the background determination are understood in the kinematical region they are applied. Figure 7.7 shows, that the method used in this analysis for the background subtraction allows to access generally one more bin at very low x . $Q^2=12 \text{ GeV}^2$ is the only bin with less data points than the standard H1 analysis, because of the angular acceptance of the CIPCIZ cut. It has to be mentioned that the very low x points rely on a good description of the radiative corrections in the Monte Carlo since no explicit cut in y was applied.

The last two figures (7.9 and 7.10) show the points of this analysis together with four different parametrizations (MRSH [19], MRSD^{0'} [18], CTEQ2 [20], and GRV [21]). Obviously, the MRSD^{0'} which starts with a constant parton density function at $Q^2=4 \text{ GeV}^2$ fails to describe the data. The error of the measurement doesn't allow to distinguish between the three other parametrizations.

The results are summarized in Tables 7.2 and 7.3, with the statistical and systematical as well as the fraction of subtracted background events separately. The values marked with ** are the additional points to the H1 analysis.

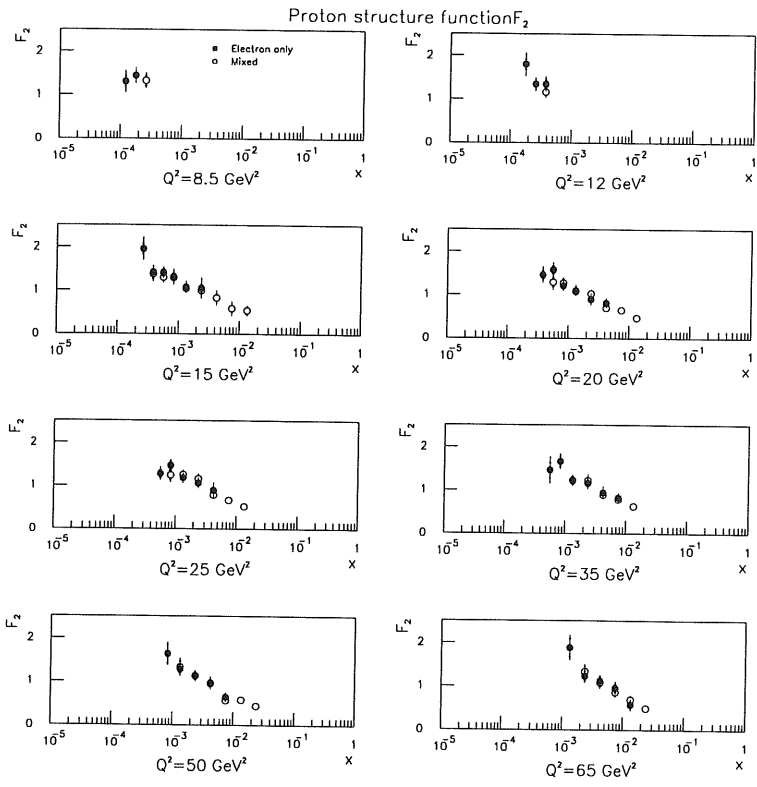


Figure 7.6: Proton structure function F_2 as a function of x in eight bins of Q^2 . Open points (full points) are deduced with the mixed (electron) method. The error bars correspond to statistical and systematical error added in quadrature, the inner error bars to the statistical error only.

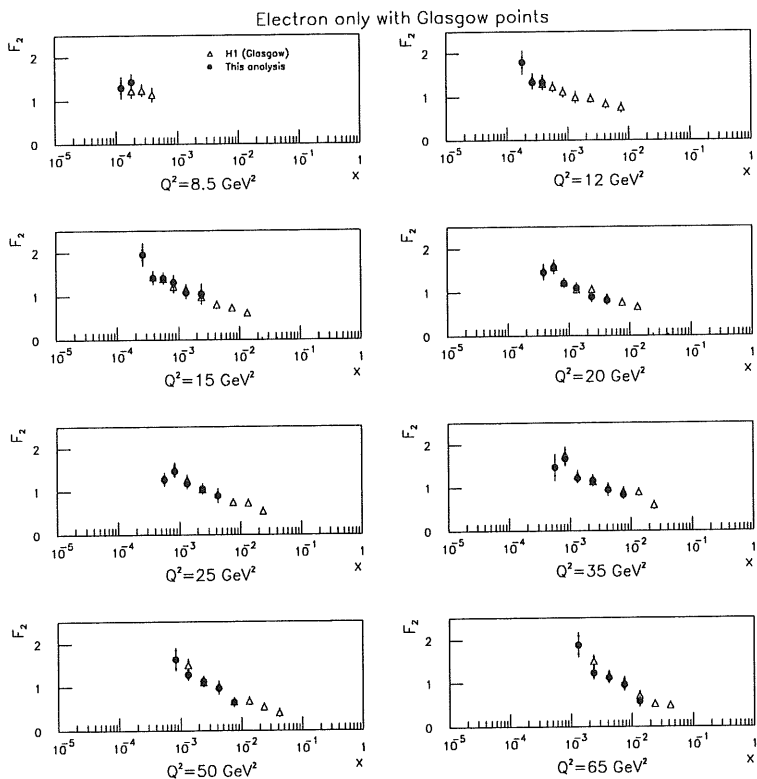


Figure 7.7: Proton structure function F_2 analysed with the electron method. The results of this analysis are compared with the H1 results presented in Glasgow.

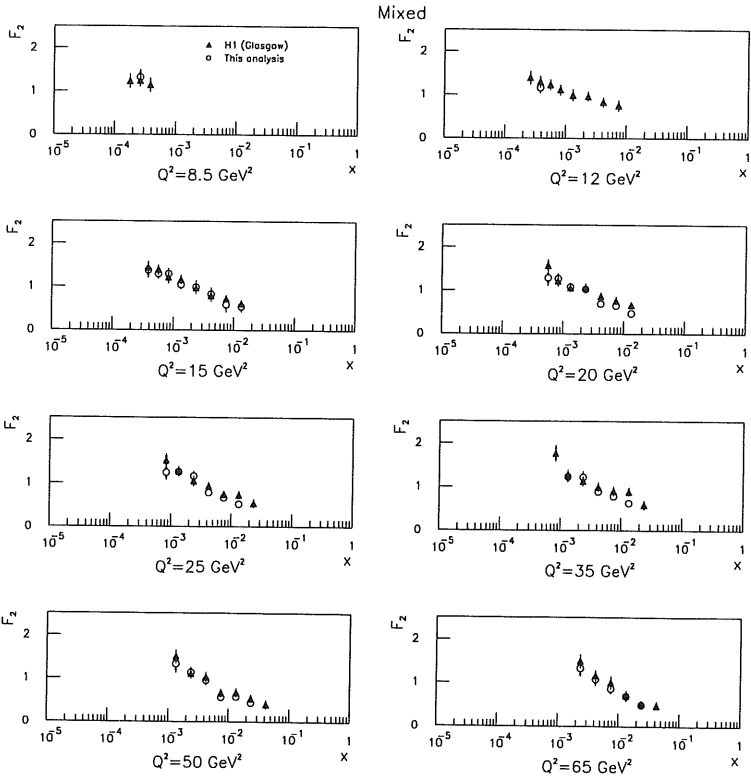


Figure 7.8: Proton structure function F_2 analysed with the mixed method. The results of this analysis are compared with the H1 results presented in Glasgow.

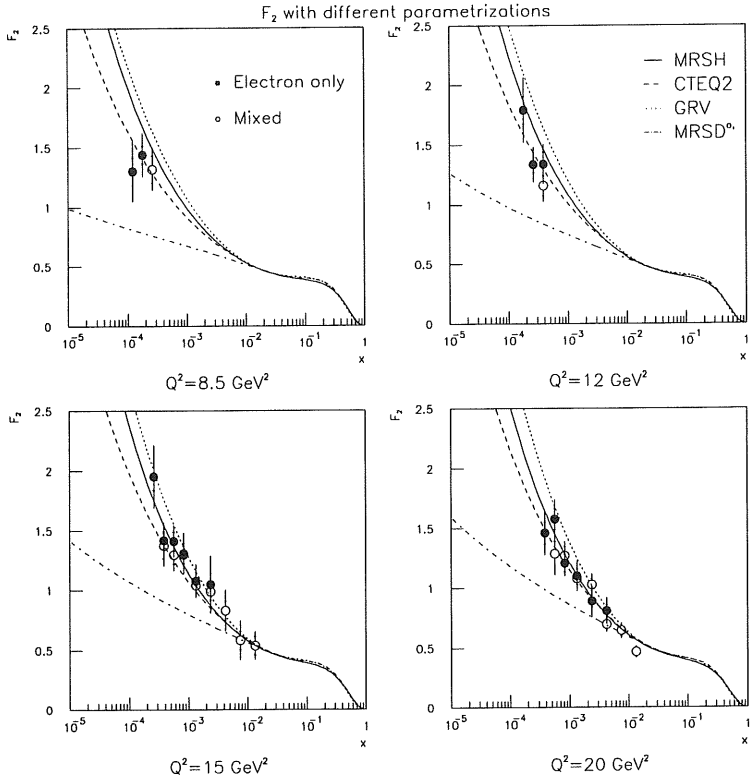


Figure 7.9: Proton structure function F_2 with four different parametrizations for the four lowest Q^2 bins.

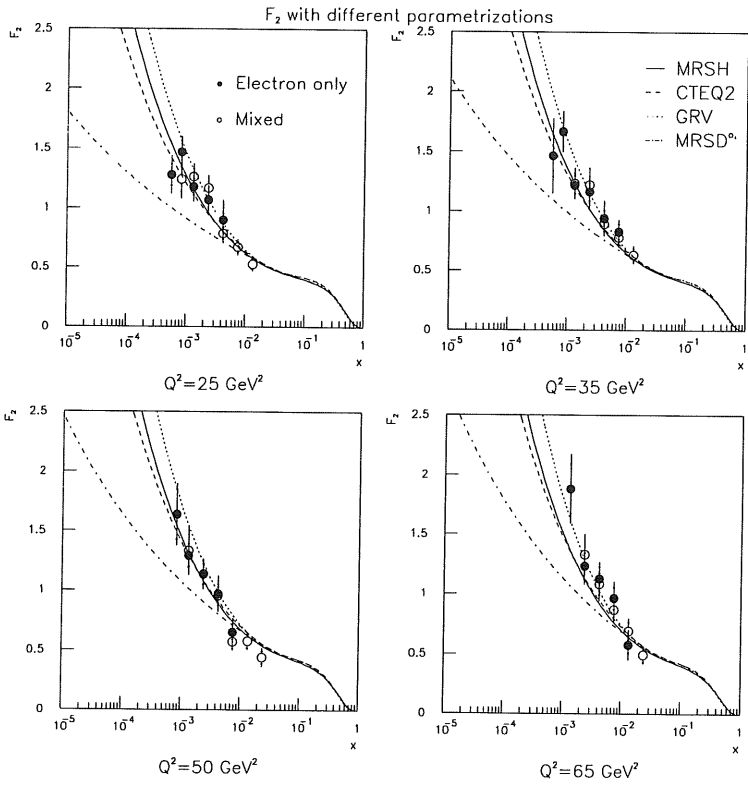


Figure 7.10: Proton structure function F_2 with four different parametrizations for the four highest Q^2 bins.

Q^2 GeV ²	x	y	Electron only			Mixed					
			F_2	Error stat \pm syst	BG*%	F_2	Error stat \pm syst	BG*			
8.5	0.00012**	0.8	1.30	0.12 \pm 0.22	40 (16)	1.32	0.11 \pm 0.14	21			
	0.00018	0.5	1.44	0.07 \pm 0.17	20 (4)						
	0.00026	0.4									
12	0.00018**	0.75	1.79	0.12 \pm 0.25	31 (2)	1.16	0.08 \pm 0.10	9			
	0.00026	0.52	1.33	0.07 \pm 0.13	6						
	0.00038	0.36	1.34	0.10 \pm 0.13							
15	0.00026**	0.65	1.98	0.12 \pm 0.24	26 (4)	1.37	0.11 \pm 0.13	14			
	0.00038	0.45	1.42	0.09 \pm 0.13	1						
	0.00056	0.30	1.41	0.09 \pm 0.11					1.30	0.08 \pm 0.11	6
	0.00083	0.20	1.31	0.07 \pm 0.15					1.30	0.07 \pm 0.10	3
	0.00133	0.13	1.08	0.06 \pm 0.12					1.04	0.06 \pm 0.08	2
	0.00237	0.07	1.05	0.09 \pm 0.22					0.99	0.07 \pm 0.15	2
	0.00421	0.04							0.83	0.08 \pm 0.15	2
	0.00750	0.02							0.58	0.08 \pm 0.15	1
0.01334	0.01				0.54	0.08 \pm 0.09	3				
20	0.00038**	0.59	1.46	0.09 \pm 0.16	18	1.29	0.10 \pm 0.14	10			
	0.00056	0.40	1.58	0.09 \pm 0.14							
	0.00083	0.27	1.21	0.07 \pm 0.08					1.27	0.08 \pm 0.09	4
	0.00133	0.17	1.10	0.06 \pm 0.11					1.08	0.05 \pm 0.08	1
	0.00237	0.10	0.89	0.05 \pm 0.12					1.02	0.05 \pm 0.08	1
	0.00421	0.05	0.81	0.05 \pm 0.10					0.70	0.04 \pm 0.05	
	0.00750	0.03							0.64	0.05 \pm 0.05	
0.01334	0.02				0.47	0.04 \pm 0.03					
BG*: fraction of events subtracted due to photoproduction (beam induced) background ** additional to standard H1 analysis											

Table 7.2: Proton structure function F_2 .

Q^2 GeV ²	x	y	Electron only			Mixed		
			F_2	Error stat \pm syst	BG*%	F_2	Error stat \pm syst	BG*
25	0.00056**	0.60	1.28	0.09 \pm 0.14	39 (5)			
	0.00083	0.41	1.47	0.10 \pm 0.09	11 (1)	1.24	0.10 \pm 0.12	7
	0.00133	0.25	1.12	0.07 \pm 0.10		1.26	0.07 \pm 0.09	3
	0.00237	0.14	1.11	0.06 \pm 0.10		1.17	0.06 \pm 0.09	
	0.00421	0.08	0.90	0.06 \pm 0.16		0.80	0.05 \pm 0.07	1
	0.00750	0.05				0.67	0.05 \pm 0.05	1
	0.01334	0.03				0.53	0.04 \pm 0.04	
35	0.00056**	0.80	1.46	0.17 \pm 0.26	31			
	0.00083	0.54	1.67	0.12 \pm 0.12	4			
	0.00133	0.33	1.22	0.08 \pm 0.08		1.23	0.09 \pm 0.16	5
	0.00237	0.19	1.17	0.08 \pm 0.12		1.22	0.07 \pm 0.09	2
	0.00421	0.11	0.94	0.07 \pm 0.13		0.89	0.06 \pm 0.07	
	0.00750	0.06	0.83	0.06 \pm 0.08		0.78	0.06 \pm 0.05	
	0.01334	0.03				0.63	0.05 \pm 0.04	
50	0.00083**	0.68	1.64	0.21 \pm 0.15	17			
	0.00133	0.42	1.29	0.10 \pm 0.10		1.34	0.13 \pm 0.16	5
	0.00237	0.24	1.14	0.09 \pm 0.09		1.14	0.08 \pm 0.09	1
	0.00421	0.13	0.97	0.08 \pm 0.13		0.95	0.07 \pm 0.07	
	0.00750	0.08	0.65	0.06 \pm 0.10		0.57	0.05 \pm 0.05	
	0.01334	0.04				0.58	0.06 \pm 0.04	
	0.02372	0.02				0.44	0.05 \pm 0.06	
65	0.00133**	0.51	1.88	0.21 \pm 0.20	2 (6)			
	0.00237	0.29	1.23	0.11 \pm 0.11		1.33	0.13 \pm 0.12	
	0.00421	0.16	1.11	0.10 \pm 0.09		1.08	0.09 \pm 0.11	
	0.00750	0.09	0.96	0.09 \pm 0.11		0.87	0.08 \pm 0.07	
	0.01334	0.05	0.58	0.07 \pm 0.11		0.69	0.07 \pm 0.08	
	0.02372	0.03				0.49	0.06 \pm 0.04	

Table 7.3: Proton structure function F_2 , cont'd.

Chapter 8

Summary

The analysis presented herein describes the measurement of the proton structure function F_2 . It uses data measured with the H1 detector at HERA in the 1993 running period, with an integrated luminosity of 253 nb^{-1} . It only considers events with the electron scattered at low angles with respect to their initial direction and therefore accesses the kinematical region of low and intermediate Q^2 and low x .

The detector measures both, the scattered electron and the hadronic system, which allows to use different methods for the determination of the kinematics. The advantages of two methods - one relying on the electron measurement only, the other one using a combined measurement- as well as the kinematical regions accessible with either method were discussed. The determination of F_2 with both methods allows to cross-check the results and the errors in the overlapping region. The electron method was used for the measurement in the low x region, whereas the mixed method completes the measurement towards high x .

The description of the H1 detector emphasizes the components important for this analysis, being the innermost tracking chambers and the backward part which is used for the detection of the scattered electron. The chamber efficiencies, as well as the energy calibration constants were determined from data.

The extension of the measurement of F_2 to very low x mainly depends on the possibilities to control the background at low energies. The studies in this analysis show that this is possible by a cut using tracking informations. Though angular acceptance is limited, this method proved to be very powerful, rejecting 40-60% of the photoproduction events and allowing an estimate of the remaining background from data with an efficiency of 95.5% for deep inelastic events. The remaining background was subtracted statistically with a systematical error determined to be 10% at most.

The extraction of the proton structure function from data was explained in detail, including acceptance studies for the two methods and a discussion of possible systematical errors. The resulting structure function F_2 as a function of x is shown in eight bins of Q^2 . The two methods agree excellently within the errors and compare well with the standard H1 analysis

of the 1993 data, which uses a different treatment for the photoproduction background and a higher energy cut. The rising of the structure function with decreasing x indicates a fast growth of the gluon and therefore the sea quark density in the proton. For constant values of x , F_2 is slowly rising with Q^2 as could be expected from perturbative QCD.

The new method of background subtraction allows to access one additional point at low x though with a large statistical and systematical error. Besides higher statistics, a reduction of the error on the very low x points requires a better understanding of the detector properties at low energies, such as the energy cluster reconstruction and energy resolution as well as trigger efficiencies. However it was shown that the determination of the remaining background is possible from data. An improvement in the systematical error of the latter would be possible by using all photoproduction events instead of the subsample of tagged events.

Appendix A

ϑ resolution

The angle ϑ is defined by a point in R , z and the vertex (R_v, z_v) :

$$\vartheta = \arctan \frac{\Delta R}{\Delta z}. \quad (\text{A.0.1})$$

For the determination of the ϑ resolution we will neglect the small deviation of the radial vertex from zero and its small error:

$$\begin{aligned} \vartheta &= \arctan \frac{R}{z - z_v} \quad \text{and} \\ \sigma_\vartheta &= \sqrt{\left(\frac{\partial \vartheta}{\partial R}\right)^2 \delta R^2 + \left(\frac{\partial \vartheta}{\partial z}\right)^2 \delta z^2 + \left(\frac{\partial \vartheta}{\partial z_v}\right)^2 \delta z_v^2} \\ &= \frac{1}{\left(1 + \frac{R}{z - z_v}\right)^2} \cdot \sqrt{\frac{1}{(z - z_v)^2} \delta R^2 + \left(\frac{R}{(z - z_v)^2}\right)^2 (\delta z^2 + \delta z_v^2)} \end{aligned} \quad (\text{A.0.2})$$

For the determination of the ϑ resolution we used three different angles which measure the angle in the backward region rather accurately. The angle with the best accuracy is defined by a point in the BPC (R, z) and the vertex:

$$\vartheta_{BPCV} = \arctan \frac{R}{z - z_v}. \quad (\text{A.0.3})$$

The other two angles were determined by the vertex and either a hit in the CIP (R_{CIP}, z_{CIP}) or the cluster center of gravity (R_{Clu}, z_{Clu}) respectively:

$$\vartheta_{CIPV} = \arctan \frac{R_{CIP}}{z_{CIP} - z_v} \quad \text{and} \quad \vartheta_{CLUV} = \arctan \frac{R_{Clu}}{z_{Clu} - z_v} \quad (\text{A.0.4})$$

With δz and δR denoting the resolution in R and z of the measurement, the angular resolution can be written as:

$$\sigma_{BPCV}^2 = \frac{1}{\left(1 + \left(\frac{R}{z - z_v}\right)^2\right)^2} \left(\frac{1}{(z - z_v)^2} \delta R^2 + \left(\frac{R}{(z - z_v)^2}\right)^2 \delta z^2 \right)$$

$$\sigma_{CIPV}^2 = \frac{1}{\left(1 + \left(\frac{R_{CIP}}{z_{CIP} - z_v}\right)^2\right)^2} \left(\frac{R_{CIP}}{z_{CIP} - z_v}\right)^2 (\delta z_v^2 + \delta z_{CIP}^2)$$

$$\sigma_{CluV}^2 = \frac{1}{\left(1 + \left(\frac{R_{Clu}}{z_{Clu} - z_v}\right)^2\right)^2} \left(\frac{1}{(z_{Clu} - z_v)^2} \delta R_{Clu}^2 + \left(\frac{R_{Clu}}{z_{Clu} - z_v}\right)^2 (\delta z_v^2 + \delta z_{Clu}^2)\right).$$

(A.0.5)

For the determination of the individual resolutions we measured the difference between two of the three angles. The three distributions are shown in Figure A.1, the narrowest distribution is given by ϑ measured by CIP and BPC. The width of the distribution of the

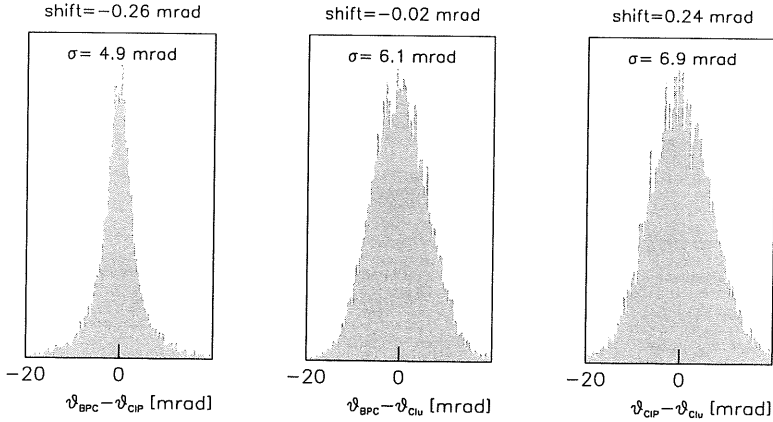


Figure A.1: Difference between three different angles in the backward direction (data).

difference between two angles (σ_{Diff}) is now given by:

$$\begin{aligned} \sigma_{Diff}^2 &= \sigma_{\vartheta_1 - \vartheta_2}^2 \\ &= \left(\frac{\partial \vartheta_1}{\partial R_1} \cdot \delta R_1\right)^2 + \left(\frac{\partial \vartheta_2}{\partial R_2} \cdot \delta R_2\right)^2 + \left(\frac{\partial \vartheta_1}{\partial z_1} \cdot \delta z_1\right)^2 + \left(\frac{\partial \vartheta_2}{\partial z_2} \cdot \delta z_2\right)^2 + \left(\left(\frac{\partial \vartheta_1}{\partial z_v} - \frac{\partial \vartheta_1}{\partial z_v}\right) \cdot \delta z_v\right)^2 \\ &= \sigma_{\vartheta_1}^2 + \sigma_{\vartheta_2}^2 - 2 \cdot \frac{\partial \vartheta_1}{\partial z_v} \cdot \frac{\partial \vartheta_2}{\partial z_v} \delta z_v^2 \end{aligned}$$

(A.0.6)

with

$$\frac{\partial \vartheta_1}{\partial z_v} \cdot \frac{\partial \vartheta_2}{\partial z_v} = \frac{1}{\left(1 + \left(\frac{R_1}{z_1 - z_v}\right)^2\right) \left(1 + \left(\frac{R_2}{z_2 - z_v}\right)^2\right)} \cdot \frac{R_1}{(z_1 - z_v)^2} \cdot \frac{R_2}{(z_2 - z_v)^2} \simeq \frac{1}{\left(1 + \left(\frac{R}{\Delta z}\right)^2\right)^2} \cdot \frac{R^4}{\Delta z^4 R_1 R_2},$$

for only small differences between the two angles. Using the above formula we get for the width of the above distributions of the difference between two angles:

$$\begin{aligned}\sigma_{\vartheta_{BPC}-\vartheta_{CIP}}^2 &= \Delta_{BPCCIP}^2 = \sigma_{BPC}^2 + \sigma_{CIP}^2 - \frac{2}{\left(1 + \left(\frac{R}{\Delta z}\right)^2\right)^2} \cdot \frac{R^4}{\Delta z^4} \frac{1}{RR_{CIP}} \delta z_v^2 \\ \sigma_{\vartheta_{BPC}-\vartheta_{Clu}}^2 &= \Delta_{BPCClu}^2 = \sigma_{BPC}^2 + \sigma_{Clu}^2 - \frac{2}{\left(1 + \left(\frac{R}{\Delta z}\right)^2\right)^2} \cdot \frac{R^4}{\Delta z^4} \frac{1}{RR_{Clu}} \delta z_v^2 \\ \sigma_{\vartheta_{Clu}-\vartheta_{CIP}}^2 &= \Delta_{CluCIP}^2 = \sigma_{Clu}^2 + \sigma_{CIP}^2 - \frac{2}{\left(1 + \left(\frac{R}{\Delta z}\right)^2\right)^2} \cdot \frac{R^4}{\Delta z^4} \frac{1}{R_{CIP}R_{CIP}} \delta z_v^2 \quad (A.0.7)\end{aligned}$$

A combination of the width of the three distributions allows to determine the individual angular resolutions plus a correction term which depends on the unknown vertex resolution:

$$\begin{aligned}\sigma_{BPC}^2 &= \frac{1}{2}(\Delta_{BPCCIP}^2 + \Delta_{BPCClu}^2 - \Delta_{CluCIP}^2) + \frac{1}{\left(1 + \frac{R^2}{z^2}\right)^2} \frac{R^4}{z^4} \frac{1}{R^2} \delta z_v^2 \\ &= \sigma_{BPC}^{2*} + C(R)\delta z_v^2 \\ \sigma_{Clu}^2 &= \frac{1}{2}(\Delta_{BPCClu}^2 + \Delta_{CIPClu}^2 - \Delta_{BPCCIP}^2) + \frac{1}{\left(1 + \frac{R^2}{z^2}\right)^2} \frac{R^4}{z^4} \frac{1}{R^2} \delta z_v^2 \\ &= \sigma_{Clu}^{2*} + C(R)\delta z_v^2 \\ \sigma_{CIP}^2 &= \frac{1}{2}(\Delta_{BPCCIP}^2 + \Delta_{CIPClu}^2 - \Delta_{BPCClu}^2) + \frac{1}{\left(1 + \frac{R^2}{z^2}\right)^2} \frac{R^4}{z^4} \frac{2R - R_{CIP}}{R^2 R_{CIP}} \delta z_v^2 \\ &= \sigma_{CIP}^{2*} + C(R) \frac{R - R_{CIP}}{R_{CIP}} \delta z_v^2 \quad (A.0.8)\end{aligned}$$

Since the ϑ_{CIP} depends only on the resolution in z it strongly varies with the radius. It is very small at small radii, even smaller than the ϑ_{BPCV} resolution but then rises towards large radii. This dependence was used to determine the z -vertex resolution.

The resolutions not corrected for the vertex term are listed below for different radii:

R [cm]	σ_{BPC}^* [mrad]	σ_{CIP}^* [mrad]	σ_{Clu}^* [mrad]
22	2.1±0.6	0.6±2.6	5.4±0.3
27	2.1±0.6	2.2±0.6	5.0±0.3
30	1.8±0.1	3.6±0.3	5.2±0.1
37	1.9±1.1	5.2±0.4	5.2±0.4
55	3.1±3.4	8.8±1.3	5.5±2.1
ϑ resolutions.			

Since the z resolution of the CIP cannot be smaller than the resolution of a pad, we fitted the function

$$\sigma_{CIP}^{2*}(R) = \frac{1}{\left(1 + \frac{R^2}{z^2}\right)^2} \frac{R^4}{z^4 R_{CIP}^2} \left(\delta z^2 + \delta z_v^2 \left(1 - \frac{R_{CIP}}{2R - R_{CIP}} R^2\right) \right)$$

to the data with dz_{CIP} restricted to values larger than 1.2 cm, which corresponds to the minimal z resolution of the CIP. We found $dz_{CIP}=1.5$ cm and a vertex resolution of $dz_v=0.9 \pm 0.2$ cm. The error was determined by varying dz_{CIP} between 1.2 and 1.8 cm.

This gives the final resolutions:

average BPC [mrad]	only one BPC hit[mrad]	CIP [mrad]	Cluster [mrad]
2.5 ± 0.3	1.7 ± 0.7	4.8 ± 0.6	5.8 ± 0.3

These values agree well with the Monte Carlo resolution of 1.9 mrad for events with a single BPC hit and 2.2 mrad in average.

A possible shift in ϑ_{BPC} was found to be less than one mrad this was determined by comparing the mean of $\vartheta_{BPC} - \vartheta_{CIP}$ for many different conditions such as positive and negative z vertex or y axis and different radii. The maximal shift observed was -0.9 mrad.

Appendix B

List of systematical errors

The following two tables (B.1 and B.2 summarize the relative systematical errors which have been considered in the F_2 analysis for each bin separately. Following abbreviations are used:

- E: uncertainty in the energy scale of the BEMC of 1.7%.
- ϑ : possible shift of the angle of 1 mrad.
- SF: structure function dependence of the analysis.
- LAR: uncertainty in the hadronic energy scale of the LAR of 7%.
- RC: uncertainty in the radiative corrections.
- FR: dependence of y_{JB} in the mixed method on different fragmentation models.
- GE: error of the global efficiencies.
- BS: error of the bin size correction.
- BG: error of the background subtraction, photoproduction and beam induced background are considered.
- LE: additional uncertainty at low energies ($E \leq 15$ GeV)
- Total: Total systematical error. No entry means that the error is less than 1%.

Q^2	x	E	ϑ	SF	RC	GE	BS	BG	LE	Total
8.5	0.00012	5	7	6	4	5	4	9	4	17
	0.00018	1	1	6	3	5	4	5	4	11
12	0.00018	4	1	6	3	5	4	7	4	13
	0.00026	3	1	5	3	5	3	1	3	9
	0.00038	1	5	5	3	5	3			9
15	0.00026	2	3	5	3	5	3	6	4	12
	0.00038	1	2	5	3	5	3		2	9
	0.00056	2	1	4	2	5	3			7
	0.00083	9	4	4	2	5				11
	0.00133	6	5	3		5				10
	0.00237	14	14	3		5				21
20	0.00038	1	2	4	3	5	3	4	4	10
	0.00056	1	4	4	2	5	3		1	8
	0.00083	2	4	3	2	5				6
	0.00133	7	3	3	2	5				10
	0.00237	12	1	3	2	5				14
	0.00421	10	1	3	2	5				12
25	0.00056	4	3	4	2	5	3	9	3	10
	0.00083	2	3	4	2	5		3		6
	0.00133	5	3	3	2	5				8
	0.00237	6	3	3	2	5				9
	0.00421	16	1	3	2	5				17
35	0.00056	11	6	4	3	5	3	7	4	18
	0.00083	4	1	4	2	5		1	3	7
	0.00133	2	1	3	2	5				6
	0.00237	7	3	3	2	5				9
	0.00421	12	3	3	2	5				14
	0.00750	6	4	3	2	5				9
50	0.00083	2	4	4	2	5		7	4	9
	0.00133	2	4	3	2	5				7
	0.00237	1	4	3	2	5				8
	0.00421	10	3	3	2	5				12
	0.00750	13	2	3	2	5				15
65	0.00133	8	2	3	2	5		4		10
	0.00237	5	1	3	2	5				8
	0.00421	4	3	3	2	5				8
	0.00750	8	2	3	2	5				10
	0.01334	17	1	2	2	5				18

Table B.1: Systematical errors for the electron method

Q^2	x	E	ϑ	SF	LAR	RC	FR	GE	BS	BG	LE	Total
8.5	0.00026	1	3	5	6	2	5	5	2	4	4	10
12	0.00038	1	2	5	5	2	5	5	2	2	2	8
15	0.00038	2	1	5	8	2	5	5	2	3	3	9
	0.00056	2	2	4	3	2	5	5	2	1	1	8
	0.00083	1	1	4	3	2	5	5	2		1	7
	0.00133	3	2	3	2	2	5	5	1			7
	0.00237	9	9	3	2	2	5	5	1			14
	0.00421	10	13	3	2	2	5	5	1			18
	0.00750	8	19	3	2	2	5	5	1			25
	0.01334	9	10	2	1	2	5	5	1			16
20	0.00056	6	4	4	5	2	5	5	2	2	2	11
	0.00083	1	1	4	5	2	5	5	2		1	5
	0.00133	2	3	3	2	2	5	5	1			7
	0.00237	3	3	3	1	2	5	5	1			7
	0.00421	1	1	3	1	2	5	5	1			6
	0.00750	2	2	3	1	2	5	5	1			7
	0.01334	1	1	2	2	2	5	5	1			6
	25	0.00083	4	5	4	4	2	5	5	2	1	1
0.00133		1	2	3	3	2	5	5	1			6
0.00237		3	3	3	2	2	5	5	1			7
0.00421		3	4	3	1	2	5	5	1			8
0.00750		2	4	3	2	2	5	5	1			7
0.01334		3	3	2	1	2	5	5	1			7
35		0.00133	3	2	4	5	2	5	5	1	1	1
	0.00237	6	5	3	1	2	5	5	1			10
	0.00421	2	2	3	1	2	5	5	1			6
	0.00750	2	2	3	2	2	5	5	1			7
	0.01334	4	4	2	3	2	5	5	1			8
50	0.00133	9	3	3	6	2	5	5	1	1	1	11
	0.00237	4	2	3	2	2	5	5	1			7
	0.00421	3	3	3	1	2	5	5	1			7
	0.00750	3	4	3	2	2	5	5	1			8
	0.01334	3	2	2	2	2	5	5	1			7
	0.02372	9	7	2	1	2	5	5	1			13
65	0.00237	5	3	3	5	2	5	5	1	1		8
	0.00421	5	4	3	2	2	5	5	1			9
	0.00750	3	4	3	2	2	5	5	1			8
	0.01334	7	6	2	2	2	5	5	1			10
	0.02372	4	3	2	2	2	5	5	1			7

Table B.2: Systematical errors for mixed method

Appendix C

Comparison with H1 results

The following two tables (C.1 and C.2) allow a comparison of the values for the structure function and their statistical and systematical errors with the H1 results presented at the Glasgow conference [80]. The H1 analysis used the electron only method and the so called Σ method ([42], [30]) which uses three quantities (energy and angle of the electron and the sum over all hadrons of $(E_h - p_{zh})$) for the determination of x and Q^2 . The numbers quoted in the tables for the Glasgow values correspond to the method with the lowest systematical error.

Q^2 GeV ²	x	Electron only		Mixed		Glasgow	
		F_2	Error stat \pm syst	F_2	Error stat \pm syst	F_2	Error stat \pm syst
8.5	0.00018	1.44	0.07 \pm 0.17	1.32	0.11 \pm 0.14	1.23	0.05 \pm 0.16
	0.00026					1.24	0.04 \pm 0.13
12	0.00026	1.33	0.07 \pm 0.13	1.16	0.08 \pm 0.10	1.39	0.06 \pm 0.14
	0.00038	1.34	0.10 \pm 0.13			1.30	0.05 \pm 0.12
15	0.00038	1.42	0.09 \pm 0.13	1.37	0.11 \pm 0.13	1.44	0.07 \pm 0.12
	0.00056	1.41	0.09 \pm 0.11	1.30	0.08 \pm 0.11	1.39	0.06 \pm 0.10
	0.00083	1.31	0.07 \pm 0.15	1.30	0.07 \pm 0.10	1.21	0.06 \pm 0.12
	0.00133	1.08	0.06 \pm 0.12	1.04	0.06 \pm 0.08	1.16	0.05 \pm 0.10
	0.00237	1.05	0.09 \pm 0.22	0.99	0.07 \pm 0.15	0.97	0.04 \pm 0.10
	0.00421			0.83	0.08 \pm 0.15	0.80	0.04 \pm 0.09
	0.00750			0.58	0.08 \pm 0.15	0.73	0.04 \pm 0.07
	0.01334			0.54	0.08 \pm 0.09	0.61	0.04 \pm 0.07
20	0.00056	1.58	0.09 \pm 0.14	1.29	0.10 \pm 0.14	1.57	0.08 \pm 0.13
	0.00083	1.21	0.07 \pm 0.08	1.27	0.08 \pm 0.09	1.21	0.07 \pm 0.08
	0.00133	1.10	0.06 \pm 0.11	1.08	0.05 \pm 0.08	1.06	0.05 \pm 0.09
	0.00237	0.89	0.05 \pm 0.12	1.02	0.05 \pm 0.08	1.06	0.05 \pm 0.09
	0.00421	0.81	0.05 \pm 0.10	0.70	0.04 \pm 0.05	0.86	0.04 \pm 0.08
	0.00750			0.64	0.05 \pm 0.05	0.76	0.04 \pm 0.08
	0.01334			0.47	0.04 \pm 0.03	0.66	0.04 \pm 0.07

Table C.1: Comparison: this analysis with the H1 analysis presented in Glasgow.

Q^2 GeV ²	x	Electron only		Mixed		Glasgow	
		F_2	Error stat \pm syst	F_2	Error stat \pm syst	F_2	Error stat \pm syst
25	0.00056	1.28	0.09 \pm 0.14			1.52	0.09 \pm 0.12
	0.00083	1.47	0.10 \pm 0.09	1.24	0.10 \pm 0.12	1.27	0.06 \pm 0.10
	0.00133	1.12	0.07 \pm 0.10	1.26	0.07 \pm 0.09	1.05	0.06 \pm 0.10
	0.00237	1.11	0.06 \pm 0.10	1.17	0.06 \pm 0.09	0.94	0.06 \pm 0.07
	0.00421	0.90	0.06 \pm 0.16	0.80	0.05 \pm 0.07	0.75	0.05 \pm 0.06
	0.00750			0.67	0.05 \pm 0.05	0.73	0.05 \pm 0.07
	0.01334			0.53	0.04 \pm 0.04	0.54	0.05 \pm 0.09
35	0.00083	1.67	0.12 \pm 0.12			1.76	0.12 \pm 0.13
	0.00133	1.22	0.08 \pm 0.08	1.23	0.09 \pm 0.16	1.27	0.07 \pm 0.11
	0.00237	1.17	0.08 \pm 0.12	1.22	0.07 \pm 0.09	1.13	0.07 \pm 0.08
	0.00421	0.94	0.07 \pm 0.13	0.89	0.06 \pm 0.07	1.00	0.07 \pm 0.08
	0.00750	0.83	0.06 \pm 0.08	0.78	0.06 \pm 0.05	0.91	0.06 \pm 0.09
	0.01334			0.63	0.05 \pm 0.04	0.89	0.06 \pm 0.08
50	0.00133	1.29	0.10 \pm 0.10	1.34	0.13 \pm 0.16	1.50	0.10 \pm 0.12
	0.00237	1.14	0.09 \pm 0.09	1.14	0.08 \pm 0.09	1.11	0.08 \pm 0.09
	0.00421	0.97	0.08 \pm 0.13	0.95	0.07 \pm 0.07	1.03	0.07 \pm 0.10
	0.00750	0.65	0.06 \pm 0.10	0.57	0.05 \pm 0.05	0.67	0.06 \pm 0.08
	0.01334			0.58	0.06 \pm 0.04	0.68	0.06 \pm 0.08
	0.02372			0.44	0.05 \pm 0.06	0.54	0.05 \pm 0.07
65	0.00237	1.23	0.11 \pm 0.11	1.33	0.13 \pm 0.12	1.50	0.11 \pm 0.12
	0.00421	1.11	0.10 \pm 0.09	1.08	0.09 \pm 0.11	1.17	0.09 \pm 0.09
	0.00750	0.96	0.09 \pm 0.11	0.87	0.08 \pm 0.07	1.01	0.08 \pm 0.11
	0.01334	0.58	0.07 \pm 0.11	0.69	0.07 \pm 0.08	0.71	0.08 \pm 0.08
	0.02372			0.49	0.06 \pm 0.04	0.52	0.06 \pm 0.05

Table C.2: Comparison: this analysis with the H1 analysis presented in Glasgow, cont'd.

List of Figures

2.1	Deep inelastic electron proton scattering.	6
2.2	Relative contribution of Z_0 exchange and γ/Z_0 interference to pure γ exchange.	8
2.3	Lowest order QCD corrections.	10
2.4	Quark and gluon densities at $Q^2=20 \text{ GeV}^2$	14
2.5	Predictions for F_2 at $Q^2 = 20 \text{ GeV}^2$	15
2.6	First order radiative corrections.	16
3.1	Kinematics at HERA.	20
3.2	Resolution of the kinematical variables $-Q^2$, y and x for the electron only method.	22
3.3	Resolution of the reconstruction of y using the Jacquet- Blondel and the double angle method.	24
3.4	Final state bremsstrahlung and initial state bremsstrahlung of the electron.	26
3.5	Effect of radiative corrections on the reconstruction of kinematical variables.	27
4.1	The HERA storage ring.	30
4.2	A typical deep inelastic scattering event.	32
4.3	Schematic side view of the H1 detector.	33
4.4	Schematic side view of the tracking area of H1.	34
4.5	CIP geometry.	36
4.6	Run dependent efficiency for CIP.	37
4.7	CIP efficiency as a function of track parameters.	38
4.8	CIP efficiency as a function of φ and z	39
4.9	BPC geometry.	42
4.10	Inefficiency of the four BPC planes.	43
4.11	Radius and φ dependence of the BPC plane efficiency.	44
4.12	Run dependency of the BPC efficiency.	45
4.13	Efficiency for finding a CIZ segment linked to a CJC track.	47
5.1	Effect of different selection steps on the energy and angle distribution.	51
5.2	z -vertex distribution for the selected DIS events.	53

5.3	Theta resolution as determined from Monte Carlo simulations.	54
6.1	Monte Carlo simulations: Reconstructed energy deposited in the BEMC compared to the simulated energy.	57
6.2	Energy deposited in the BEMC for 'pion like' and 'electron like' clusters. . .	59
6.3	Contribution of tagged photoproduction events to the DIS event sample. . .	60
6.4	Rejection of photoproduction background by a cut on the distance of the closest BPC hit.	62
6.5	Radius dependency of the efficiency for finding a BPC hit within 5 cm for kinematic peak events.	63
6.6	Efficiency of the DBPCL cut as a function of the energy for the DIS sample. .	64
6.7	Number of BPC hits within 5 cm of the cluster c.o.g. as function of the energy. .	65
6.8	Distribution of DCLBP vs energy.	66
6.9	Background estimators for the BPC cut.	67
6.10	Lateral cluster size for simulated photoproduction events.	70
6.11	Energy weighted cluster radius for simulated DIS events.	71
6.12	Missing backward energy (E_{minPz}).	72
6.13	Efficiency for finding a CIP or CIZ hit in function of the minimal distance in φ and z	73
6.14	Efficiency for finding a CIP or CIZ segment as a function of the azimuthal angle φ and the z position.	74
6.15	Reduction of photoproduction events by the CIPCIZ cut using simulated events. .	75
6.16	Percentage of events with a CIPCIZ hit as a function of the electron energy. .	76
6.17	A typical γp event which can be rejected using the CIPCIZ information. . .	77
6.18	ECRA distribution for events rejected and kept by the CIPCIZ cut.	79
6.19	Rejection of γp events by the use of the CIPCIZ cut.	80
6.20	Percentage of remaining γp background after all cuts.	81
7.1	z -vertex distribution for data and Monte Carlo events.	83
7.2	Energy and angle distribution for data and Monte Carlo events.	85
7.3	Event distribution in the $x - Q^2$ plane.	86
7.4	Acceptance the electron only method.	87
7.5	Acceptance in the $x - Q^2$ plane for the mixed method.	88
7.6	Proton structure function F_2 as a function of x in eight bins of Q^2	94
7.7	F_2 (electron only) compared with data presented in Glasgow.	95
7.8	F_2 (mixed) compared with data presented in Glasgow.	96
7.9	Proton structure function F_2 with four different parametrizations.	97
7.10	Proton structure function F_2 with four different parametrizations (cont'd.). .	98
A.1	Difference between three different angles in the backward direction.	104

List of Tables

2.1	Abbreviation for the DIS process.	6
2.2	Splitting function for different processes with gluon radiation in $LLA(Q^2)$	11
2.3	Naive estimate for the quark and gluon density as a function of x	12
2.4	Different parametrizations for quark densities.	13
4.1	HERA parameters.	31
4.2	CIP geometry.	35
4.3	Efficiency for CIP in percentage.	40
4.4	BPC parameters.	41
4.5	CIZ parameters.	46
5.1	ϑ resolution in backward region.	55
6.1	Identified photoproduction events in the DIS sample.	68
6.2	Photoproduction events rejected by the BPC cut.	69
7.1	Global efficiencies with respect to Monte Carlo simulations.	84
7.2	Proton structure function F_2	99
7.3	Proton structure function F_2 , cont'd.	100
B.1	Systematical errors for the electron method	108
B.2	Systematical errors for mixed method	109
C.1	Comparison with Glasgow results.	111
C.2	Comparison with Glasgow results, cont'd.	112

Bibliography

- [1] E. D. Bloom et al., Phys. Rev. Lett. **23**, (1969) 930.
- [2] M. Breidenbach et al., Phys. Rev. Lett. **23**, (1969) 935.
- [3] H. Fritzsch, M. Gell-Mann, H. Leutwyler, Phys. Lett. **47B**, (1973) 1346.
- [4] R. P. Feynman, Phys. Rev. **163**, (1969) 1415.
- [5] M. Bonesini et al., Z. Phys. **C38**, (1988) 371.
- [6] Proc. of the HERA workshop, Hamburg (1987), ed. R. D. Peccei, DESY, Hamburg (1988), vol. 1,2.
- [7] Proc. of the HERA workshop on Physics at HERA, Hamburg (1991), eds. W. Buchmüller and G. Ingelman, DESY, Hamburg (1992), vol. 1,2,3.
- [8] G. Ingelman et al., "Deep inelastic physics and simulation" in ref. [6], p.3.
- [9] C. G. Callan, D. Gross, Phys. Rev. Lett. **22**, (1969) 156.
- [10] J. Blümlein et al., "Structure Functions, Quark Densities and λ_{QCD} at HERA", in ref. [6], p.67
- [11] A. M. Cooper et al., " Measurement of the Longitudinal Structure Function and the Small- x GLuon Distribution of the Proton", in ref. [6], p.231.
- [12] G. Altarelli, G. Parisi, Nucl. Phys. **B 126**, (1977) 296.
- [13] V. N. Gribov, L. N. Lipatov, Sov.J. Nucl. Phys. **15**, (1972) 78; Yu. L. Dokshitzer, JETP **46**, (1977) 641.
- [14] A. D. Martin, "Structure Functions and small x Physics", Proceedings of the XXI International Meeting on Fundamental Physics "Physics at HERA", Madrid (1993) F. Barreiro, L. Hervas and L. Labarga eds., Singapore (1994), p.250.
- [15] R. K. Ellis et al., Nucl. Phys. **B470**, (1994) 517.
- [16] L. V. Gribov, E. M. Levin and M. G. Ryskin, Phys. Rep. **100** (1983) 1.
- [17] A. H. Mueller and J. Qiu, Nucl. Phys. **B 268**, (1986) 427.

- [18] A. D. Martin, R. G. Roberts and W. J. Stirling, Phys. Lett. **B256**, (1991) 258.
- [19] A. D. Martin and W. J. Stirling "MRS Parton Distributions", RAL preprint RAL-93-077 (1993).
- [20] CTEQ collaboration, J.Botts et al., Phys. Lett. **304**, (1993) 159, now superseded by CTEQ2: J. Botts et al. (unpublished).
- [21] M. Glück, E.Reya and A.Vogt, Z. Phys. **C53** 127 (1992), Phys. Lett. **B306**, (1992) 391.
- [22] A. Kwiatkowski, H.Spiesberger and H.-J. Möhring, Comp. Phys. Commun. **69**, (1992) 155.
- [23] A. Akhundov et al."TERAD91" in [7], p.1285.
- [24] A. Akhundov, "Treatment of the Radiative Corrections for the ' ${}^{\prime}92F_2(x, Q^2)$ '", DESY internal H1 note, DESY, H1-12/93-335 (1993).
- [25] W. Hollik, "Radiative Corrections in Deep Inelastic Scattering - Essentials for HERA Processes", in ref. [6], p.579.
- [26] C. Weizsäcker, Z. Phys. **88** (1934) 612.
- [27] E. Williams, Phys. Rev. **45** (1934) 729.
- [28] G.Kramer and H. Spiesberger, "Radiative Corrections to ep Scattering, A Survey", in ref. [7] p.789.
- [29] J. Feltesse "Measurement of inclusive differential cross-sections",in ref. [6], p. 33.
- [30] U. Bassler, G. Bernardi "Progress on Kinematical Variables Reconstruction. Consequences for D.I.S. Physics at Low x ", DESY internal H1-Note, H1-03/93-274 (1993).
- [31] S. Bentvelsen et al. "Reconstruction of (x, Q^2) and extraction of the structure function at HERA", in ref. [7], p.23.
- [32] M. Fleischer and E. Poppel, BEMC energy calibration from quasi-elastic scattered electrons, DESY internal H1-note, DESY, H1-07/93-304 (1993).
- [33] A. Blondel and F. Jacquet, Proceedings of the study of an ep facility for Europe, ed U.Amaldi, DESY **79-48** 391 (1979).
- [34] G. Bernardi and W. Hildesheim, "A detailed simulation of the F_2 measurability at HERA", in ref. [7], p.79.
- [35] H1 Collaboration, I. Abt et al., Nucl Phys. **B 407**, 515 (1993).
- [36] K. Müller, Proceedings of the Moriond Conference 1994, to be published.
- [37] ZEUS Collaboration, M. Derrick et al., Phys.Lett. **B316**, (1993) 412.

- [38] A. M. Cooper-Sarkar, R. C. E. Devenish and M. Lancaster, "Measurement of $F_L(x, Q^2)$ at low x and extraction of the gluon distribution", in ref.[7], p.155.
- [39] H. Spiesberger et al., "Radiative corrections at HERA", in ref. [7], p.798.
- [40] M. W. Krasny, "Determination of the longitudinal structure function at HERA", DESY internal report, DESY, DESY-91-117 (1991).
- [41] L. Favart and M. Fleischer, "Radiative Corrections at H1", H1 internal report, DESY, H1-09/93-317 (1993).
- [42] N. Wulff, "Tiefinelastische Elektron-Proton-Streuung bei kleinem x -Bjorken", Dissertation Hamburg 1994, Interner Bericht DESY FH1T-94-01 (1994).
- [43] HERMES collaboration, "Technical design report", DESY internal report, DESY-PRC 93/03 (1993).
- [44] HERA-B collaboration, T. Lohse et al. "An experiment to study CP Violation in the B System Using an Internal Target at the HERA Proton ring", proposal, DESY internal report, DESY-PRC 94/02, (1994).
- [45] B. H. Wiik, "HERA status", in ref [7], vol.1, p. 1.
- [46] F. Willeke. Proc. XVth Int. Conf. on High-Energy Accelerators, Hamburg (1992).
- [47] H1 collaboration, I. Abt, et al., Phys.Lett. **B321**, (1994) 161.
- [48] H1 collaboration, I. Abt, et al., " Energy Flow and Charged Particle Spectra in Deep Inelastic Scattering at HERA", submitted to Zeitschrift für Physik C, (1994)
- [49] H1 collaboration, I. Abt, et al., Z.Phys. **C61**, (1994) 59.
- [50] H1 collaboration, T. Ahmed, et al., Phys.Lett. **B299**, (1993) 374.
- [51] I. Abt et al., H1 collaboration "The H1 detector at HERA", DESY internal report, DESY 93-103 (1993).
- [52] St. Eichenberger et al., Nucl. Instr. and Meth. **A323**, (1992) 532.
- [53] St. Eichenberger, " A fast pipelined trigger for the H1 experiment at HERA based on multiwire proportional chamber signals", Ph. D thesis, University of Zurich (1993), unpublished.
- [54] R.Eichler et al., The first level MWPC trigger for the H1 detector, DESY internal H1 note, 04/87-61, DESY (1987).
- [55] H. J. Behrend and W. Zimmermann, Proc. Int. Conf. Computing in High Energy Physics, Tsukuba, Japan (1991), Universal Academy Press, ISBN 4-946443-09-6 (1991).

- [56] K. Müller et al., Nucl. Instr. and Meth. **A457**, (1992) 456.
- [57] F. Sauli, CERN Yellow Report, CERN 77-09; reprinted in T. Ferbel, Experimental Techniques in High Energy Physics, Frontiers in Physics (Addison-Wesley, Menlo Park, 1987), p.59.
- [58] P. Robmann, "The central inner z chamber of the H1 experiment", Ph. D thesis, University of Zurich (1994), unpublished.
- [59] E. Peppel, "Messung der Protonstrukturfunktion F_2 unter besonderer Berücksichtigung des H1-Rückwärtskalorimeters", Dissertation Hamburg 1994, Interner Bericht, DESY FH1K-94-03 (1994).
- [60] Ch. Brune, U. Hölzke and K. Meier, "BEMC calibration 1993" H1 internal report, DESY, H1-04/94-352 (1994).
- [61] P. Reimer, "MC study of BEMC energy resolution and software calibration constant dependence on impact point position, electron energy and ep vertex smearing.", unpublished, (1990).
- [62] T. Wolff et al., Nucl. Instr. Meth. **A323**, (1992) 537.
- [63] F. Charles, J. F. Laporte and E. Perez, "Deep Inelastic Scattering low and medium Q^2 events selection", DESY internal H1 note, H1-05/94-357 (1994).
- [64] J. Ban et al., "The BEMC single electron trigger (BSET)", DESY internal H1-note, H1-07/92-235, (1992).
- [65] T. Kurca, report to the ELAN group at DESY (1994).
- [66] A. de Roeck "Results from the H1 experiment", to appear in the proceedings of the International Europhysics Conference on High Energy Physics, Marseille, July 1993 (1993).
- [67] H1 Collaboration, T. Ahmed, et al., Phys.Lett. **B299**, (1993) 385.
- [68] Review of Particle Properties, Phys. Rev. **D45** (1992)
- [69] S. Levonian, Lebedev Physical Institute, 117924 Moscow, private communication.
- [70] Sebastian Reinshagen, report to the ELAN group at DESY (1994).
- [71] Erik Evrard, report to the ELAN group at DESY (1994).
- [72] A. Panitch, "Vertex reconstruction and BPC efficiency determinations for the 1993 structure function analysis", DESY internal H1-note, H1-08/94-373, (1994).
- [73] A. de Roeck, report to the ELAN group at DESY, (1994).
- [74] G. A. Schuler and H. Spiesberger, "DJANGO", in [7], p. 1419.

- [75] M. Klein, report to the ELAN group at DESY, (1994).
M. Klein et al., "Analysis II of the 1992 Data of the Structure Function $F_2(x, Q^2)$ ", DESY internal H1-note, H1-12/93-332, (1993).
- [76] G. Marchesini et al., *Computer Phys. Comm.* **67** (1992) 465.
- [77] G. Ingelman, "LEPTO 6.1" in [7], p.1366.
- [78] T. Sjöstrand and M. Bengtsson, *Computer Phys. Comm.* **43**, (1987) 367.
- [79] S. Levonian, Lebedev Physical Institute, 117924 Moscow, private communication.
- [80] V. Brisson, G.Rädel contributed papers to the 27th International Conference on High Energy Physics, Glasgow, 20-27th July 1994.
J. Feltesse, invited talk at the 27th International Conference on High Energy Physics, Glasgow, 20-27th July 1994.

Acknowledgments

I am very grateful to all my colleagues in H1 for the stimulating working atmosphere and many interesting discussions. Particularly I want to thank

Ueli Straumann for his permanent technical and moral support even in times with very tight time constraints.

Prof. Dr. P. Truöl for the chance he gave me to work in the H1 collaboration, though coming from the solid state physics. He gave me a large degree of freedom in finding and defining my analysis work.

The ELAN group at DESY in which this analysis was carried out, for many discussions and technical help.

The H1 tracker group for the good and pleasant cooperation

The Zurich part of the H1 collaboration for the nice atmosphere in and outside of our offices, especially

Stefan Eichenberger, Christian Dollfus and Peter Robmann, it was fun to work with them with the chambers and in the North Hall.

Hanspeter Beck for his patience in computer advises.

Thom Wolff, Marco Arpagaus and Roland Bernet for many discussions on different topics.

Josef Riedlberger for many advises in physics and entertaining hours besides physics.

And Nicolaus Busch for his patience and love even in times with too much work.

This list is far too short to mention all the colleagues and friends who helped me in many ways to complete this work. Thanks!

Curriculum vitae

Personalien:

Name: Müller
Vorname: Katharina
Geboren: 7. Oktober 1963 in Zürich
Bürgerort: Zürich

Bildungsgang

1970-1979 Primar- und Sekundarschule in Fehraltorf
1979-1983 Gymnasium Typus Lehramt an der Kantonsschule Wetzikon
1983-1987 Studium der Physik an der Universität Zürich
Nebenfächer: Mathematik und Astronomie
1987-1988 Studienaufenthalt (1 Semester) am Trinity College in Dublin, Irland
1988-1989 Diplomarbeit in Experimentalphysik unter der Leitung von Prof. Dr. D. Brinkmann
Titel: "Kernspinresonanz unter Druck am Hoch- T_c -Supraleiter $YBa_2Cu_3O_{7-\delta}$
und am Halbleiter $YBa_2Cu_3O_{6+\epsilon}$ "
1989 Diplom in Experimentalphysik
1989-1994 Wissenschaftliche Mitarbeit beim H1 Experiment an HERA am DESY (Hamburg)
und Dissertation bei Prof. Dr. P. Truöl.

Dozentenverzeichnis

A. Amann	H. H. Keller	G. Rasche
C. Amsler	U. Matter	G. Scharf
A. O. Benz	M. Mali	B. Schmid
D. Brinkmann	P. F. Meier	H. R. Schwarz
K. Bösigler	V. Meyer	J. O. Stenflo
E. Brun	H. H. Müller	N. Straumann
B. Derighetti	H. Nussbaumer	U. Straumann
R. Engfer	B. D. Patterson	A. Thellung
M. Greuter	R. E. Pixley	P. Truöl
V. Huber-Dyson	H. S. Pruyss	D. Wyler
H. Keller	W. Reichart	